

**Study of Advanced Slider Concepts for  
Precision Cargo Airdrop Operations  
(Grant F49620-98-0125)**

Dr. Jean Potvin  
Department of Physics  
Parks College of Engineering and Aviation  
Saint Louis University  
St. Louis, MO

Year-3, Mid-Year Report Submitted to:  
Dr. Steve Walker  
U. S. Air Force Office of Scientific Research

January 22, 2001



**Study of Advanced Slider Concepts for  
Precision Cargo Airdrop Operations  
(Grant F49620-98-0125)**

Dr. Jean Potvin  
Department of Physics  
Parks College of Engineering and Aviation  
Saint Louis University  
St. Louis, MO

Year-3, Mid-Year Report Submitted to:  
Dr. Steve Walker  
U. S. Air Force Office of Scientific Research

January 22, 2001

**Abstract**

This project aims first at improving the modeling of the inflation characteristics of parachutes reefed with a slider, in particular the type of round and cruciform parachutes decelerating military systems. We are also investigating the inflation performance of new slider designs such as heavy sliders, variable grommet friction sliders, computer-controlled sliders, etc. Specifically, we want to find out whether such designs can lead to lower and reliable opening shocks together with short inflation times, and optimal inflation reliability.

We report on the results obtained during the first half of FY00 as well as on the analysis of the test drop data collected in FY99. Both FY99- and FY00-datasets were the result of test drops of full scale and half-scale cruciform and flat circular parachutes, in unreefed as well as in slider-reefed configurations. Other FY00 results discussed in this report include an exciting new theory of unsteady drag, which will prove valuable in improving the accuracy of our parachute inflation simulation codes.

## Table of contents

|   |    |
|---|----|
| 1. Executive Summary                                | 3  |
| 2. Summary of Accomplishments - FY00 (first half)   | 6  |
| 3. Inflation code development                       | 7  |
| 3.1 General introductory remarks                    | 7  |
| 3.2 New models for the description of unsteady drag | 8  |
| 3.3 Simulation of the early pressurization stage    | 9  |
| 3.4 Testing and use of the complete inflation code  | 10 |
| 3.5 Test drop data for code validation              | 10 |
| 4. Active slider design                             | 12 |
| References  | 13 |
| Appendix 1. Definitions                             | 14 |
| Appendix 2. Paper submitted to Journal of Aircraft  | 16 |
| Appendix 3. Time graphs of the measured riser loads |    |
| Figures   |    |

## 1. Executive summary of results, up to present

The two main goals of this research project are:

- 1) To continue the development of a simulation code of slider-reefed parachute inflation by including more realistic modeling and by performing a validation through the use of a large database of ram-air, flat circular and cruciform parachute inflation data. This database is to be established either from the available literature or from new drop tests performed by this PI and his team.
- 2) To propose and study new slider designs aimed at improving the inflation performance of cargo airdrop parachute systems (cup-shaped parachutes).

### 1. Inflation simulation code development

The improvements of the inflation model that were made in FY98 and FY99 included: 1) the addition of an extra degree of freedom for the simulation of ballistic trajectories; 2) the use of a general time evolution for the calculation of instant parachute surface area as applied to slider-reefed flat circular and cruciform parachutes; and, 3) a new drag coefficient evolution equation to simulate more accurately the effects of unsteady aerodynamics on  $C_D$ . The first half of FY00 saw more modeling refinements as well as more parachute data collection for validation purposes:

- New model for the calculation of the drag coefficient of accelerating and decelerating bluff shapes.

The effects of unsteady aerodynamics on parachute inflation enter through the time-variation of the drag coefficient during the parachute canopy spreading phase as well as after, when the parachute-payload system quickly settles into steady flight. In FY99 a parachute deceleration model based on the drag coefficient of accelerating disks showed good agreement with our FY99 data on half-scale cruciform and flat circular parachutes. This good agreement was unfortunately not repeated in a comparison done in FY00, using *full-scale* parachute data. For this reason a new drag coefficient model was formulated and shown to compare favorably with both half-scale and full-scale data. As described in the following section and in a paper recently submitted to *Journal of Aircraft* (see Appendix 2), the model includes new drag equation evolution formulae for both accelerating and decelerating bluff shapes. The model is better motivated from a physics point-of-view. It is also detailed, and yet general enough to make non-trivial predictions on the value of  $C_D$  before and during unsteady motions without resorting to the usual "added mass" parameterization, which has been shown to not apply to all parachute deceleration profiles.

- Simulation modeling of the early pressurization stage

Slider-reefed parachutes inflate through the two stages of early pressurization and slider descent (see Appendix 1 for definitions). During early pressurization the parachute

adopts a temporary inflated (and inflating) shape as the slider remains pressed against the canopy and the payload continues to decelerate. So far, only the slider-descent stage had been considered in our computer model. In FY00 a full model of early pressurization was tested and added to allow the complete simulation of a payload's trajectory during both stages. The model is based on Ludtke's  $t^6$ -law which has been shown to be very successful in reproducing correctly the time dependence of the drag force during the inflation of a wide variety of *unreefed* parachutes [1]. This new model is described in Section 3 below and also in Appendix 2 where it was used in the validation of the unsteady drag model discussed previously.

- New test drop data for code validation

In FY99 over 60 test drops were performed on half-scale cruciform and flat circular parachutes with, and without sliders. More test drops were performed in FY00, this time 30 drops on both half- and full-scale cruciform parachutes and flat circular parachutes outfitted with new slider sizes. In particular, these parachutes were dropped under the same ballistic conditions, with and without sliders in order to isolate the effects of the slider reefing for opening shock control.

- Code validation

Code validation of slider reefing inflation dynamics is continuing at this time and will be presented in the final report of this project. Current features being tested include: 1) assuming a near constant surface area during slider descent, which is more justified for cupped chutes than for ram-air ones because of their low aspect ratio; 2) adding the newly-found unsteady drag equations to describe the post-inflation phase of the parachute-payload trajectory; and 3) using this same unsteady drag equation to justify new approximations in the equation of motion of the slider-descent phase.

## 2. New slider designs

New slider designs were studied theoretically in FY 98 and FY99 using the inflation code, and drop-tested using 1/2-scale and full-scale parachutes in FY 99 and FY00. The slider designs listed in the original proposal included:

- Concept A: passive slider, with variable friction pads on the suspension lines.
- Concept B: passive slider, fitted with weights to increase its inertia.
- Concept C: smart (or "active") active slider, fitted with a micro-processor which would control micro-brakes according to input signals collected by a slider-mounted altimeter and/or accelerometer.

Three new concepts were added in FY99 namely:

- Concept D: Passive or active slider linked via bridle to a pilot chute of variable inflated surface area.
- Concept E: Inflation sequences along a non-vertical (i.e. ballistic) trajectory.

- Concept F: Double reefing, where a slider is used in conjunction with line reefing applied near the crown area of the parachute. Slider descent would be initiated by the cutting of the reefing line by a pyrotechnic cutter activated by a time fuse, altitude sensor or any other microprocessor-based hardware sewn on the parachute.

The results of the past two and a half years are as follows:

- Computer simulations have shown that concept B (i.e. tuning slider weight) provides little inflation control because of unsteady aerodynamics effects which make the slider's motion insensitive to slider mass;
- The test drops performed in FY99 have shown that concept A (i.e. slider friction tuning) may not be practical given that the line tension differential above and below the slider is smaller on cruciform and circular parachutes than on ram-air parachutes due to their smaller aspect ratio. Smaller line tension result in little friction usable for inflation control purposes.
- The test drops performed in FY99 have shown that concept D offers the reliability, simplicity of implementation *and* wide range of inflation control;
- Concepts C, D and F provide a useful first active slider design which could mitigate the negative effects of abnormally hard openings; however concept C may be the hardest to implement given the sophisticated hardware needed.
- Computer simulations have shown concept E to further reduce the amount of maximum opening shock.

FY00 has seen our efforts focusing on concept F, which has been shown experimentally to be the simplest, cheapest and most versatile implementation of active opening shock control. In a way, concept F marks a departure from the philosophy of using a "smart slider" on a "dumb chute", going instead to that of using a "dumb slider" on a "smart chute". Our past simulations and test drops of active slider concepts has shown that it is far more easier to control slider dynamics via parachute pressurization than by any other means.

In FY00 four more test drops were performed to test such doubly-reefed parachutes. In all tests the parachute flew in a slider-up configuration (or "drogue" phase) for at least four second before a pyrotechnic cutter severed the crown reefing line. The tests were performed with two new sliders of sizes that were different from the FY99 designs, as well as with suspended payloads of up to 300 lbs.

## 2. Summary of Accomplishments – FY00 (first half of the year)

The following was accomplished during the first half of FY00:

- Testing of important improvements to the Ideal Parachute Model computer program which included more accurate physics to describe the drag effects of unsteady aerodynamics and a new model of early pressurization;
- Execution of dozens of computer simulations, 50% of which were on round parachutes, 0% on ram-air parachutes and 50% on cruciform parachutes;
- Hiring and training of Ms. Becky Brocato, Mr. Rodney Kutz and Mr. Carlos Manglano to work on this project. These students are Aerospace Engineering seniors at Saint Louis University.
- Ms. Brocato and Mr. Manglano wrote a paper entitled *Size and Speed Scaling Study of Parachute Inflation*. Their paper was the result of the testing of the Ludtke's  $t^6$ -model discussed previously. **The paper won the third prize at a competition that took place on April 26-28 2000, during the Region V AIAA Student Conference (Wichita, KS).**
- Continuation of the collecting of un-reefed and slider-reefed round parachute and cruciform data using the equipment developed during FY99.
- Travel to U.S. Army research facilities in Natick, MA and Yuma, AZ to attend New World Vistas – Precision Air Delivery (or NWV-PAD) meetings.
- Continued the patent application process for the double reefing concept (i.e. concept F), in collaboration with R. Benney – Natick Army Soldier Systems Center.
- Submitted the paper entitled *Using Galilean Relativity for the Study of Unsteady Drag*, for publication in the *Journal of Aircraft*. A copy is included in Appendix 2.
- Submitted two abstracts/papers to the 16<sup>th</sup> AIAA Aerodynamic Decelerator Systems Technology Seminar and Conference, which will take place in Boston MA at the end of May 2001. The papers are entitled *Deceleration Modeling of Unreefed Cruciform and Round Parachutes During and After Inflation* - and - *Inflation and Glide Studies of Slider-reefed Cruciform Parachutes*.

### 3. Inflation simulation code development

#### 3.1 General introductory remarks

The modeling of the trajectory of an inflating or post-inflating parachute is first based on the combined parachute/load Newtonian equation of motion, here written for a purely vertical trajectory for the sake of simplicity:

$$ma(t) = -\frac{1}{2}\rho\Sigma(t)v^2(t) + W \quad (3.1)$$

Here  $m$ ,  $a$ ,  $v$ ,  $\rho$  and  $W$  correspond to the system's total mass, descent acceleration or deceleration, descent speed, air density at deployment altitude and system all-up-weight respectively. However, such an equation cannot be solved until the time dependence of the drag area  $\Sigma(t)$  ( $= C_D(t)S(t)$ ) is known. Until recently, most *unreefed* parachute inflation studies have used Ludtke's law, namely [1]:

$$\Sigma(t) = \left[ \frac{C_D(t_{final})S(t_{final}) - C_D(0)S(0)}{t_{final}^6} \right] t^6 + C_D(0)S(0) \quad (3.2)$$

Ludtke's formulation requires the knowledge of the empirical inflation time  $t_{final}$ , all other inputs being available from measurements performed "on the laboratory floor". On the other hand, the inflation of *slider-reefed* parachutes (slider descent stage only) can be described by the Ideal Parachute Model, which uses a differential equation derived from the slider's own Newtonian equation of motion, namely [2 - 4]:

$$\frac{d^2\Sigma}{dt^2} = [(K_1 + K_2\Sigma(t)) + (K_a + K_b\Sigma^{1/2}(t) + K_c\Sigma^{3/2}(t))]v^2(t) \quad (3.3)$$

The K-factors are known constants or functions of time written in terms of a parachute's specific construction characteristics. These factors have the following property:

$$K_1, K_2 \neq 0 \text{ \& } K_a, K_b, K_c = 0 \quad ; \text{ ram-air parachute}$$

and

$$K_1, K_2 = 0 \text{ \& } K_a, K_b, K_c \neq 0 \quad ; \text{ round or cruciform parachute}$$

As shown in references 2 and 3, these K-factors can be directly related to a parachute's initial drag area, final drag area, suspended weight, descent velocity prior to slider descent down the suspension lines and suspension line lengths. These K-factors also depend on the slider construction characteristics such as weight and surface area. Finally,

parachutes decelerating while *fully opened* have long been described using an expression based on the concept of added mass, which expresses the drag coefficient as

$$C_D(t) = C_D^{steady} + 2K \left( \frac{Va}{Sv^2} \right) \quad (3.4)$$

Here  $V$  and  $S$  refer to known representative parachute volume and surface area. On the other hand, constant  $K$  is the so-called *added mass* parameter. Equation (3.4) has been shown to work in inviscid flow conditions, but also in some but not all parachute applications [see Appendix 2 and references therein].

### 3.2 New models for the description of unsteady drag (at fixed surface area)

Parachute dynamics depends in a crucial manner on the knowledge of the time evolution of the drag coefficient. But, as discussed at length by Sarpkaya and Isaacson [5] and by Sarpkaya [6], such time evolution is complicated because the fluid moving about objects in unsteady motions is no longer characterized by a constant value of the Reynolds number. Accelerated and decelerated motions imply a host of new phenomena including a time-dependent wake shape, time-dependent vortex shedding intervals and locations, hard-to-predict boundary layer transitions and laminar-to-turbulent flow transitions, and values of the drag coefficient that are much greater than unity [7, and Appendix 2]. This was shown quite clearly in several tow tank studies of cylinders, plates and disks at low and medium Reynolds number and in parachute test drops [8, 9 and Appendix 2]. *Most importantly, these experiments have also shown that the time dependence of the drag coefficient for accelerating motions is not the same for that of decelerating motions.*

The following formulas represent an improvement over equation (3.4), and is applicable to a much greater number of parachute applications (see Appendix 2 for details). These formulas are to be used together with the standard drag force equation written as follows:

$$F_D(t) = \frac{1}{2} C_D(t) \rho S v(t)^2 \quad (3.5)$$

Our review of the tow tank literature on the drag of accelerating bluff shapes has shown that *accelerating* parachutes would have a drag coefficient given by (see Appendix 2 for details):

$$C_D \approx (20 \cdot \delta)^{0.46} \quad 0.3 < \delta < 10 \quad (3.6)$$

$$C_D \approx C_D^{steady} \cdot (4.67)^{\delta^{0.68}} \quad 0 < \delta < 0.3 \quad (3.7)$$

$$C_D(t) = C_D^{steady} + 2K \left( \frac{V}{SD} \right) \delta \quad \delta \gg 10 \quad (3.8)$$

where  $\delta$  is the so-called acceleration modulus defined as:

$$\delta = \frac{Da}{v^2} \quad (3.9)$$

Note that equation (3.8) is that same as (3.4), but is restricted to accelerations of non-streamlined objects in the high- $\delta$  regime. Equations (3.7) – (3.9) are the result of a direct fit of a tow tank experiment performed by Iversen and Ralent, which covered low and intermediate Reynolds number values [7].

In the case of *decelerating* parachutes, we have proposed a new formula based on the Galilean equivalence between bodies decelerating in a static fluid and those drifting and accelerating with a *moving* fluid (again, see Appendix 2 for details):

$$C_D(t) = C_D^{init} \left( \frac{v(t)}{v_t} \right)^{\beta'-2} \quad (3.10)$$

where

$$\beta' = 2 + \frac{\ln\left(\frac{C_D^{init}}{C_D^{steady}}\right)}{\ln\left(\frac{v_t}{v_T}\right)} \quad (3.11)$$

Equations (3.10) and (3.11) were tested via a comparison with our half- and full- scale parachute data, as shown in figures 1 and 2.

### 3.3 Simulation of the early pressurization stage

Early pressurization takes place after the parachute has been pulled out of the bag, a process initiated as soon as the suspension lines have deployed and stretched taut (Appendix 1). Early pressurization begins when the parachute adopts a tube-like shape and ends when it has an inverted pear-like shape (figure 3). During this stage the slider remains pressed against the skirt because of its own built-in drag, and begins to move only when the pressure inside the parachute is high enough to cause a high enough line tension differential above and below the slider to push it down. The beginning of slider descent marks then end of the early pressurization stage. Lengthening the duration of early pressurization is one sure way to reduce opening shock since even a partly opened parachute will generate enough drag to cause a substantial deceleration of the payload.

Until recently, our parachute inflation code did not simulate the payload deceleration sustained during early pressurization. Such defect has been corrected by using again Ludtke's formalism (equation (3.2)), this time to describe the temporal change during early pressurization of the parachute's diameter as measured *at its mid-section* (see figure 3). The logic behind this idea is that Ludtke's model has been shown to be very successful in describing the unreefed inflation of many parachute shapes [1].

Our idea is to assume that the model could do well for inflating parachutes that are shaped like inverted pears (see figure 3), and *unreefed* at their mid-section.

This idea was validated by looking at the data generated during drops NWV114 and NWV116, which involved full-scale Natick-Army cruciform parachutes with a 110 lbs payload. In those two cases the slider had a very high drag area and descended very slowly and over a very short distance down the suspended lines. For that reason, most of the high drag forces sustained occurred during early pressurization and post-inflation deceleration. A computer model thus using equation (3.1), with (3.2) during early pressurization and (3.10) during post inflation deceleration was used to produce the calculated forces shown in figures 4 and 5. The comparison of these calculated values with experimental data, also shown in these figures, indicates a good agreement with this theory.

### 3.4 Testing and using the complete inflation code

The second half of FY00 will see the testing and use of our inflation code, updated and upgraded with the features discussed previously. To recapitulate, the upgraded code will be based on Newton's equations as applied for a pseudo-ballistic trajectory:

$$ma = -\frac{1}{2}\rho S(t)C_D(t)v^2 + W \cos\theta \quad (3.12)$$

where

$$\frac{d\theta}{dt} = -g \frac{\sin\theta}{|v|} \quad (3.13)$$

Simultaneously, the following drag coefficient formulas would be used to simulate the different inflation stages:

- Equation (3.2) when  $0 < t < t_{earlypress}$  (early pressurization stage)
- Equation (3.3) with  $K_b \sim K_c \sim 0$ , when  $t_{earlypress} < t < t_{sliderdescent}$  (slider descent stage)
- Equation (3.10) when  $t_{sliderdescent} < t < t_{postinfl}$  (post-inflation stage)

The results of the validation of this upgraded code will be presented in this project's final report.

### 3.5 Test drop data for code validation

As of now, over 96 test drops have been performed in Missouri and Illinois to produce inflation data for the purpose of code validation and slider design testing. The parachutes tested so far were: A 15ft-diameter, half-scale model of the USAF C-9 personnel emergency flat circular parachute, and a (30 year-old and very porous) 28 ft-diameter personnel emergency flat circular parachute used by the U.S. Navy. Reference 2 give ample details on their construction, including the type of cloth used. We found these

parachutes to have a 22 ft/sec and 16.6 ft/sec terminal descent rate while carrying payloads of 100 and 120 lbs respectively. The other parachutes tested included a one-of-a-kind U.S. Army-Natick 24ft cruciform parachute, built out of two 9.2ft-by-24.0ft panels sewn into a cross and attached to 20 suspension lines of length 19.7 ft. The cloth had a permeability of 30 to 45 cfm and was made of 200 denier nylon; the suspension lines were made of MIL-C-7515 Type V chord. Also tested were half-scale models of this U.S. Army cruciform parachute, built out of two 4.2ft-by-10.7ft panels and 20 suspension lines of length 12.2 ft and 17.0ft. The cloth used was the same as for the full-scale article and the suspension lines were of MIL-C-7515 Type I-A chord. The terminal speed of these cross chutes was measured at 17.8 ft/sec and 32 ft/sec while carrying payloads of 100 and 128 lbs respectively.

In FY99 the test payloads were dropped from a Cessna 411 twin-engine aircraft over a commercial drop zone located in Bowling Green MO. In FY00, the drops were carried out from a Beech King Air C-90 twin-turbine aircraft over the Vandalia Municipal airport in Vandalia, IL. The drops were conducted between 1000 and 2000 feet MSL (i.e. 500ft AGL in the St. Louis MO area) from speeds ranging between 90 and 110 kias.

As described in details in the FY99 final report, the payloads consisted of 100 lbs steel tubs shaped as half-scale models of the U.S. Army A-22 container, with dimensions of 24in x 20in x 23in. Payload weight could be adjusted by adding cement sacs at the bottom of the tubs. Each tub was instrumented with a load cell inserted on each of the two parachute risers, and with an electronic barograph located inside the tub. These instruments sent data to an on-board data acquisition system recording at a rate of 500 Hz. All components were built using off-the-shelf components.

The riser loading recorded during those tests are shown in Appendix 3. Note that not all drops were fully instrumented, as sometimes required by the nature of the test.

#### 4. Active slider design

Our simulations and test drops of active slider concepts performed over the past two years have shown that the cheapest and most flexible implementation of an "active" or "smart" slider is that of the doubly reefed parachute. As its name indicates, the concept involves the use of a standard slider in conjunction with a reefing line routed through rings sewn near the crown area of the parachute as shown in figures 6 and 7. During the first portion of the drop (or "drogue phase"), the reefing line would be used to restrict the parachute canopy to a partly-inflated shape, such as those shown in figure 3. At a given altitude or time, or according to other parameters measured by on-board sensors, the reefing line would be severed to allow full inflation of the canopy.

The simplicity of the idea resides in the fact it requires no special hardware on the slider itself, other than a hole cut in the fabric to insure inflation reliability, to keep the latter in the "up" position during the drogue phase. And only *one* cutter would be needed to trigger the *double* unreefing of the crown line and slider during canopy spreading phase. Here the combined action of the slider's own drag and small parachute crown radius (while reefed) would keep the slider naturally pushed against the parachute skirt without any extra rigging. Upon cutter activation, crown reefing would be deactivated to allow full canopy inflation which in turns would create the necessary line tension differential above and below the slider to generate a down-pushing force on the latter.

This concept would thus make use of a single parachute to perform the function of two parachutes, thus leading to rigging simplicity and low cost. It would also reduce the opening shock sustained by cruciform parachutes since, after cutter activation, the inflation process would evolve through two inflation stages of finite duration. The time delay caused by these two stages would ensure early deceleration of the payload to lower speeds at the moment of full canopy spreading and thus to smaller opening shocks. Designing for a desired opening shock would be simply done by adjusting the slider dimensions, namely slider vent hole size and slider perimeter, and crown reefing line length. In particular, the circumference of the crown reefing line would determine the descent speed of the system prior to cutter activation. The lower such speed would be the lower the opening shock. All size combinations so far tested have shown the expected reductions in opening shock. For example, see figure 8 as well as the riser load evolution curves of drops NWV45 and NWV131 in Appendix 3.

A patent application is currently being put together in collaboration with Natcik.

## References

- 1) T. W. Knacke, "Parachute Recovery Systems Design Manual"; Para Publishing (Santa Barbara, CA 1992).
- 2) J. Potvin, G. Peek and B. Brocato; "Modeling the Inflation of Ramair Parachutes Reefed with Sliders"; To appear in the Journal of Aircraft.
- 3) T. Perschbacher and J. Potvin, "The Improved Ideal Parachute Model and Its Application to the Study of Inflation Dynamics of Slider-Reefed ram-air and Round Parachutes"; AIAA paper 99-1750.
- 4) J. Potvin and G. Peek, "Experimental Validation of the Ideal Parachute Model: A Status Report"; AIAA paper 99-1746.
- 5) Sarpkaya, T. and Isaacson, M., *Mechanics of Wave Forces on Offshore Structures*, Van Nostrand Reinhold Company, New York, 1981.
- 6) Sarpkaya, T., "Method of Analysis for Flow Around Parachute Canopies", *11<sup>th</sup> AIAA Aerodynamic Decelerator Systems Technology Conference*, AIAA, Reston, VA, 1991, pp. 1 – 17, ; AIAA Paper 91-0825.
- 7) Iversen, H.W., and Balent, R., "A Correlating Modulus for Fluid Resistance in Accelerated Motions", *Journal of Applied Physics*, **22**, pp. 324 – 328, 1951.
- 8) Cochran B.C., White, B.R. and Macha, J.M., "Experimental Investigation of Added Mass during Parachute Deceleration – Preliminary Results", AIAA-91-0853, pp.171-180.
- 9) Strickland, J. H. and Macha, M.; "Preliminary Characterization of Parachute Wake Recontact", *Journal of Aircraft*, **27**, 501 – 506, 1990.
- 10) Potvin, J.; "Simple Description of Airflow Characteristics Inside and Unfolding Parachute"; *Journal of Aircraft*, **36**, 809 – 818, 1999.

**APPENDIX 1.**  
**DEFINITIONS**

### The slider

A slider is a simple rectangle of nylon fabric re-enforced with nylon straps along its edges. The parachute's suspension lines are routed through grommets also rigged at the slider's corners on a ram-air canopy, or along its periphery on a round canopy. As its name indicates, its construction allows the slider to move up or down the suspension lines depending on the balance of the forces acting on it.

### Two slider configurations

Sliders come into two basic varieties: the *pilot-chute-controlled* (or PCC) configuration, where the slider is additionally linked via bridle to the parachute's extraction/pilot chute or the *sail* configuration, where the slider is not attached to the pilot chute. In the case of the PCC, the amount of slider drag is mostly determined by the pilot chute size. In the case of the sail slider, slider drag is determined only by the amount of fabric covering the nylon strap that defines its shape. So far, commercial ram-air parachutes have used both configurations, while only the sail design has been used on commercial round parachutes.

### The four stages of parachute deployment and inflation

The inflation stages of slider-reefed parachutes are very similar to those of skirt-reefed cargo parachutes: both begin with line deployment which is then followed by the extraction of the parachute itself out of the bag/container (or "bag strip"). This is followed by early pressurization, a stage during which the parachute gets its first "gulp" of air and begins inflating. However, the parachute is not allowed to spread completely during this stage because of line reefing or slider reefing, which constrains to a small projected surface area the parachute's skirt on a round parachute or aspect ratio on a ram-air parachute. With line reefing, full canopy spreading begins only after the reefing line is severed by a time-activated cutter. In the case of slider reefing, canopy spreading is only achieved when the line tension differential above and below the slider overcomes the latter's drag force which initially keeps it pushed against the base of the parachute. In most cases, maximum loading of a parachute's structure occurs during this last inflation stage.

**APPENDIX 2**

**USING GALILEAN RELATIVITY FOR THE STUDY OF UNSTEADY DRAG**

**Submitted to the Journal of Aircraft**

# USING GALILEAN RELATIVITY FOR THE STUDY OF UNSTEADY DRAG

J. Potvin<sup>1</sup>, G. Peek<sup>2</sup> and B. Brocato<sup>3</sup>  
Parks College Parachute Research Group  
Saint Louis University, St. Louis, MO 63103

## Abstract

We present a new point of view for the study of the drag force experienced by objects accelerating or decelerating along straight and non-periodic trajectories. The formalism is based on relating via Galilean transformations the drag force experienced by an object in a given reference frame to the drag force sustained by the same object in another reference frame. In such alternate frames, the fluid may now be in motion but its dynamics relative to the object remains the same. We apply this idea to the study of a disk accelerating in a static fluid under a constant external force, a situation that is shown to be equivalent to the same object decelerating downwind or accelerating upwind under the same external force. We also consider the example of a high-drag object decelerating in a static fluid under a constant external force, which in another reference frame can be seen as accelerating downwind under the influence of the same external force. A new drag coefficient equation for motions accelerating under a constant force is derived from the data of Iversen and Balent (*Journal of Applied Physics*, **22**, pp. 324 – 328, 1951). Also proposed is new drag coefficient equation for decelerating motions in a static fluid, which is compared with parachute test drop data.

---

<sup>1</sup>Associate Professor, Department of Physics, potvinj@slu.edu , member AIAA

<sup>2</sup>Consultant, Industrologic Inc.

<sup>3</sup>Research assistant, student Member AIAA

Submitted to JOA

## NOMENCLATURE

$A$  = Constant of integration, equation (13)

$a(t)$  = instant acceleration

$b_0$  = initial value of the drag area used in equation (29)

$b_1$  = time-normalized drag area difference used in equation (29)

$C_D$  = drag coefficient

$C_D^{disk}$  = drag coefficient of a disk accelerating in a static fluid

$C_D^{ini}$  = initial value of the drag coefficient

$C_D^{steady}$  = drag coefficient in steady motion

$C_k$  = Opening shock factor

$\bar{C}(s(t) / D)$  = effective drag coefficient in equation (3)

$D$  = characteristic diameter

$F_D$  = force of drag

$F_{ext}$  = external force, assumed constant

$F_{max}$  = maximum parachute opening force

$K$  = "added mass" coefficient

$\bar{K}(s(t) / D)$  = effective "added mass" coefficient in equation (3)

$R$  = disk radius

$R_e$  = Reynolds number

$s(t)$  = total displacement of an accelerating body

$S$  = reference surface area

$S_{flat}$  = parachute surface area as measured on a flat surface

$t_f^{infl}$  = final time of canopy spreading during parachute inflation

$t_{max}$  = time of maximum drag during parachute inflation

$v(t)$  = instant speed

$v_i$  = speed at the beginning of the acceleration/deceleration

$v_f$  = speed at the end of the acceleration/deceleration

$v_{ref}$  = speed of a particular reference frame

$v_{relwind}$  = speed of the fluid at infinity, relative to the moving object

$v_{snatch}$  = parachute descent speed at the end of suspension line deployment

$v_T$  = terminal speed

$V$  = volume of the apparent mass

$V_{chute}$  = volume of the air enclosed inside the inflated shape of parachutes

$\beta'$  = exponent defined in equation (20)

$\delta$  = acceleration modulus

$\delta_i$  = initial acceleration modulus

$\epsilon$  = small time increment

$\rho$  = air density

Superscripts

' = designates quantities measured in any Galilean frame moving with respect to the fluid

## INTRODUCTION

Inflated parachutes and other high-drag objects often travel along trajectories that are far from being characterized by a constant velocity and constant drag coefficient<sup>1-21</sup>. Even during flight or cruise they may undergo unsteady motions such as during a turn maneuver or during oscillations caused by excess air spilling from alternate sides. This means that before reaching terminal velocity, these objects may feature drag coefficients that are time-dependent as well as motion- and trajectory-dependent. This introduces an additional level of complexity in the standard drag equation, which then must be expressed in terms of a time-dependent drag coefficient:

$$F_D(t) = \frac{1}{2} C_D(t) \rho S v(t)^2 \quad (1)$$

Such time dependence is due to many factors, which often times play equal parts in defining a specific drag evolution profile. As discussed at length by Sarpkaya and Isaacson<sup>2</sup> and by Sarpkaya<sup>3</sup>, the fluid moving about objects in unsteady motions is no longer characterized by a constant value of the Reynolds number. Here accelerated and decelerated motions imply a host of new phenomena including a time-dependent wake shape, time-dependent vortex shedding intervals and locations, hard-to-predict boundary layer transitions and laminar-to-turbulent flow transitions, and values of the drag coefficient which are much greater than unity<sup>22-31</sup>. This was shown quite clearly in several tow tank studies of cylinders, plates and disks at low and medium Reynolds number<sup>22-26</sup> and in parachute test drops<sup>18,31</sup>. The time-dependence of the drag coefficient may also arise from the geometry of the motion itself, as with motions that periodically return a body back into its own wake. As in the case of immersed pendulums, the body

encounters a flow that is far from being at rest and is most likely turbulent. Finally, there are significant differences in drag time evolution between seemingly similar motions. Comparing the tow tank studies of uniformly accelerated cylinders<sup>27</sup> and of disk accelerating to terminal speed<sup>22</sup>, one finds profound differences in drag coefficient evolution that go beyond shape differences. The same can be said when comparing accelerating motion and decelerating motions. Here low-Reynolds number tow tank studies of decelerating cylinders and plates have shown wake vortices changing sizes, and detach laterally and away from the wake-generating body<sup>32</sup>. This contrasts with the wake of an accelerating cylinder, which adopts a potential flow pattern after the disappearance of the primary wake vortices<sup>32</sup>. The lack of aerodynamic similarity between these two motions is particularly evident in swiftly decelerating motions where bodies are stricken from the rear by previously-shed wake structures<sup>31</sup>, an event that is never encountered in accelerating motions.

Given this complexity, many unsteady drag studies have borrowed from the idea that an accelerating object causes similar accelerations of portions of the surrounding fluid mass, which in effect change the effective inertia of the object. This idea suggests writing the drag force as the sum of the standard drag  $v^2$ -term and of a so-called “added mass” term that is proportional to acceleration<sup>2,3</sup>:

$$F_D = \frac{1}{2} C_D^{steady} \rho S v^2 + K \rho V \frac{dv}{dt} \quad (2)$$

$V$  is the volume of the co-accelerated air mass, which will be different from the that of the moving object. The constant  $C_D^{steady}$  is the value of the drag coefficient when the body is travelling at constant velocity<sup>1</sup>. In conditions where incompressible and laminar flow prevail, the value of  $K$  can be shown to be constant, exclusively shape-dependent and

obtained via potential flow theory<sup>17, 33, 34</sup>. In contrast, the value of  $K$  as applied to various applications generating turbulent wakes has been shown to vary with time, object shape, size and speed, and even with trajectory. For example, Cochran, White and Macha<sup>18</sup> found  $K$  to be time-dependent in their study of fast-opening, highly-loaded parachutes dropped from a high ceiling.

Equation (2) can be made to work correctly when application-specific constant values and/or time-dependent functions are replacing  $C_D^{steady}$  and  $K$ . In another parachute study, Macha<sup>19</sup> found that the simulation of highly porous, supersonic parachutes decelerating in the range of 20 to 40 g's could use constant values of  $K$  to accurately reproduce experimental data over several parachute types and speeds. Contrary to potential flow theory however, such values had to be adjusted according to the initial speed and terminal speed of the payload under consideration. On the other hand, Sarpkaya and Garrison showed in their study of cylinders moving at constant acceleration that  $C_D^{steady}$  and  $K$  could be meaningfully replaced by functions of the instant displacement  $s(t)$  in order to give

$$F_D = \frac{1}{2} \bar{C}(\frac{s(t)}{D}) \rho S v^2 + \bar{K}(\frac{s(t)}{D}) \rho V \frac{dv}{dt} \quad (3)$$

with  $D$  being the cylinder diameter, and  $S$  and  $V$  being proportional to the cylinder's surface area and volume respectively<sup>27</sup>. These authors showed this formulation to be valid at Reynolds numbers of up to  $5.2 \times 10^5$ .

Being that motion-specific has made unsteady drag theory an empirical science. In this paper we wish to show that, quite contrary to this expectation, some generalizing is possible *in cases that can be related by Galilean transformations of reference frames*. In particular, it will be shown that such transformations can relate the drag equation of

specific accelerating motions to that of specific decelerating motions and vice-versa. To illustrate the concept, new specific drag formulas valid for discs accelerating to terminal speed in a static fluid are derived from empirical data and transformed into corresponding formulae applicable for downwind decelerations and upwind accelerations. It will also be shown that Galilean transformations can be used to search for an *a priori* unknown expression of the drag force, using a known one as obtained in another equivalent Galilean reference frame. In particular, this strategy will be used to derive a new formula describing the drag coefficient of decelerating bluff shapes in a static fluid, by using plausible assumptions on the motion of the same object accelerating downwind in another reference frame. Such a formula is validated via the comparison with detailed parachute test drop data.

### **Galilean Relativity and Equivalence Classes for Unsteady Motions**

Galilean transformations relate the coordinates  $(x, y, z, t)$ , speed  $(v)$  and acceleration  $(a)$  of an object moving in one reference frame to the corresponding set of coordinates and variables of the same object seen from another reference frame moving at constant velocity  $v_{ref}$  (Figure 1). More specifically these transformations are formulated as follows:

$$x' = x - v_{ref}t, \quad y' = y, \quad z' = z, \quad t' = t, \quad v' = v - v_{ref}, \quad a' = a \quad (4)$$

#### Galilean equivalence classes

Going into different reference frames related by specific Galilean transformations permit to lump together motions that seems at first very different. Consider the motion depicted in figure 1a, namely that of an object increasing its speed from  $v_1$  to  $v_2$  in a static fluid while under a constant external force  $F_{ext}$ . Depending on the speed  $v_{ref}$  of the

alternate reference frame, such motion can be transformed into other motions involving speed gain, speed loss and even speed loss followed by speed gains. For example, figure 1b shows the case of a reference frame characterized by  $v_{ref} > v_f$  where the object loses speed in a fluid moving rearwards at  $-v_{ref}$ . Aerodynamically, nothing has changed since the speed of the object *relative* to the fluid remains the same. Both decelerating and accelerating motions appear, on the other hand, when  $v_i < v_{ref} < v_f$ : here the body first decelerates downwind to a full stop from an initial speed of  $v_i' = v_i - v_{ref}$ , then reverses direction and accelerates upwind until it reaches its final value  $v_i' = v_f - v_{ref}$ .

The type of external force and trajectory define broad equivalence classes characterized by the same fluid dynamics relative to the moving body. Being Galilean-invariant classes, these would include both accelerated and decelerated motions within each class, depending on the value of  $v_{ref}$ . Here we are interested into two specific classes, which are defined as follows:

- *Class 1:* Acceleration along a straight line in a fluid at rest, under the influence of an constant external force;
- *Class 2:* Deceleration along a straight line in a fluid at rest, under the influence of an constant external force.

In both classes, the presence of a constant external force brings the body into a state of dynamical equilibrium with drag, to ultimately generate a constant-speed motion. An example of class-1 motion includes powered aircraft accelerating in static air, a motion that would be Galilean-equivalent to one involving a deceleration with, or acceleration into a head wind. On the other hand, class-2 examples would include a parachute decelerating in static air, a case that is Galilean-equivalent to that of a ground vehicle

powered by a sail and accelerating downwind while being opposed by a constant external force such as friction. Other classes can be defined similarly, using other types acceleration profiles and/or external forces, such as the constant-acceleration motion studied by Sarpkaya and Garrison<sup>27</sup>.

It is to be emphasized that using Galilean transformations may also be helpful in finding the best experimental conditions for the study of a particular motion. In contrast to accelerations for example, the physics of decelerations is more difficult to study in tow tank experiments because of the difficulty in establishing exactly the correct initial conditions in a tank's limited amount of space, particularly when the initial state includes high speeds and non-zero accelerations. On the other hand, test-dropping objects from aircraft can be carried out, but again for a limited set of initial conditions. Fortunately, being of class-2 type means that decelerated motions in static fluids can also be studied as accelerations in reference frames where the fluid is also moving, a perspective that may be easier to setup in tow-tank experiments.

#### Drag coefficient transformation

Considering the 1-dimensional equation of motion of an object subjected to a drag force and to a constant external force  $F_{ext}$ ,

$$ma = -\frac{1}{2}C_D(t)S\rho v^2 + F_{ext} \quad (5a)$$

and considering also the equation of the same object as measured from a moving reference frame,

$$ma' = -\frac{1}{2}C'_D(t')S'\rho v'^2 + F'_{ext} \quad (5b)$$

one finds the following relation between the drag coefficient measured in each reference frames, after assuming  $F_{ext} = F'_{ext}$  and using equation (4):

$$C_D' v'^2 = C_D v^2 \quad (6)$$

This result means that the product  $C_D v^2$  has the same value in all reference frames, i.e. is Galilean-invariant. On the other hand, because speed is not Galilean-invariant, the value of the drag coefficient wont be either, instead changing from frame-to-frame as

$$C_D' = \frac{C_D \cdot (v' + v_{ref})^2}{v'^2} \quad (7)$$

For example, in cases where  $v'$  is greater than  $v$ , equations (6) and (7) imply smaller values of the drag coefficient in moving reference frames. This observation also applies to the steady state value of the drag coefficient. Additionally, the corresponding terminal speed  $v_T'$  would increase being related to  $C_D^{steady'}$  through the well-known formula

$$v_T' = \sqrt{\frac{2F_{ext}}{\rho S C_D^{steady'}}} \quad (8)$$

### **Acceleration-Deceleration Equivalence: Kinematics of Class-1 Bodies Moving with Respect to Static or Moving Fluid**

Using Galilean transformations permits to study a great number of accelerated or decelerated motions belonging to a given Galilean class. As example we discuss the basic, yet very instructive class-1 case of a disk accelerating from rest to its terminal velocity under the influence of an external force. Such a case was studied experimentally by Iversen and Balent<sup>22</sup> using disks accelerating in water under the force of gravity via line tension. These tow tank experiments involved submerged disks being pulled from rest by a rope attached to weights falling outside the tank. The driving weights ranged

between 2 and 10lbs, disk diameters (D) between 1ft and 2ft, speeds between 0 to 4 ft/sec, accelerations 0 to 4 ft/sec<sup>2</sup>, and Reynolds number reaching 1000. These authors found that the instant value of the drag coefficient (as defined by (1)) could be graphed as a sole function of the acceleration modulus  $\delta$ , a dimensionless ratio given by:

$$\delta = \frac{Da}{v^2} \quad (9)$$

Iversen and Balent showed that the beginning of the disks' fall was characterized by very large acceleration moduli, namely  $\delta \sim 10$ , to be followed by monotonically decreasing values as the disks reached terminal speed.  $C_D$  was shown to converge towards its steady state value as  $\delta$  went to zero. Interestingly, they also showed how potential flow-inspired expressions like equation (2) could be justified at very large  $\delta$ .

The correlation between  $C_D$  and  $\delta$  as mapped by Iversen and Balent can be summarized by the formulae below, which we derived by curve-fitting their graphical data:

$$C_D^{disk} \approx (20 \cdot \delta)^{0.46} \quad 0.3 < \delta < 10 \quad (10a)$$

$$C_D^{disk} \approx C_D^{steady} \cdot (4.67)^{\delta^{0.63}} \quad 0 < \delta < 0.3 \quad (10b)$$

Equations (10a) and (10b) were defined to have the same value and the same slope at  $\delta = 0.3$ . This particular value of the acceleration modulus marks in this tank experiment a distinct but smooth transition between the high- and low- $\delta$  regimes.

Iversen and Balent also discussed the limit  $\delta \rightarrow \infty$ , which occurred at the onset of motion from the disk's initial state of rest. These authors argued that the fluid motion about the disk actually corresponds to potential flow *before* the formation of the annular

vortex at the disk's edge. For a short while, this would allow the use of equation (2) for the description of disk drag. Their data appear to confirm this trend, and the fact that at large acceleration moduli, the value of  $K$  decreases with  $\delta$  and converges to a value close to potential flow theory. In the light of this observation, rewriting equation (2) in terms of the acceleration modulus would give:

$$C_D^{disk}(t) = C_D^{steady} + 2K\left(\frac{V}{SD}\right)\delta \quad \delta \gg 10 \quad (10c)$$

It is interesting to note that the drag coefficient of objects *uniformly* accelerating from rest may also feature a one-to-one dependence on the acceleration modulus similar to (10c), as can be shown with the case of the accelerated cylinders studied by Sarpkaya and Garrison<sup>27</sup>. Here the motion allows for a simple relationship between  $\delta$ ,  $a$ ,  $v(t)$  and  $s(t)$ , namely  $s(t)/D = (2\delta)^{-1}$ . Using this result in (3) and calculating the ratio  $2F/\rho S v^2$  from (1) would yield a drag coefficient entirely dependent on  $\delta$ , in a form similar to (10c) with  $\bar{C} = \bar{C}(\delta)$  and  $\bar{K} = \bar{K}(\delta)$ .

Except at the onset of the motion, Iversen and Balent reported little dependence of  $C_D$  on Reynolds number, a fact explained by the wake of disks being fully turbulent at relatively low  $Re$  as compared to more streamlined shapes like cylinders. Perhaps this observation could help answer the unresolved issue of whether equations (10a-c) are still valid when the disk is travelling at constant speed at  $t = 0$  or, more interestingly, when  $a(0) \neq 0$ .

#### Medium- $\delta$ , low-mass solution

Simple kinematics can be derived analytically in the medium- $\delta$  and low-mass regime, by combining equation (10a) with the general equation of motion (5) while

assuming  $ma \ll F_{ext}$ . Here it is also assumed that  $v(0)$  is actually different from zero, but small enough to be relevant to the dynamics included in (10a) at high acceleration moduli. Under such assumptions, the resulting equation of motion is recast as

$$a = \frac{2F_{ext} \delta^{0.54}}{DS\rho 20^{0.46}} \quad 0.3 < \delta < 10 \quad (11)$$

a result which shows acceleration increasing with acceleration modulus. Equation (11) can be exactly separated in terms of  $a(t)$  and  $v(t)$  and integrated, thus yielding:

$$a(t) = \left[ \frac{2F_{ext}}{D^{0.46} S\rho 20^{0.46}} \right]^{2.17} v^{-2.35} \quad (13)$$

$$v(t) = \left( v(0)^{3.35} + 3.35 \left[ \frac{2F_{ext}}{D^{0.46} S\rho 20^{0.46}} \right]^{2.17} t \right)^{0.30} \quad (12)$$

These forms are of course consistent with the empirical data of Iversen and Balent.

#### Transformations to other class-1 cases

Defining the acceleration modulus with respect to the speed of the fluid at infinity *relative* to the moving object, as in  $\delta \equiv Da/v_{relwind}^2$ , makes this ratio explicitly invariant in all reference frames. Given that the fluid in the tank study of Iversen and Balent was at rest, this makes the acceleration modulus  $\delta$  in equations (9) and (10) a Galilean invariant as well. However, the specific form of the drag coefficient will change from frame to frame because it is not Galilean-invariant, as specified by equation (6). This also means that in other frames, the acceleration modulus is no longer the sole determinant of the value of  $C_D'(t)$ . For example we consider the case of a disk moving in a reference frame moving at  $v_{ref} > v_T$ . Here  $v'_i = -v_{ref}$  and  $v'_f = v_T - v_{ref}$ , which defines an upwind decelerating

motion. In the medium- $\delta$  regime the drag coefficient would be given by the following, as derived from (10a), (4) and (7):

$$C'_D(t) \approx [20 \cdot \delta']^{0.46} \frac{(v' + v_{ref})^2}{(v')^2} \quad (14)$$

where drag now depends on *two* independent variables, namely  $\delta'$  (or  $\delta$ ) and  $v'$ . On the other hand, looking at very high acceleration moduli where drag is either described by (2) or (10c), we get:

$$C'_D(t) \approx \left[ C_D^{steady} + \frac{2KV}{SD} \left( \frac{Da'}{(v' + v_{ref})^2} \right) \right] \frac{(v' + v_{ref})^2}{(v')^2} \quad (15)$$

It is interesting to note that when  $\delta$  is very large, the inertial term is much greater than the steady drag term, which in this case yields the following Galilean-covariant expression,

$$C'_D(t) \approx \left[ \frac{2KV}{SD} \left( \frac{Da'}{(v')^2} \right) \right] \quad (16)$$

that is, a form which has the same mathematical form in all reference frames but not necessarily the same value.

## Searching for a New Formulation of Bluff Body Drag for

### Decelerations in a Static Fluid

Little is known about the mathematical expression of the drag force exerted on decelerating objects in a static fluid, except for equation (2) being applied to motions in inviscid fluids or in other very specific cases<sup>2, 3, 19</sup>. Here we use Galilean transformations to derive an unknown drag formula using as input another drag equation presumed to be

valid in other reference frames. More specifically, we discuss the case of the drag generated by a bluff body decelerating in static air as would, for example, inflated parachutes decelerating people, vehicle or cargo.

Consider the case of a high-drag object decelerating in static air from an initial speed  $v_i$  to a final speed  $v_f$ , the latter being the terminal speed  $v_T$  generated by the external force  $F_{ext}$  via equation (8). Consider also any reference frames that are co-moving at speed  $v_{ref} > v_i$ . In such frames the fluid is moving rearward and the resulting Galilean transformation makes the object look as accelerating in a downwind direction, from an initial speed of  $v_i' = v_i - v_{ref}$  to a final speed of  $v_f' = v_T - v_{ref}$ . In other words, the object is observed drifting with the wind and accelerating to a constant final speed. In what follows we derive a formula for the drag coefficient based on considerations obtained in the reference frame of such wind drifters. The derivation is based on the following assumptions:

- Convergence to zero-drag coefficient at large times

In situations where the external force is very small, wind drifters will settle in time into a constant speed that is near to windspeed. In other words, in the limit where  $F_{ext}$  or  $v_T \ll 0$ , one has  $ma' \approx - (1/2) C_D' \rho S v'^2$ , which implies that the drag coefficient converges as  $C_D' \rightarrow 0$  in a sufficiently long time as  $v' \rightarrow v_T - v_{ref} \neq 0$ . Remarkably, this property should be valid regardless of shape and speed range. Of course the specific manner in which this convergence occurs is object- and speed-dependent. For example, cylinders with boundary layer transitions happening while accelerating to drift speed would converge in a manner that is different from that of disks which do not have such transitions.

- No dependence on instant deceleration

By definition, a class-2 motion involves the generation of wake sections produced at earlier times that travel at a faster speed than sections produced at later times. In extreme cases such as with a swiftly decelerating parachute, wakes generated at earlier times can collide with, and even deflate the parachute when the latter's initial speed is at least four times the values of the final speed<sup>31</sup>. For smaller speed differences, one could anticipate the wake sections created at earlier times to still interact with the more recently created sections and body, but more gently. Such an interaction could result in the overall wake being more homogeneous and less-time varying than wakes of accelerating objects (in a static fluid), that is, less dependent on the amount of deceleration sustained *instantly* by the body (i.e.  $a(t)$ ). Moreover, it is conceivable that deceleration-independent wakes could be generated at high-Reynolds numbers where there are no boundary layer transitions; they could also be generated when there are no attached or separating large-scale fluid elements that could directly re-contact with the body. On the other hand, we would anticipate some dependence on the initial acceleration or deceleration.

Thus the drag coefficient of such drifters can be estimated using these assumptions in concert with the fact that the product  $C_D v'^2$  is a Galilean invariant, by writing this product in terms of the wind speed relative to the drifter:

$$C_D v'^2 = B(v' - v_{wind})^\beta \quad (17)$$

$B$  and  $\beta$  are constants to be evaluated later. Such an expression does indeed guarantee a drift speed equal to wind speed when  $F_{ext}$  is zero. Also, being exclusively speed-dependent means that the type of power-law embodied in (17) should actually apply

regardless to the actual magnitude of  $F_{ext}$ . However, it will be shown that the exponent is actually dependent on the external force.

Since  $B$  and  $\beta'$  are Galilean-invariant, one has via (7) the following result in the reference frame where the fluid is at rest:

$$C_D(t) = Bv(t)^{\beta'-2} \quad (18)$$

In particular, equation (18) should hold for both initial and final values of the drag coefficient, namely  $C_D^{init} = B v_i^{\beta'-2}$  and  $C_D^{steady} = B v_T^{\beta'-2}$ . This provides the necessary information for the calculation of  $B$  and  $\beta'$ , and of the final form of the drag coefficient equation:

$$C_D(t) = C_D^{init} \left( \frac{v(t)}{v_i} \right)^{\beta'-2} \quad (19)$$

where

$$\beta' = 2 + \frac{\ln\left(\frac{C_D^{init}}{C_D^{steady}}\right)}{\ln\left(\frac{v_i}{v_T}\right)} \quad (20)$$

It is interesting to note that exponent  $\beta'$  not only change with object shape, but also with the instant value of the drag coefficient at the beginning of the deceleration, as well as with the actual amount of the applied external force. On the other hand, reference to fluid density and viscosity is only made implicitly through  $C_D^{init}$  and  $v_T$ . Also clear is the fact that the acceleration modulus is not much of a factor here in contrast to accelerating objects from rest, as seen in the previous section.

### Initial conditions

A non-trivial feature of this model is that identical shapes may have different drag properties depending on the history of the motion prior to deceleration (i.e.  $t < t_i$ ) as well on the magnitude of  $F_{ext}$ . This is shown in Tables 1 and 2, which display the values of  $\beta'^{-2}$  and of  $C_D^{init}$  for different initial conditions where the applied external force is constant at all times except at  $t_i$ , where possibly  $F_{ext}(t < t_i) \neq F_{ext}(t > t_i)$ . The tables display the cases where the final speed is equal to zero (or  $F_{ext} = 0$ ), or when an object is travelling at zero-acceleration prior to deceleration with drag balanced by  $F_{ext}(t < t_i)$  (leading to  $C_D^{init} = C_D^{steady}$ ), or when the object accelerates prior to  $t_i$  with the drag profile of a disk (Eq. (10)) accelerating under a constant external force different from  $F_{ext}(t > t_i)$ . Note that in the last case, writing the initial value of the acceleration modulus as  $\delta_{i-\epsilon}$  in Tables 1 and 2 reflects the fact that the value of the acceleration modulus  $\delta$  just before the beginning of the deceleration may not be the same just after, given that our model may not yield a continuous  $a(t)$  at  $t = t_i$ .

Some estimates can be obtained by studying the example of a jet-powered vehicle towing a deceleration parachute, which is assumed to have the drag profile of a disk when accelerated. Consider first the case where parachute drag is balanced exactly by engine thrust prior to reducing engine power at  $t_i$ . In this case  $a(t) = 0$  and  $C_D(t) = C_D^{steady}$  at  $t \leq t_i$ , which, according to Tables 1 and 2, means that  $\beta'^{-2} = 0$  and  $C_D^{init} = C_D^{steady} \sim 0.8$ . Here the drag force would vary as  $F_D(t) \propto v^2$ . This would contrast with the case where, prior to  $t_i$ , the aircraft provides unbalanced thrust causing an acceleration. As before, engine power would be reduced at  $t_i$ . Assuming  $\delta_{i-\epsilon} \sim 0.5$  for example would give a maximum drag coefficient of  $C_D^{init} = 2.88$  according to Table 2. Being dependent on initial and final

speed, exponent  $\beta'-2$  would then be approximated by  $\beta'-2 \sim 0.6, 1.39$  and  $5.33$  for speed ratios of  $v_i/v_f \sim 5.0, 2.0$  and  $1.20$  respectively. In other words, the drag force would vary as  $F_D \propto v^{2.6}, v^{3.39}$  and  $v^{7.33}$  respectively.

It is interesting to note that in the limit of very high  $v_i/v_f$ -ratios, the drag force would change as  $F_D(t) \propto v^2$ . Also  $C_D$  would be a constant but with a value different from  $C_D^{steady}$ , depending on the history of the motion. As discussed in more details the next section, the model may provide an explanation as to why the use of equation (2) with constant  $C_D$  may make sense in some turbulent wake deceleration applications after all. Finally, these examples show that depending on the history of the motion, deceleration may or may not depend on the acceleration modulus and if so, only indirectly.

#### Freely decelerating body in a static fluid:

An interesting solution can be obtained analytically when considering the case of an object decelerating in a static fluid without the application of the external force  $F_{ext}$ .

As discussed before, one uses equations (5) and (19) together with  $\beta' = 2$  in order to get:

$$ma = -\frac{1}{2}C_D^{ini} S \rho v^2 \quad (21)$$

an equation that can be recast as follows, using (9):

$$\delta = \frac{C_D^{ini} D S \rho}{2m} \quad (22)$$

Equations (21) and (22) can be integrated exactly to yield:

$$v(t) = v_i \left[ 1 + \frac{v_i \rho S C_D^{ini}}{2m} t \right]^{-1} \quad (23)$$

As expected the speed would converge to zero, here in a time scale defined by the ratio  $2m/v_i \rho S C_D^{ini}$ . Equation (22) also shows that although  $C_D$  does not depend on  $\delta$ , the

decelerating motion itself is  $\delta$ -dependent. Moreover, equation (22) implies that  $\delta$  is constant and determined partly by the history of the motion prior to  $t_i$ , as is now shown. Assuming the object to have the profile of an accelerated disk in the range of  $0 < \delta < 10$  before the beginning of deceleration, equation (22) and (23) would have the following form at  $t = t_i$ :

$$\delta_i = (20 \cdot \delta_{i-\epsilon})^{0.46} \frac{DS\rho}{2m} \quad (24)$$

$$v(t_i) = v_i \left[ 1 + \frac{v_i \rho S (20 \cdot \delta_{i-\epsilon})^{0.46}}{2m} t \right]^{-1} \quad (25)$$

Here again the difference between  $\delta_{i-\epsilon}$  and  $\delta_i$  reflects the fact that the value of the acceleration modulus  $\delta$  just before the beginning of the deceleration may not be the same just after, given that  $a(t)$  may not be continuous at  $t = t_i$ . Note also that transforming this solution into a frame characterized by  $v_{ref} = v_i$  will give a solution applicable to a wind drifter reaching windspeed in the same time scale of  $2m/v_i \rho S C_D^{init}$ .

### Comparison with Parachute Drop Data

Like disks, parachutes are characterized by high drag. They also display no boundary layer transitions because of airflow separation taking place at the leading edge (i.e. skirt) of the canopy<sup>35</sup>. Therefore a validation of the ideas embodied in (19) and (20) can be carried out using the data of the parachute drops we have collected. In the following, the model is applied to parachute motion during the *post-inflation phase*, an

event characterized by the canopy decelerating to terminal speed while remaining fully opened.

#### Experimental conditions and theoretical model

The tests consisted in dropping parachutes at 1000 feet MSL (i.e. 500ft AGL in the St. Louis MO area) from an aircraft flying at speeds ranging between 90 and 110 kias. The suspended loads consisted of 100 lbs steel tubs shaped as half-scale models of the U.S. Army A-22 container, with dimensions of 24in x 20in x 23in (figure 2). Each tub was instrumented with a load cell inserted on each of the two parachute risers (figure 3), and with an electronic barograph located inside the tub. These instruments sent data to an on-board data acquisition system recording at a rate of 500 Hz. All components were built using off-the-shelf components<sup>36-38</sup>. The parachutes tested were as follows: A 15ft-diameter, half-scale model of the USAF C-9 personnel emergency flat circular parachute, and a (30 year-old and very porous) 28 ft-diameter personnel emergency flat circular parachute used by the U.S. Navy. References 35, 39 and 40 give ample details on their construction, including the type of cloth used. These parachutes were found to have a 22 ft/sec and 16.6 ft/sec terminal descent rate while carrying payloads of 100 and 120 lbs respectively. The other parachutes tested included a one-of-a-kind U.S. Army-Natick 24ft cruciform parachute, built out of two 9.2ft-by-24.0ft panels sewn into a cross and attached to 20 suspension lines of length 19.7 ft. The cloth had a permeability of 30 to 45 cfm and was made of 200 denier nylon; the suspension lines were made of MIL-C-7515 Type V chord. Also tested were half-scale models of this U.S. Army cruciform parachute, built out of two 4.2ft-by-10.7ft panels and 20 suspension lines of length 12.2 ft and 17.0ft. The cloth used was the same as for the full-scale article and the suspension lines

were of MIL-C-7515 Type I-A chord. The terminal speed of these cross chutes was measured at 17.8 ft/sec and 32 ft/sec while carrying payloads of 100 and 128 lbs respectively.

The comparison of our model with the parachute riser force data is based on the drag force calculated from this equation of motion:

$$ma = -\frac{1}{2}\rho SC_D^{Meady} \left(\frac{v}{v_t}\right)^{\beta-2} v^2 - \rho V_{chute} a + W \cos \theta \quad (26)$$

$$\frac{d\theta}{dt} = -g \frac{\sin \theta}{|v|} \quad (27)$$

Equation (27) accounts for the time-changing component of weight that is parallel to drag. Under our deployment conditions, the parachute-payload system always traveled along a parabolic-like trajectory, which however appeared linear at the level of a length scale defined by the parachute diameter and suspension line length.

In addition to the new drag equation discussed previously, equation (26) includes a term representing the inertia of the air enclosed inside the parachute throughout the deceleration process. This term takes into account the fact that, while remaining at rest with respect to the canopy, this enclosed air makes the parachute look more like a filled solid than a hollow shell. Note that enclosed air has nothing to do with the air that is co-accelerated ahead of, or behind the parachute as discussed previously in relation to equation (2). In the proposed model, the effects of *external* co-accelerated air (or "added mass") would be represented by the  $v^{\beta-2}$ -term. For all zero-porosity and zero-permeability parachutes the volume of such enclosed air is equal to that of the inflated parachute. In a 20 ft-diameter circular parachute for example, the enclosed air would have a mass of about 4.8 slugs which near sea level would be comparable to the mass of

the 200lbs payload that is usually suspended under such a parachute. Understood as such, using (26) to simulate parachutes with vents, slots and other openings, or with porous fabric, would be more ambiguous given the difficulty of defining what exactly is “enclosed air”. In these cases some of the air entering the parachute exits through the openings at a rate determined by parachute speed and by the surface area of the vents and slots. In other words, the amount of enclosed air which is at rest and remains at rest inside the parachute will be smaller but also much more difficult to calculate. On the other hand, an extreme case that can still be described accurately by (26) would be that of very high-porosity and/or -permeability parachutes, such as cruciform parachutes, where the amount of enclosed air and corresponding acceleration term are very small.

#### Initial conditions

As explained previously, our deceleration model depends on the initial values for the parachute’s descent rate and drag coefficient. In the context of our test drops such numbers are obtained at the very end of the inflation phase. As discussed in reference 31, calculating the drag coefficient from test drop data is particularly difficult, given that the needed acceleration, instant opened surface area and velocity evolutions have to be measured independently and at a level of accuracy that is beyond the capabilities of our instrumentation package. Instead, we have used Ludtke’s well-established simulation method to duplicate the time dependence of the parachute riser force, drag area and payload descent rate during, and at the end of inflation<sup>35, 41</sup>. Ludtke’s formalism is based the use of

$$ma = -\frac{1}{2}\rho S(t)C_D(t)v^2 + W \cos\theta \quad (28)$$

together with

$$S(t)C_D(t) = b_1 t^6 + b_0 \quad (29)$$

where  $b_0$  corresponds to the parachute's drag area prior to inflation, i.e.  $b_0 = S(0) C_D(0)$ . On the other hand,  $b_1$  is expressed in terms of  $b_0$  and of the drag area at the end of inflation, namely as  $b_1 = [(S(t_f^{infl})C_D(t_f^{infl}) - b_0)] / (t_f^{infl})^6$ . Test drops performed over the past decades have shown Ludtke's  $t^6$ -law to work very well with most inflating, unreefed and unslotted parachutes made of near-zero permeability cloth<sup>35</sup>. Established from the direct measurement of the ratio  $2(ma - W \cos \theta) / \rho v^2$ , this law takes into consideration all effects relevant to the unsteady aerodynamics affecting an inflating parachute, including co-accelerated air mass and the actual opening and spreading of the canopy. Like equation (26), equation (28) neglects the elastic response of the suspension lines and parachute cloth during inflation, which for the light payload weight being tested here, allows the full transmission of the drag force to the load measuring cells in a time scale much shorter than the inflation time. A comparison between Ludtke's model and the measured riser loading during inflation is shown in figures 4 through 7.

The relationships between the variables measured in the test drops at the end of inflation (i.e.  $t = t_f^{infl}$ ) and the initial values needed in (19) and (20) can be written as  $C_D^{init} \equiv C_D(t_f^{infl})$  and  $v_i \equiv v(t_f^{infl})$ . Their numerical values were obtained by

- directly comparing the riser load curves with the computer solutions of equations (27), (28) and (29), using the direct measurements of  $m$ ,  $\rho$ ,  $S(0)$  (from video),  $S(t_f^{infl})$  (from video),  $F_{drag}(t_f^{infl})$  (load cell),  $t_f$  (load cell) and  $C_D^{steady}$  (terminal descent rate measurement);
- assuming an initial drag coefficient estimated at  $C_D(0) \sim 1$  because of the tub's near cubical shape;

- tuning the values of  $C_D^{init}$  and  $v(0)$  for best fits of (28)-(29) to the overall measured drag force.

In addition to  $C_D^{init}$ , this procedure yielded  $v_i$  as a product and allowed a subsequent numerical solution of (26)-(27) without any further parameter tuning or measurement.

Figure 8 shows the effects of changing the values of  $t_f$ ,  $v_0$  and  $C_D(t_f^{infl}) S_f$ , which demonstrates that such fitting is not unique. This problem is partly solved by comparing the calculated  $C_D^{init}$  with Wolf's compilation of the world's data on the parachute opening shock factor  $C_k$ <sup>42</sup>. The latter is a dimensionless constant defined as  $C_k = 2F_{max}/\rho S_{flat} v_{snatch}^2$ , with  $F_{max}$ ,  $v_{snatch}$  and  $S_{flat}$  corresponding to the maximum drag force sustained, the descent speed at the end of suspension line deployment and the parachute's total surface area respectively. Wolf showed that  $C_k$  scaled reasonably well over five orders of magnitude of the mass ratio  $\rho (S_{flat})^{1.5}/m$ , for a large number of parachute sizes, parachute types and deployment conditions. Given that  $C_D^{init} = 2F_D(t_f^{infl})/\rho S_{flat} v(t_f^{infl})^2$ , one has:

$$C_D^{init} = C_k \left( \frac{F_D(t_f^{infl})}{F_{max}} \right) \left( \frac{v_{snatch}}{v(t_f^{infl})} \right)^2 \quad (30)$$

The consistency check for  $C_D^{init}$  was thus calculated from (30), using Wolf's value of  $C_k$ , the simulation values for  $F_{max}$ ,  $F_D(t_f^{infl})$  and  $v(t_f^{infl})$ , the known aircraft speed for  $v_{snatch}$  and an explicit measurement of  $S_{flat}$ .

### Comparison with experiment

Figures 4 through 7 show the comparison between calculated and experimental riser force, during and after inflation. In agreement with most unreefed parachutes studies of the past<sup>35</sup>, the computer simulations show that the moment of maximum opening force occurs *before* the full spreading of the parachute. Discarding the brief variations of

measured drag during the early part of inflation caused by the elastic nature of the suspension lines and fabric flutter, the agreement between theory and experiment is good. In particular, our deceleration model gives a good estimate of the deceleration rates after the end of inflation (very high rates) and just prior to settling into terminal velocity (very low rates). According to (19) such rates should be proportional to  $v^{\beta'-1}$ .

Figures 9 through 12 show the corresponding time evolution of the calculated drag coefficient. Figure 11 in particular shows the effect of changing the values of  $v_0$  and  $C_D(t_f^{init}) S_f$ . Quite remarkably, the half-scale parachutes feature higher values and rates than the full-scale parachutes. This could be explained by the fact that, in our tests, the inflation time scale is much smaller for the half-scale than for the full-scale parachutes. Being deployed under similar aircraft speeds, drop altitudes and payload weights, this translates to higher opening forces for the smaller chutes than for the large ones. All this would therefore contribute to drag coefficients that would be larger for the former than for the latter. Table 3 shows the calculated values of  $C_D^{init} / C_D^{steady}$ ,  $v_i/v_T$  and  $\beta'$  for the four parachute tested. According to (19) the drag force would vary as

$F_D \propto v^{5.29}$ ,  $v^{5.98}$ ,  $v^{2.12}$  and  $v^{2.00}$  for the half-scale cruciform parachute, half-scale C-9 parachute, full-scale cruciform parachute and the full-scale Navy round parachute respectively. Finally, another point of interest is the minimum value of  $C_D(t)$ , which is smaller than  $C_D^{steady}$  by about 20% to 30%. Such a dip appears to be present also in the post-inflation portion of the data collected by Strickland and Macha in their study of parachutes undergoing wake recontact<sup>31</sup>. The high rate of drag coefficient change,

together with such dip is consistent with the picture of the parachute being "pushed" by portions of its own wake that were produced at an earlier time.

Most interestingly, the full-scale parachutes featuring  $C_D(t) \sim C_D^{steady}$  points to the suitability of describing the drag force by the sum of a steady drag term and an added mass-like terms as in equation (2). Our model (i.e. equation (26)) would predict a value of  $K = 1$ . In contrast, the drag force generated by the half-scale parachutes cannot be re-written this way. As far as very-low or very high permeability/porosity parachutes go, the use of equations (19) and (20) together with Wolf's opening shock factor data and equation (30) could allow some measure of prediction on the applicability of equation (2).

### Concluding Remarks

The idea of using Galilean equivalence classes to study unsteady drag allows the grouping of many different types of motions which share the same aerodynamic properties. Perhaps the most interesting equivalence is the one that exists between decelerating parachutes and wind drifters. Good agreement was shown between test drop data and the drag calculated from our wind drifter-inspired model. However, more experiments, in particular tow tank experiments, are needed to validate completely some of the assumptions made. In particular, a careful investigation is needed to verify the presumed independence on the instant value of the deceleration (i.e.  $a(t)$ ) that lead to the derivation of (19). Moreover, the dependence on the external force needs to be clarified as well.

## Acknowledgements

This work was supported by the US Army Soldier, Biological and Chemical Command (SBCCOM) under contract DAAD16-00-C-9250, and by the US Air Force Office of Scientific Research (AFOSR) under grant F49620-98-1-0125. The authors thank R. Benney, C. Lee and S. Patel (SBCCOM-Natick, MA) and S. Walker (AFOSR) for their advice and support. We also thank J. T. Blimling, R. Kutz, R. Eddy, J. Gentry, O. Guerrero, C. Loehner, C. Manglano, J. Mark, J. Papke, T. Perschbacher, T. Poston and B. Yavitz for their help during the experimental phase of the project.

## REFERENCES

1. Hoerner, S.F.; "Fluid Dynamic Drag"; published by the author; Hoerner Fluid Dynamics (Brick Town, N.J. 1965).
2. Sarpkaya, T. and Isaacson, M., *Mechanics of Wave Forces on Offshore Structures*. Van Nostrand Reinhold Company, New York, 1981.
3. Sarpkaya, T., "Method of Analysis for Flow Around Parachute Canopies", *11<sup>th</sup> AIAA Aerodynamic Decelerator Systems Technology Conference*, AIAA, Reston, VA, 1991, pp. 1 – 17, ; AIAA Paper 91-0825.
4. Cockrell, D. J. and Haidar, N.I.A., "Influence of the Canopy-Payload Coupling on the Dynamic Stability in Pitch of a Parachute System", AIAA-93-1248, 1993.
5. White, F. M. and Wolf D. F., "A Theory of Three-Dimensional Parachute Dynamic Stability", *Journal of Aircraft*, 5, 86 – 92, 1968.
6. Doherr, K. -F., "Theoretical and Experimental Investigation of Parachute-load-System Dynamic Stability", AIAA-75-1397, 1975.
7. Tory, C. and Ayres, R., "Computer Model of a Fully Deployed Parachute", *Journal of Aircraft*, 14, 675-679, 1977.
8. Eaton, J. A. and Cockrell, D. J., "The Validity of the Leicester Computer Model for a Parachute with Fully-Deployed Canopy", AIAA-79-0460, 1979.
9. Yavuz, T. and Cockrell, D. J., "Experimental Determination of Parachute Apparent Mass and its Significance in Predicting Dynamic Stability", AIAA-81-1920, 1981.

10. Cockrell, D. J. and Doherr, K. -F., "Preliminary Considerations of Parameter Identification Analysis from Parachute Aerodynamic Flight Test Data", AIAA-81-1940, 1981.
11. Doherr, K. -F. and Saliaris, C., "On the Influence of Stochastic and Acceleration Dependent Aerodynamic Forces on the Dynamic Stability of Parachutes", AIAA-81-1941, 1981.
12. Eaton, J. A. "Added Mass and the Dynamic Stability of Parachutes", *Journal of Aircraft*, 19, 414-416, 1982.
13. Heinrich, H.G. and Haak, E.L., "Stability and Drag of Parachutes with Varying Effective Porosity", Wright-Patterson AFB, ASD-TDR-62-100, September 1962. Unpublished.
14. Lingard, J. S. "The Effects of Added Mass on Parachute Inflation Force Coefficients"; AIAA-95-1561. *13<sup>th</sup> AIAA Aerodynamic Decelerator Systems Technology Conference*, Clearwater Beach, FL, 1995; pp. 176 – 185.
15. P.B.S. Lissaman, "Apparent Mass Effects on Parafoil Dynamics", AIAA-93-1236, *12<sup>th</sup> RaeS/AIAA Aerodynamic Decelerator Systems Technology Conference*, London, 1993.
16. G.J. Brown, "Parafoil Steady Turn Response to Control Input", AIAA-93-1236, *12<sup>th</sup> RaeS/AIAA Aerodynamic Decelerator Systems Technology Conference*, London, 1993, pp. 248 – 254.
17. S. K. Ibrahim, "Apparaent Added Mass and Moment of Inertia of cup-shaped bodies in Unsterady Incompressible Flow". Ph.D. Thesis, University of Minnesota, 1965.

18. Cochran B.C., White, B.R. and Macha, J.M., "Experimental Investigation of Added Mass during Parachute Deceleration – Preliminary Results", AIAA-91-0853, pp.171-180.
19. Macha, J., M.; "A Simple Approximate Model of Parachute Inflation"; 12<sup>th</sup> *RaeS/AIAA Aerodynamic Decelerator Systems Technology Conference and Seminar*, London, United Kingdom, May 1993; AIAA-93-1206.
20. Wolf, D., E., "A Simplified Dynamic Model of Parachute Inflation", *Journal of Aircraft*, **11**, pp. 28-33, 1974.
21. McVey, D., F., and Wolf, D., E., "Analysis of Deployment and Inflation of Large Ribbon Parachutes", *Journal of Aircraft*, **11**, pp. 96-103, 1974.
22. Iversen, H.W., and Balent, R., "A Correlating Modulus for Fluid Resistance in Accelerated Motions", *Journal of Applied Physics*, **22**, pp. 324 – 328, 1951.
23. Keim, S.R., "Fluid Resistance to Cylinders in Accelerated Motions", *Journal of Hydraulic Division, ASCE*, **82**, No. HY6, pp.1113-1 to 1113-14, 1956.
24. Stelson, T. E. and Mavis, F. T. , "Virtual Mass and Acceleration in Fluids", *Proceedings ASCE*, **81**, Separate No. 670, pp. 670-1 to 670-9, 1955.
25. Laird, A.D.K. and Johnson, C.A., "Drag Forces on Accelerated Cylinders", *Journal of Petroleum Technology*, **8**, pp. 56-67, 1956.
26. Laird, A.D.K., Johnson, C.A. and Walker, R.W. "Water Forces on Accelerated Cylinders", *Journal of Waterways and Harbor Division ASCE*, WW1, pp. 99-119, 1959.
27. Sarpkaya, T., and Garrison, C.J., "Vortex Formation and Resistance in Unsteady Flow", *Journal of Applied Mechanics*, **30**, Series E, pp. 16-24, 1963.
28. Odar, F., and Hamilton, W.S., "Forces on a Sphere Accelerating in a viscous Fluid", *Journal of Fluid Mechanics*, **18**, pp.302-314, 1964.

29. Mavis, F.T., "Virtual Mass of Plates and Discs in Water" *Proc. ASCE, Journal Hydraulics Division*, Paper 7593, 1970.
30. Hamilton, W.S. and Lindell, J.E., "Fluid Force Analysis and Accelerating Sphere Tests", *Journal of Hydraulic Division, ASCE*, 97, No. HY6, pp. 805-817, 1971.
31. Strickland, J. H. and Macha, M.; "Preliminary Characterization of Parachute Wake Recontact", *Journal of Aircraft*, 27, 501 – 506, 1990.
32. Tatsuno, M., and Taneda, S., "Visualization of the Unsteady Flow Past Cylinders and Plates from a Steady Speed", *Journal of the Physical Society of Japan*, 31, 1266-1274, 1971.
33. Lamb, H., "On the Motion of Solids Through a Liquid", *Hydrodynamics*, 6<sup>th</sup> edition, Dover, New York NY, 1945, pp. 160-201.
34. Thomasson, P. G. "Equations of Motion of a Vehicle in a Moving Fluid", *Journal of Aircraft*, 37, 630-639, 2000.
35. T. W. Knacke, "Parachute Recovery Systems Design Manual"; Para Publishing (Santa Barbara, CA 1992).
36. Potvin, J., Montanez, R. and Peek, G.; "The Parks College Ram-Air Parachute Deployment Study: a Status Report". AIAA-97-1426; 14<sup>th</sup> AIAA Aerodynamic Decelerator Systems Conference and Seminar, San Francisco CA, June 1997.
37. Potvin, J., Montanez, R. and Peek, G.; "The Parks College Ram-Air Parachute Deployment Study". Proceedings of the 1997 Parachute Industry Association International Symposium, Houston, TX, February 9-13, 1997.
38. Potvin, J., and Peek, G.; "The Parks College Parachute Research Group: Putting Science at the Service of Riggers and Manufacturers"; Proceedings of the 1999

*Parachute Industry Association International Symposium*, San Diego, CA, January 10-14, 1999.

39. Lee, C. K., "Modeling of Parachute Opening: an Experimental Investigation", *Journal of Aircraft*, **26**, 444 – 451, 1989.

40. Lee, C.K., "Experimental Investigation of Full-Scale and Model Parachute Opening", AIAA-84-0820, *8<sup>th</sup> AIAA Aerodynamic Decelerator Systems Technology Conference*, Hyannis, MA, 1984, pp. 215-223.

41. Ludtke, W. P., "A Technique for the Calculation fo the Opening-Shock Forces for Several Types of solid Cloth Parachutes", AIAA-73-477. *4<sup>th</sup> AIAA Aerodynamic Decelerator Systems Technology Conference*, Palm Springs, CA, 1973; pp. 176 – 185.

42. Wolf, D., "Opening Shock", AIAA-99-1702, *15<sup>th</sup> AIAA Aerodynamic Decelerator Systems Technology Conference*, Toulouse, France, 1999; pp.253-256.

Table 1.

Values of exponent  $\beta'-2$  for different initial conditions where  $F_{ext}(t < t_i) \neq F_{ext}(t > t_i)$ .

|   |   |   |   |  |
|---|---|---|---|--|
| $F_{ext} = 0, v_T = 0$<br>$t_i \leq t \leq t_f$ | $a(t < t_i) = 0$<br>$v(t < t_i) = v_T$<br>$C_D(t < t_i) = C_D^{steady}$ | <i>Accelerating disk, <math>t &lt; t_i</math></i><br>$0 \leq \delta \leq 0.3$ | <i>Accelerating disk, <math>t &lt; t_i</math></i><br>$0.3 \leq \delta \leq 10.0$                    | <i>Accelerating disk, <math>t &lt; t_i</math></i><br>$\delta \gg 10.0$                                 |
| 0   | 0   | $\frac{\delta_{i-\epsilon}^{0.65} \ln 4.67}{\ln(v_i / v_T)}$                  | $\frac{\ln\left(\frac{(20 \cdot \delta_{i-\epsilon})^{0.46}}{C_D^{steady}}\right)}{\ln(v_i / v_T)}$ | $\frac{\ln\left(1 + \left(\frac{2K\delta_{i-\epsilon}}{SDC_D^{steady}}\right)\right)}{\ln(v_i / v_T)}$ |

Table 2.

Values of  $C_D^{init}$  for different initial conditions, where  $F_{ext}(t < t_i) \neq F_{ext}(t > t_i)$ .

|   |   |   |  |  |
|---|---|---|--|--|
| $F_{ext} = 0, v_T = 0$<br>$t_i \leq t \leq t_f$ | $a(t < t_i) = 0$<br>$v(t < t_i) = v_T$<br>$C_D(t < t_i) = C_D^{steady}$ | <i>Accelerating disk, <math>t &lt; t_i</math>,<br/> <math>0 \leq \delta \leq 0.3</math></i> | <i>Accelerating disk, <math>t &lt; t_i</math>,<br/> <math>0.3 \leq \delta \leq 10.0</math></i> | <i>Accelerating disk, <math>t &lt; t_i</math>,<br/> <math>\delta \gg 10.0</math></i> |
| $C_D^{init}$                                    | $C_D^{steady}$  | $C_D^{steady} 4.67 \delta_{i-\varepsilon}^{0.65}$   | $(20 \cdot \delta_{i-\varepsilon})^{0.46}$   | $\frac{2KV \delta_{i-\varepsilon}}{SD}$  |

Table 3.

Calculated deceleration properties of the parachutes studied in the test drops.

Input data displayed in figures 4 through 7.

|                             | Half-scale cross<br>D = 10.7 ft | Half-scale C-9<br>D= 15.0 ft | Full-scale cross<br>D = 24.0 ft | Full-scale Navy<br>D = 28.0 ft |
|-----------------------------|---------------------------------|------------------------------|---------------------------------|--------------------------------|
| $C_D^{init} / C_D^{steady}$ | 3.25                            | 3.12                         | 1.06                            | $\approx 1.00$                 |
| $v/v_T$                     | 1.43                            | 1.33                         | 1.63                            | 1.52 & 1.41                    |
| $\beta'$                    | 5.29                            | 5.98                         | 2.12                            | 1.95 & 2.13                    |

## Figure Captions

Figure 1. Accelerating object as viewed from different Galilean reference frames.

Figure 2. Top view of the A-22 container payload model, with packed parachute on the top tray. The data acquisition system is visible through the window cut in the carboard.

Figure 3. Close-up view of the A-22 payload, parachute riser and integrated load cell.

Figure 4. Total parachute riser force, per unit payload weight, versus time (sec). Half-scale U.S. Army cruciform parachute. The smooth, continuous line corresponds to the calculated force using equation (26) through (29). The arrow marks the end of inflation and the beginning of the post-inflation deceleration phase.

Figure 5. Total parachute riser force, per unit payload weight, versus time (sec). Half-scale USAF C-9 personnel emergency flat circular parachute. The smooth, continuous line corresponds to the calculated force using equation (26) through (29). The arrow marks the end of inflation and the beginning of the post-inflation deceleration phase.

Figure 6. Total parachute riser force, per unit payload weight, versus time (sec). Full-scale U.S. Navy personnel emergency flat circular parachute. The smooth, continuous lines correspond to the calculated force using equation (26) through (29). The calculated curve with the highest load corresponds to the 90ft/sec, 625 ft<sup>2</sup> case. The arrow marks the end of inflation and the beginning of the post-inflation deceleration phase.

Figure 7. Total parachute riser force, per unit payload weight, versus time (sec). Full-scale U.S. Army cruciform parachute. The smooth, continuous line corresponds to the calculated force using equation (26) through (29). The arrow marks the end of inflation and the beginning of the post-inflation deceleration phase.

Figure 8. Total parachute riser force, per unit payload weight, versus time (sec) - full-scale U.S. Army cruciform parachute. The smooth, continuous lines correspond to the calculated force using equation (26) through (29). The lines feature the same input values as in figure 7, except for  $t_f$ ,  $v_0$  and  $C_D S_f$  which are: 1.5 sec, 95 fps, 325 ft<sup>2</sup> (grey line); 1.7 sec, 120 fps, 325 ft<sup>2</sup> (black line); 1.5 sec, 95 fps, 450 ft<sup>2</sup> (diamonds). The discontinuity on the right-hand-side of the calculated curves corresponds to the end of inflation and the beginning of the post-inflation deceleration phase.

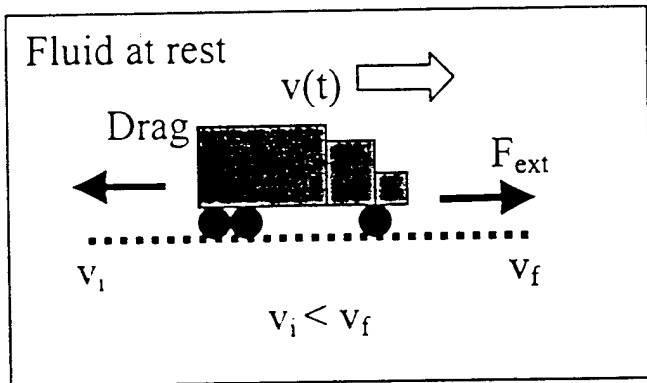
Figure 9. Evolution of the calculated drag coefficient versus time (sec) during the post-inflation deceleration phase. Half-scale U.S. Army cruciform parachute. Same input parameters as figure 4.

Figure 10. Evolution of the calculated drag coefficient versus time (sec) during the post-inflation deceleration phase. Half-scale USAF C-9 personnel emergency flat circular parachute. Same input parameters as figure 5.

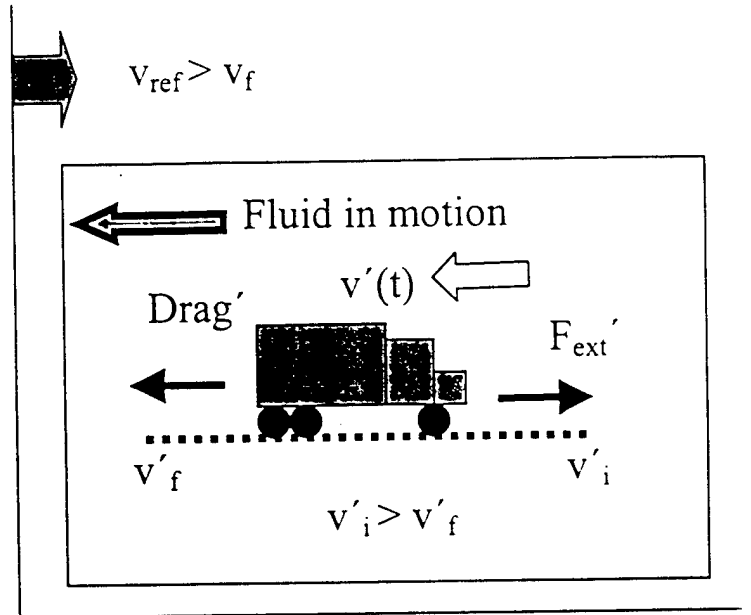
Figure 11. Evolution of the calculated drag coefficient versus time (sec) during the post-inflation deceleration phase. Full-scale U.S. Navy personnel emergency flat circular parachute. Same input parameters as figure 6, with the upwards-pointing curve corresponding to the 90ft/sec, 625 ft<sup>2</sup> case.

Figure 12. Evolution of the calculated drag coefficient versus time (sec) during the post-inflation deceleration phase. Full-scale U.S. Army cruciform parachute. Same input parameters as figure 7.

Figure 1



(a)



(b)

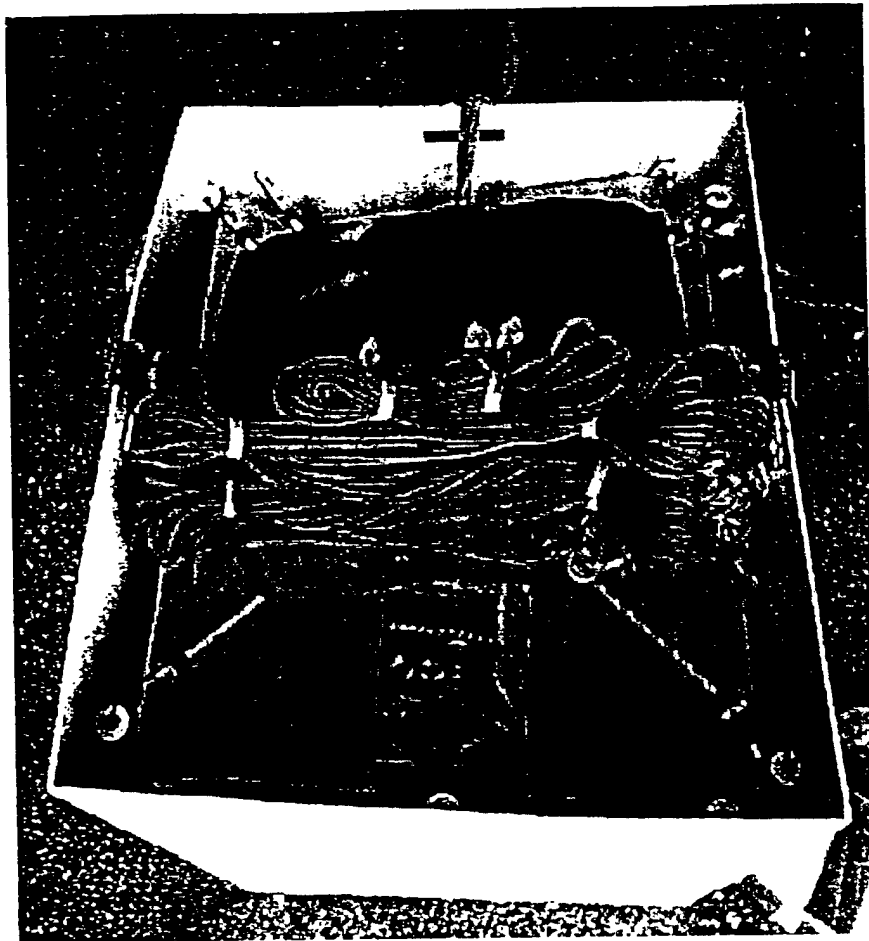


Figure 2

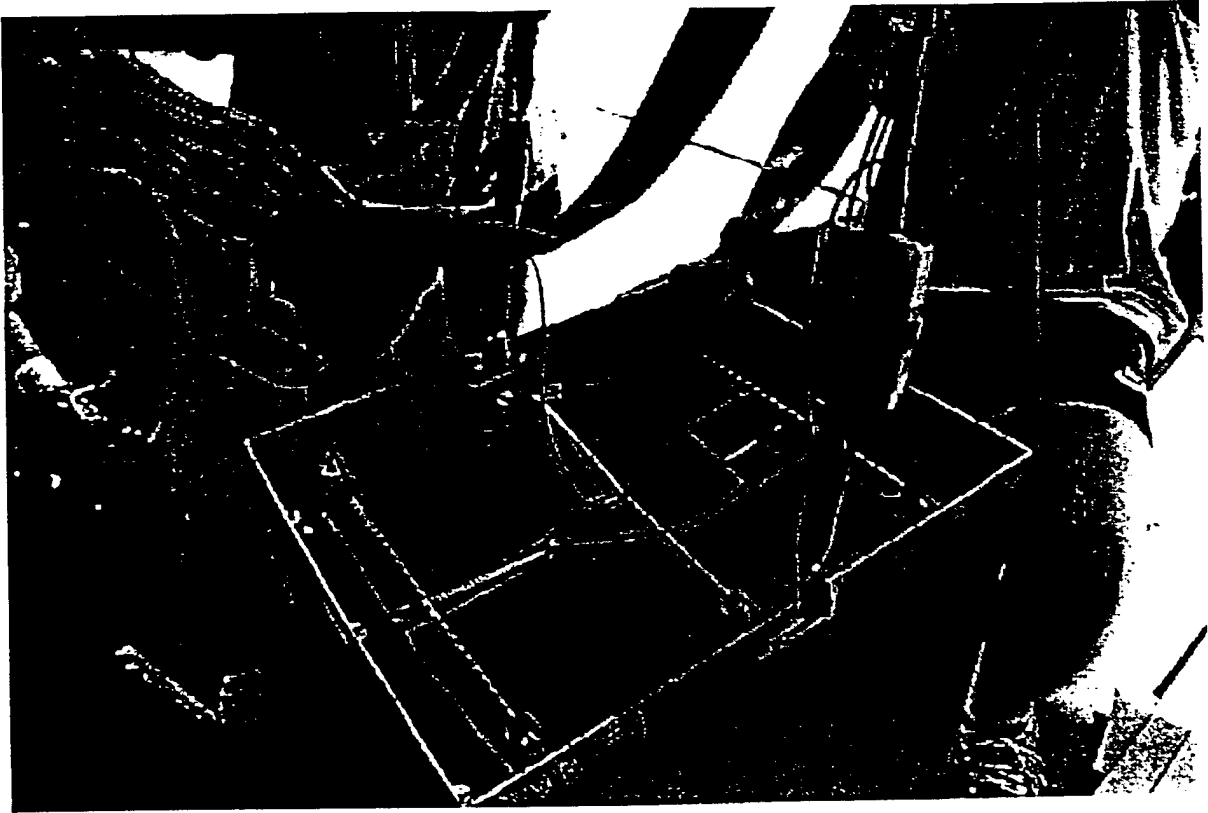


Figure 3.

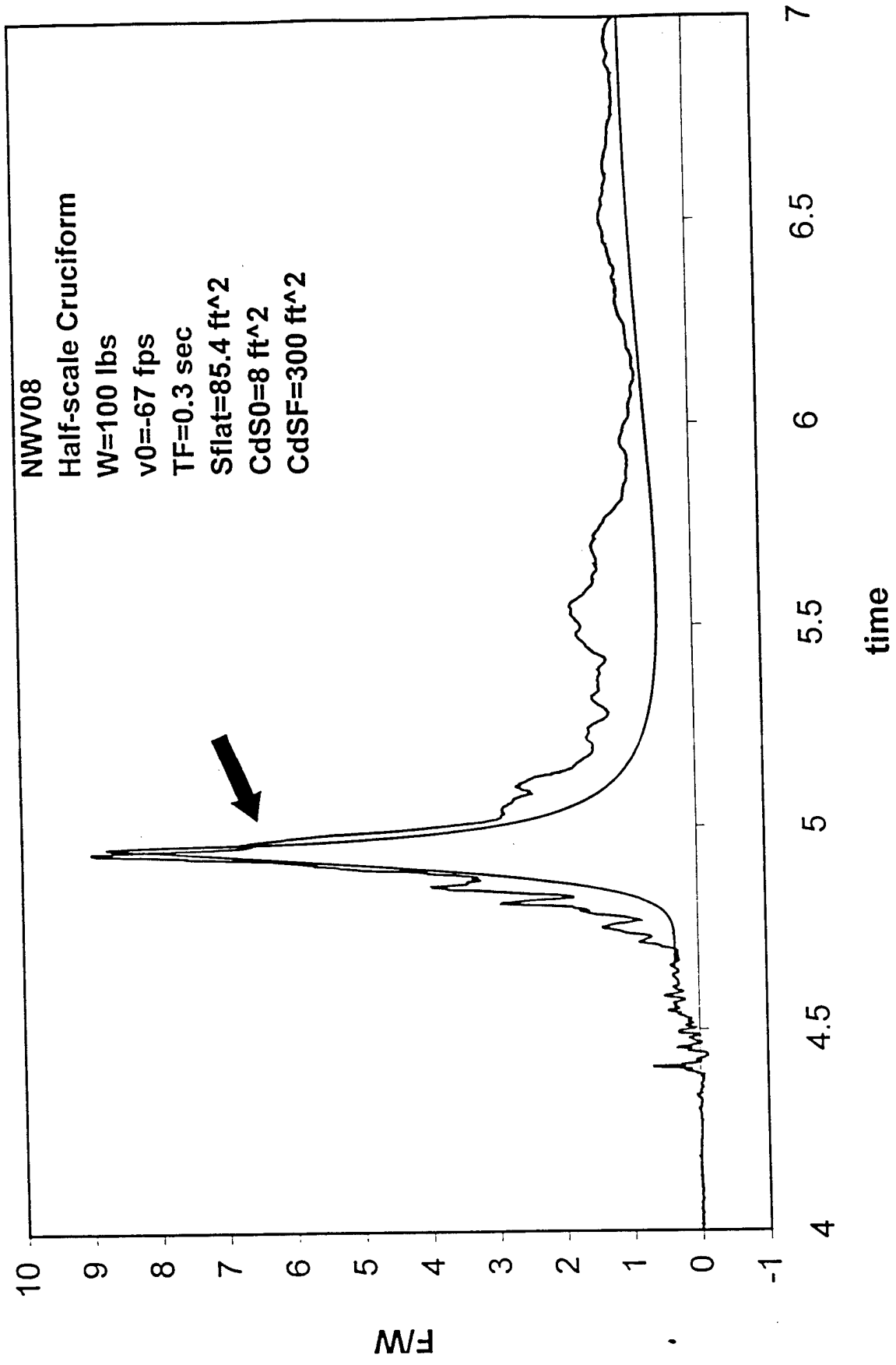
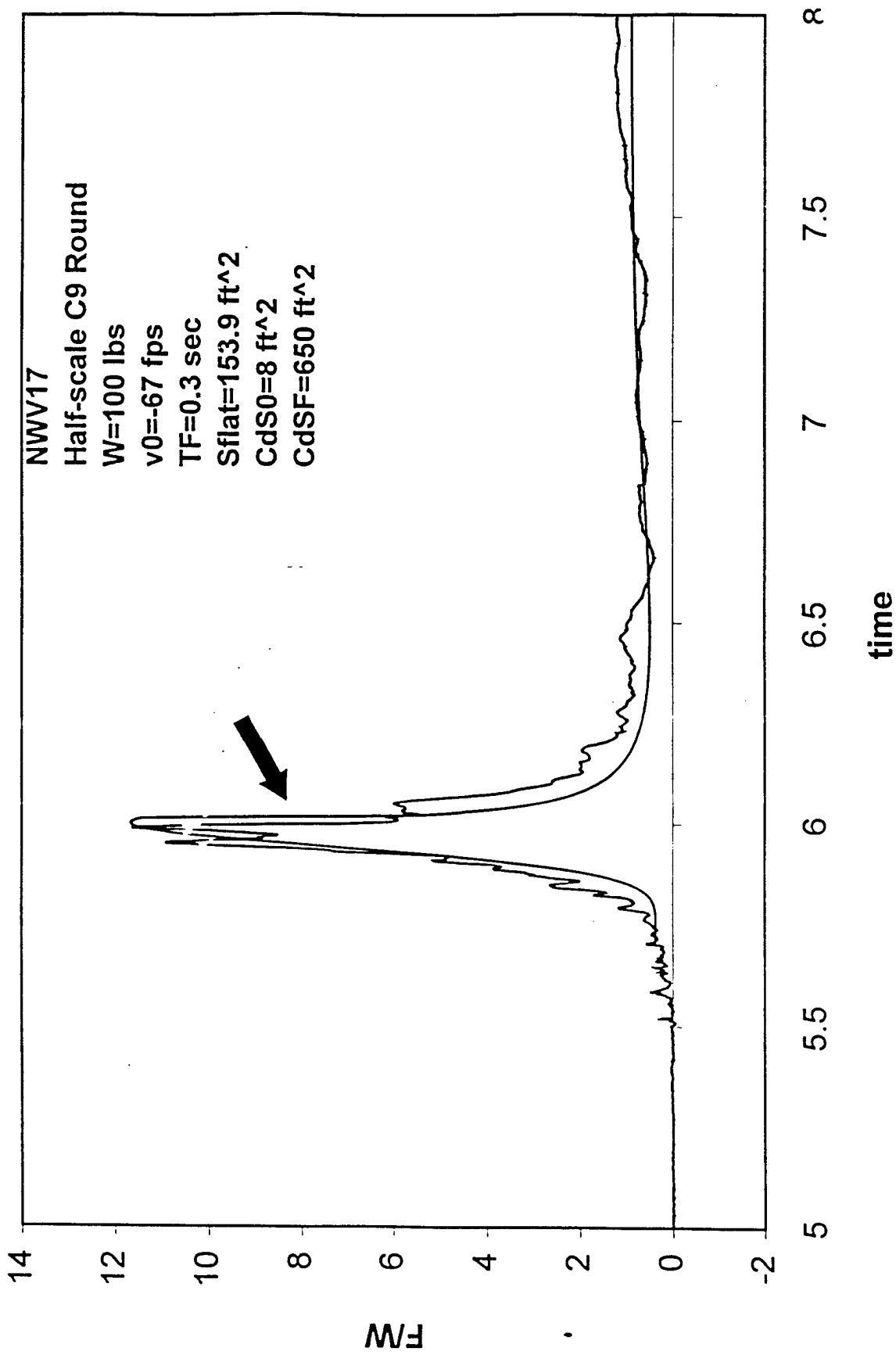


Fig 4



Figs

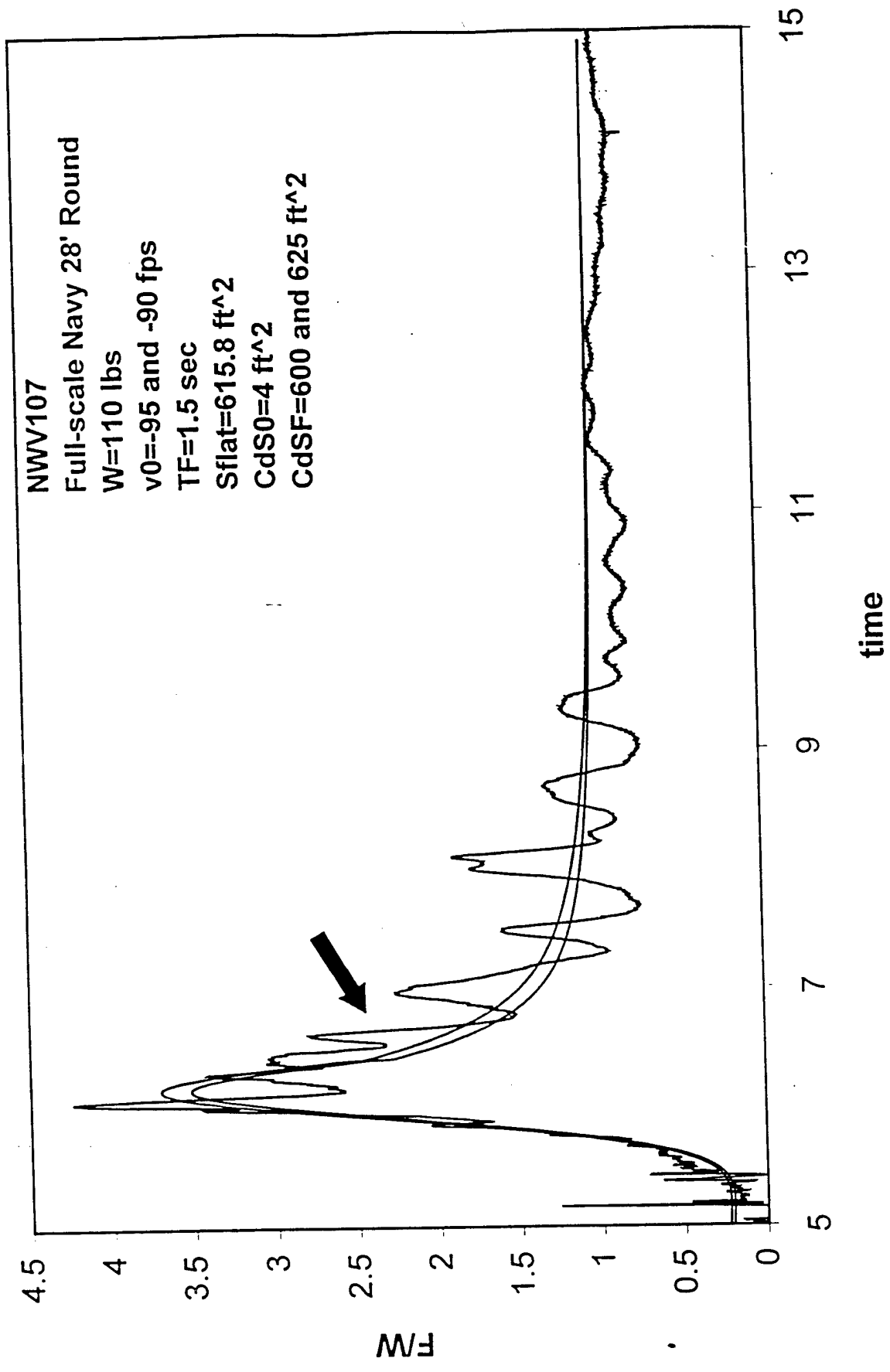


Fig 6

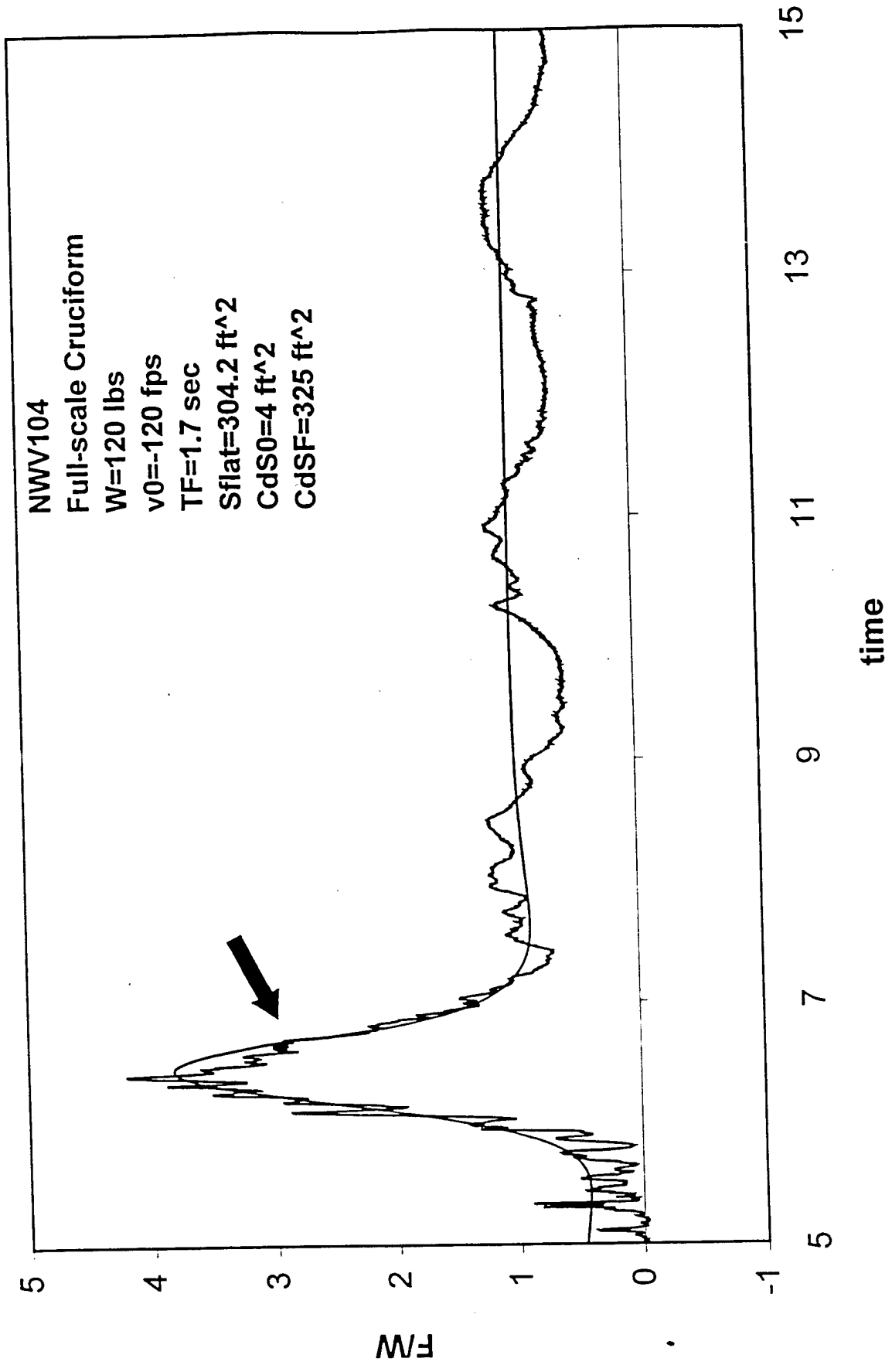


Fig 7

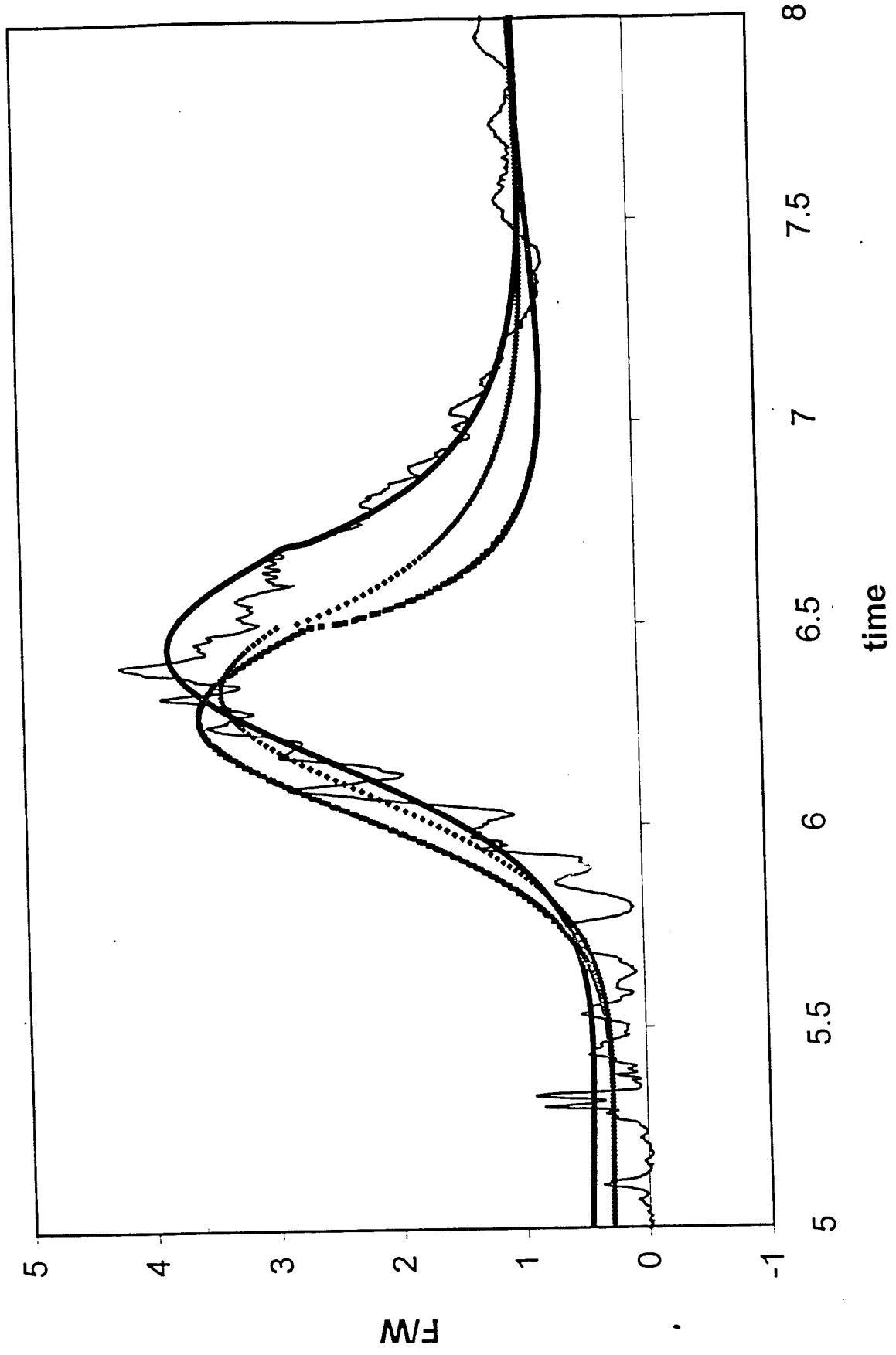


Fig 8

3

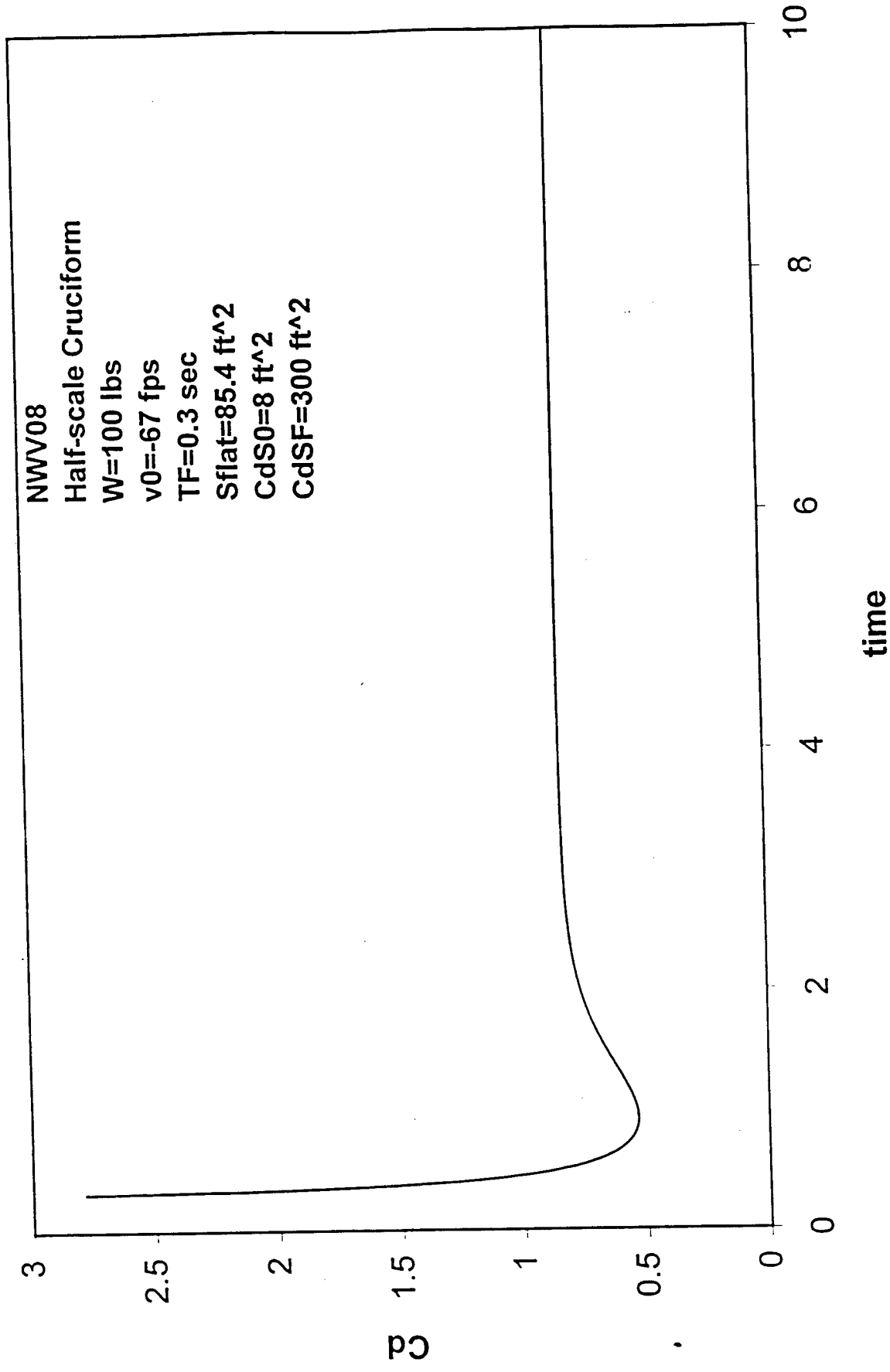
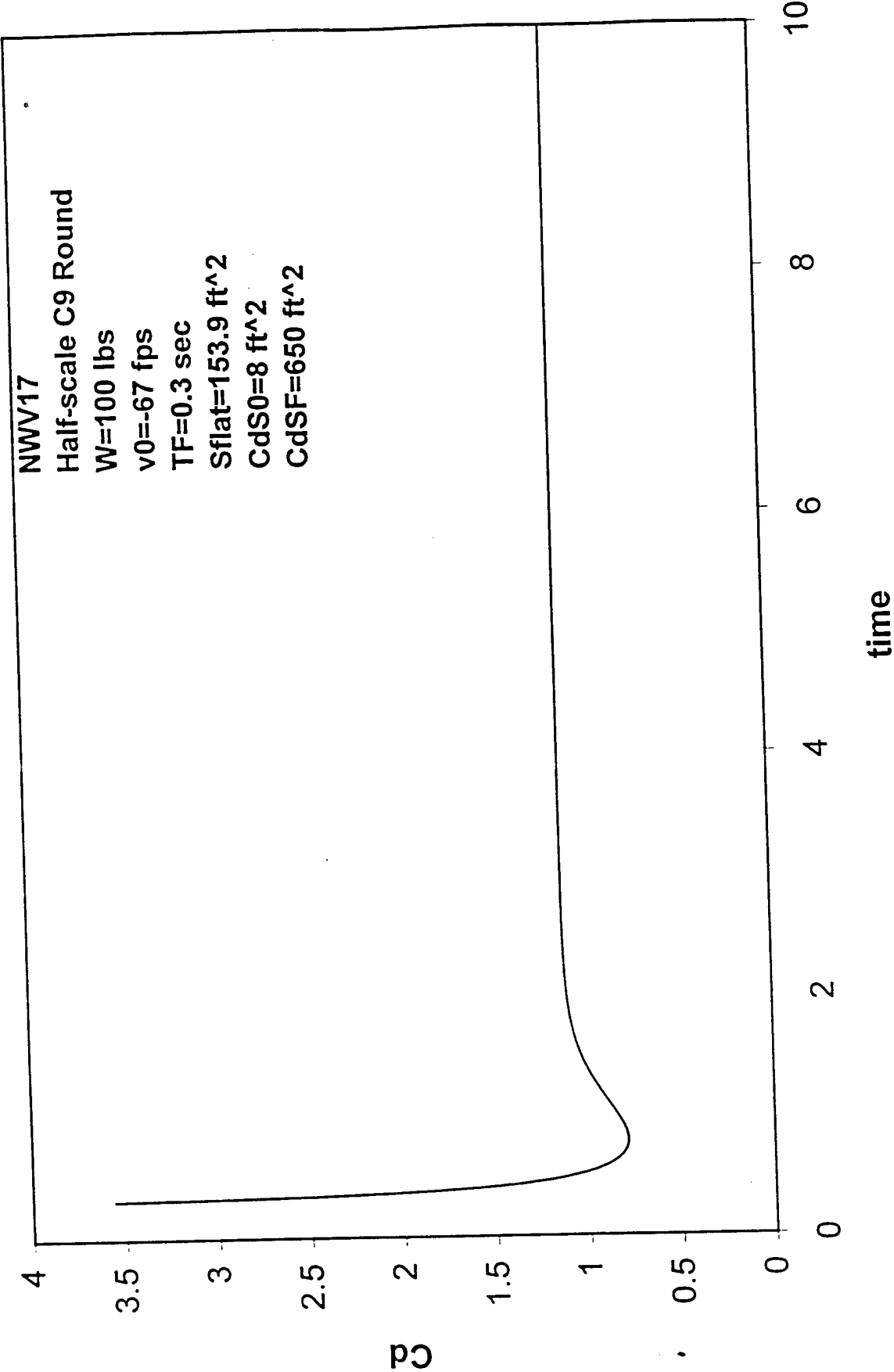


Fig 9



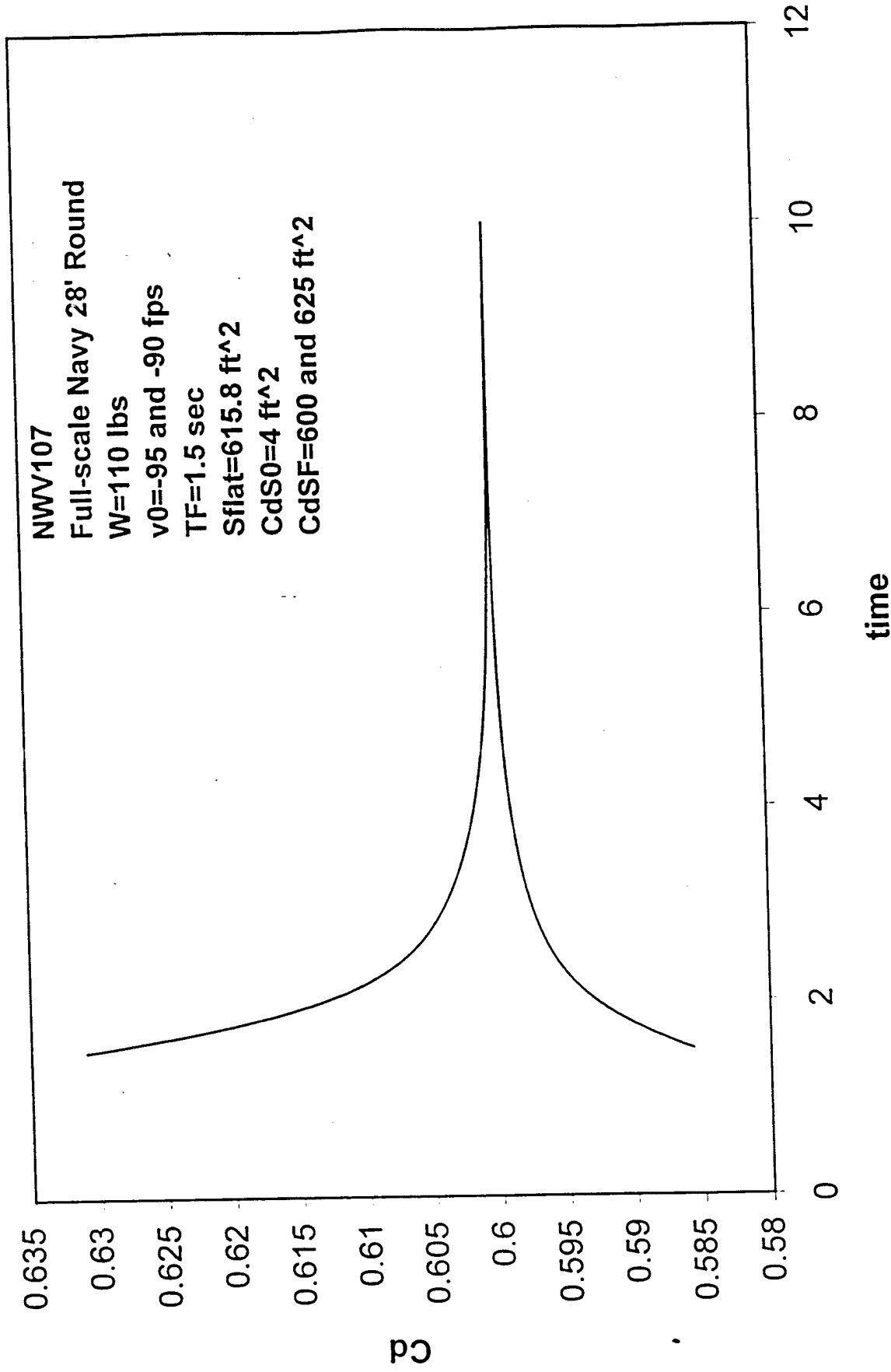


Fig 11

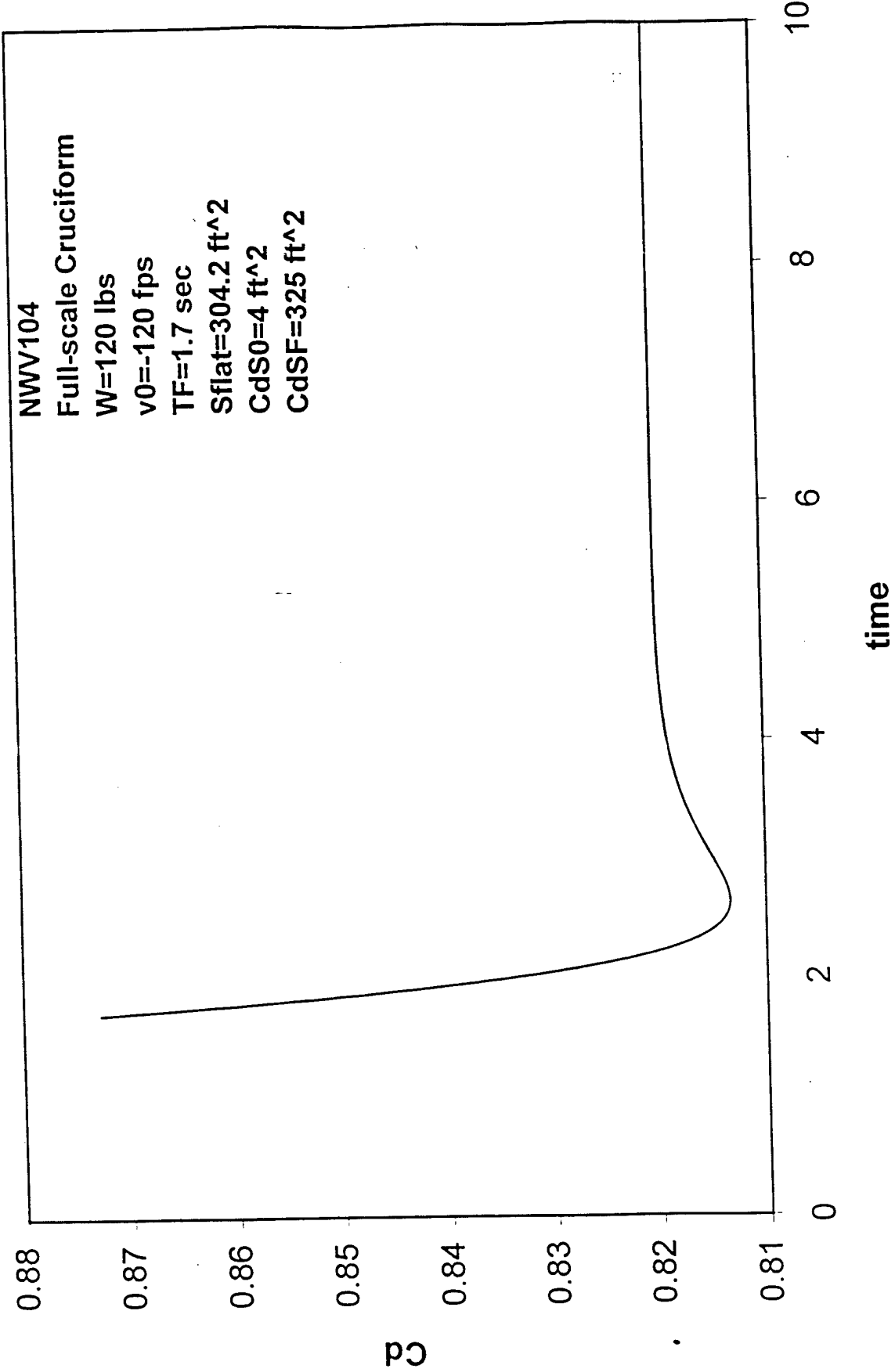
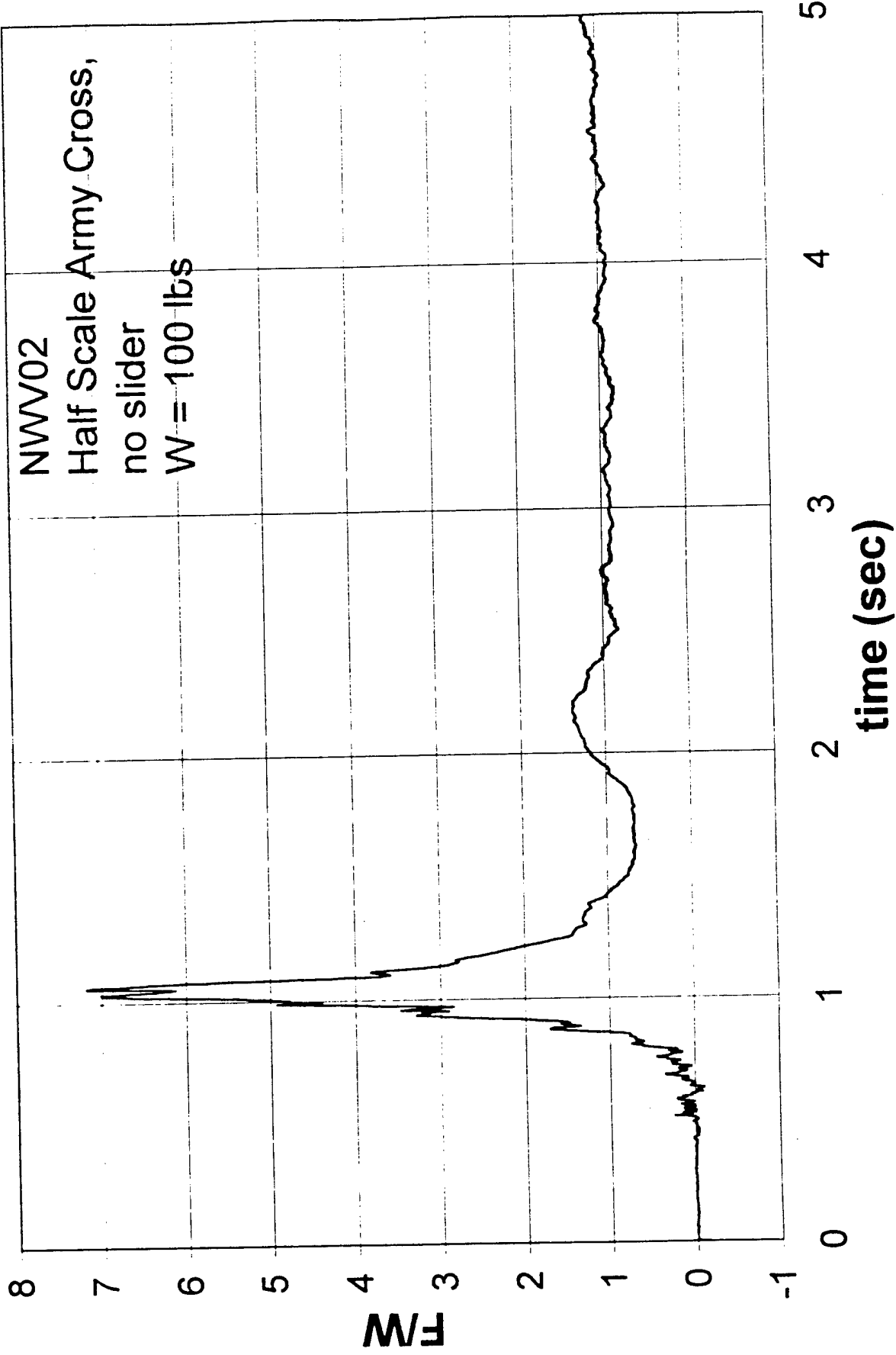
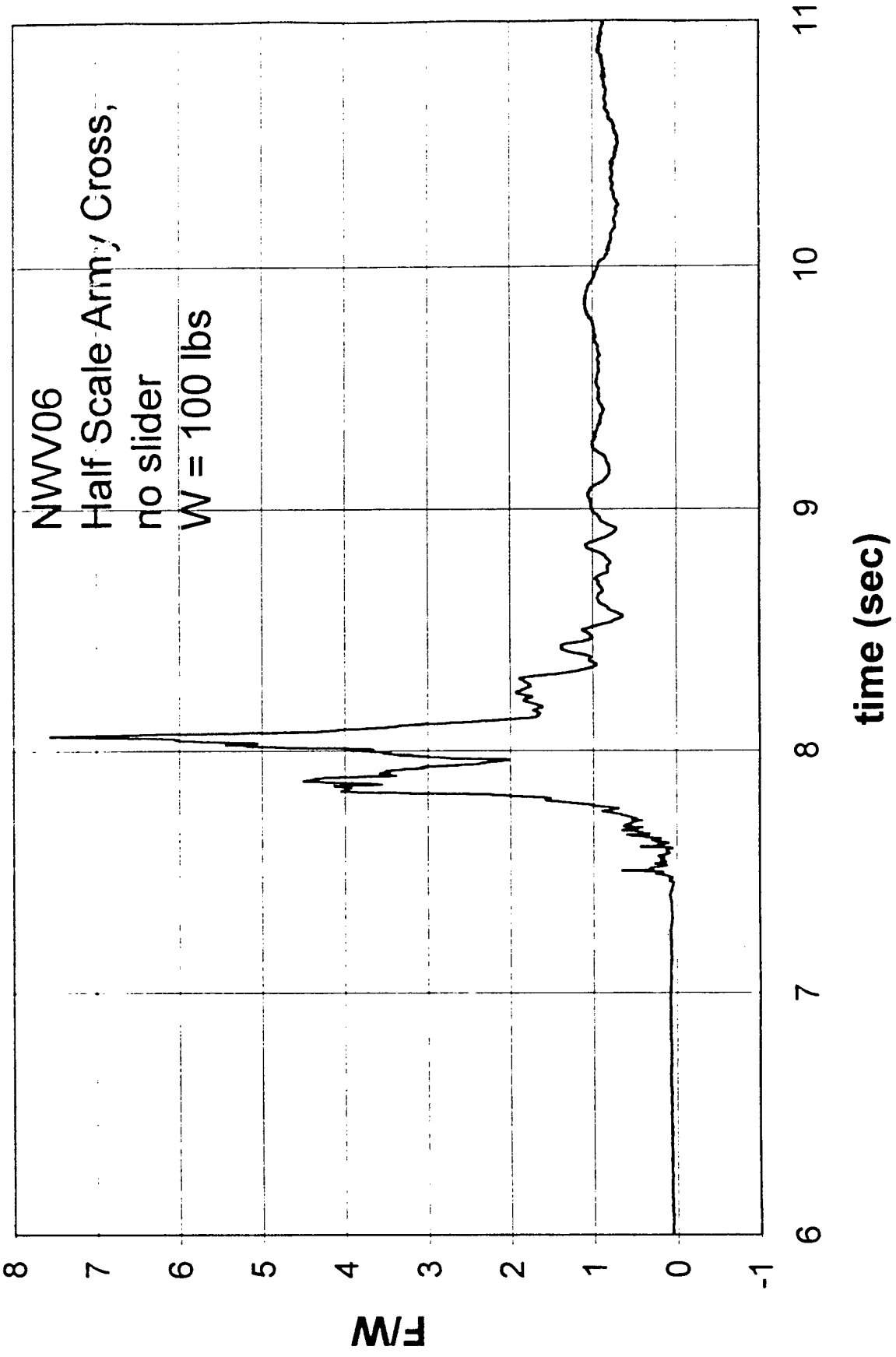


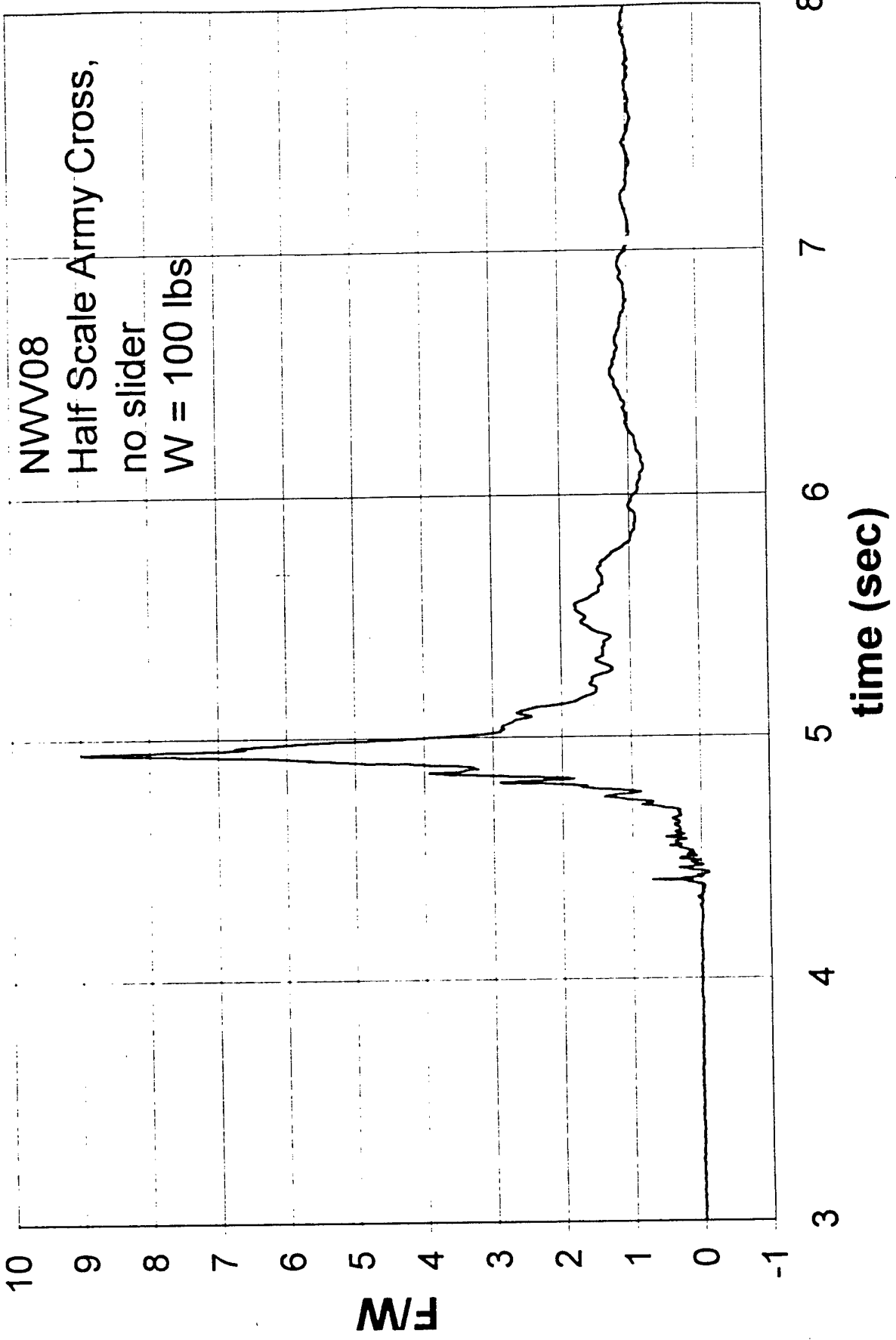
Fig 1A

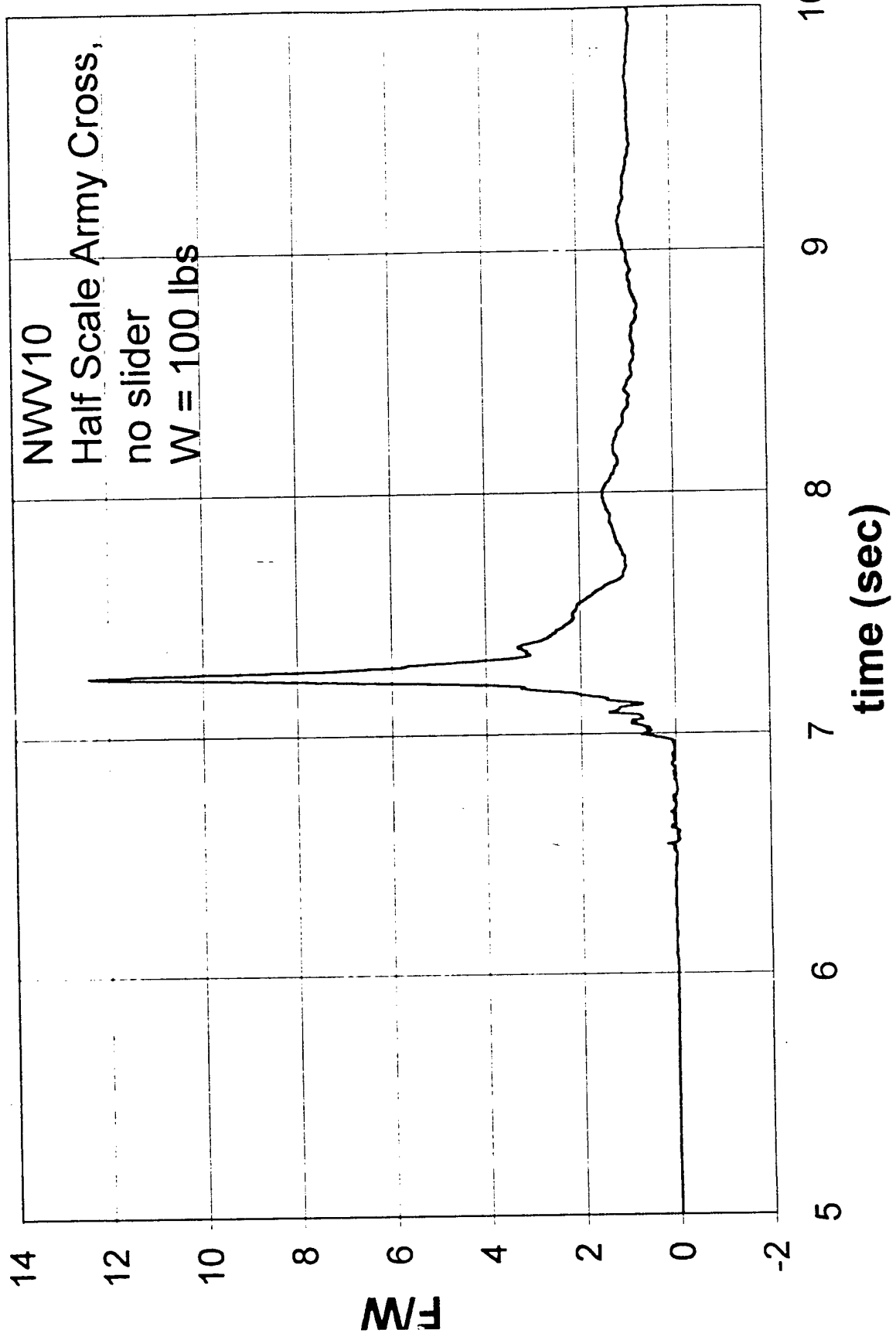
**APPENDIX 3.**

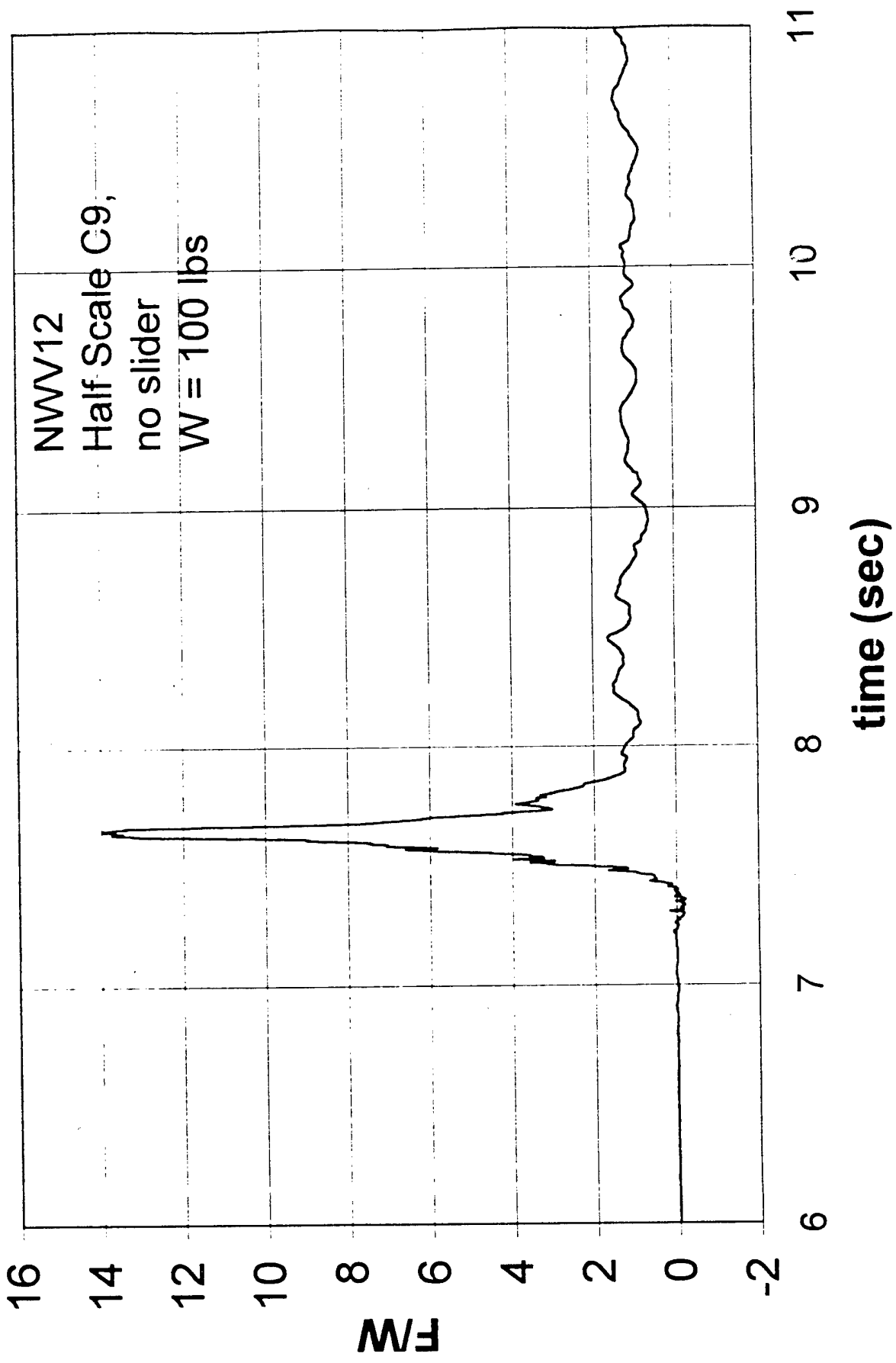
**TIME PLOTS OF THE MEASURED RISER LOADING**

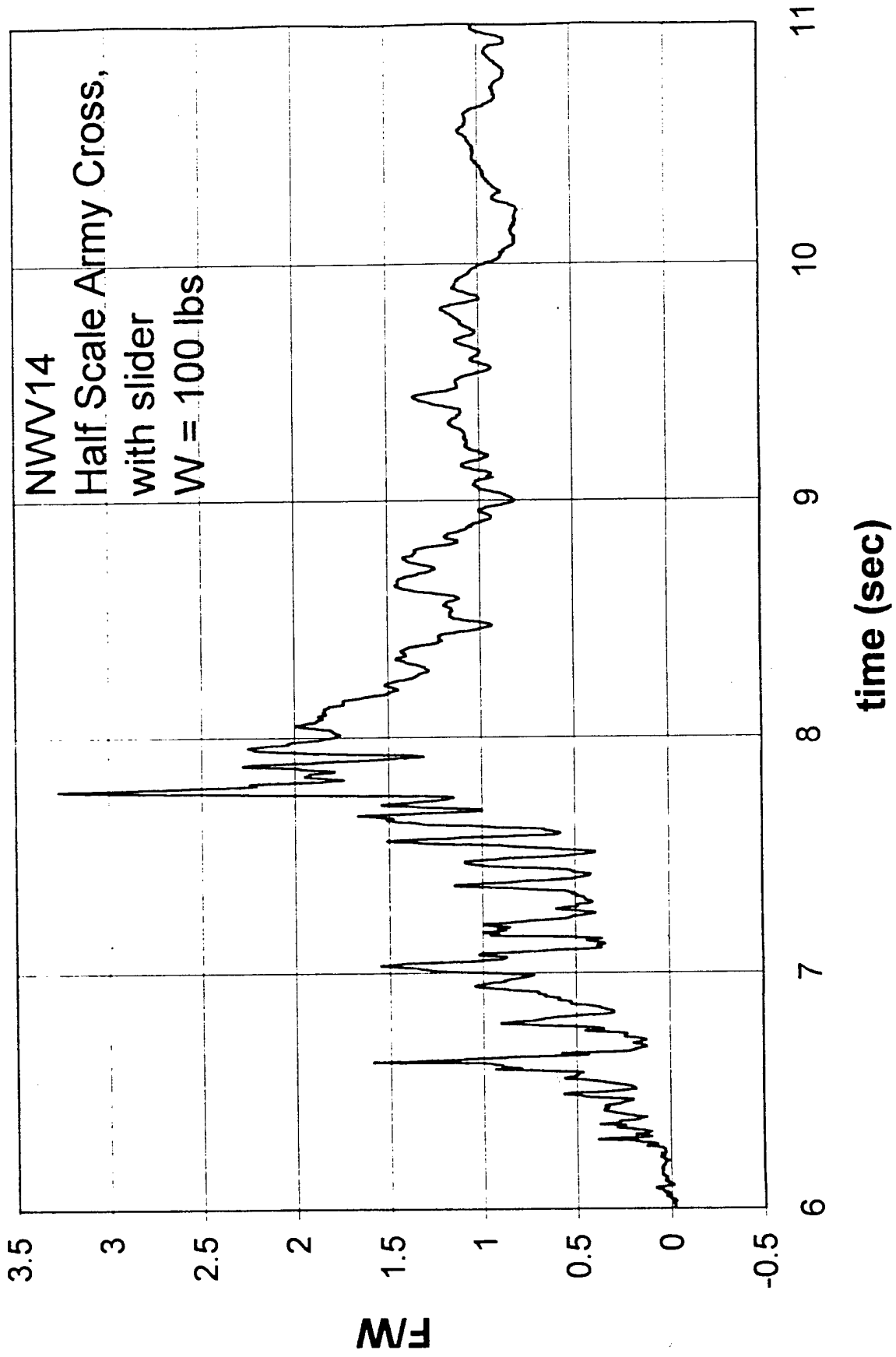


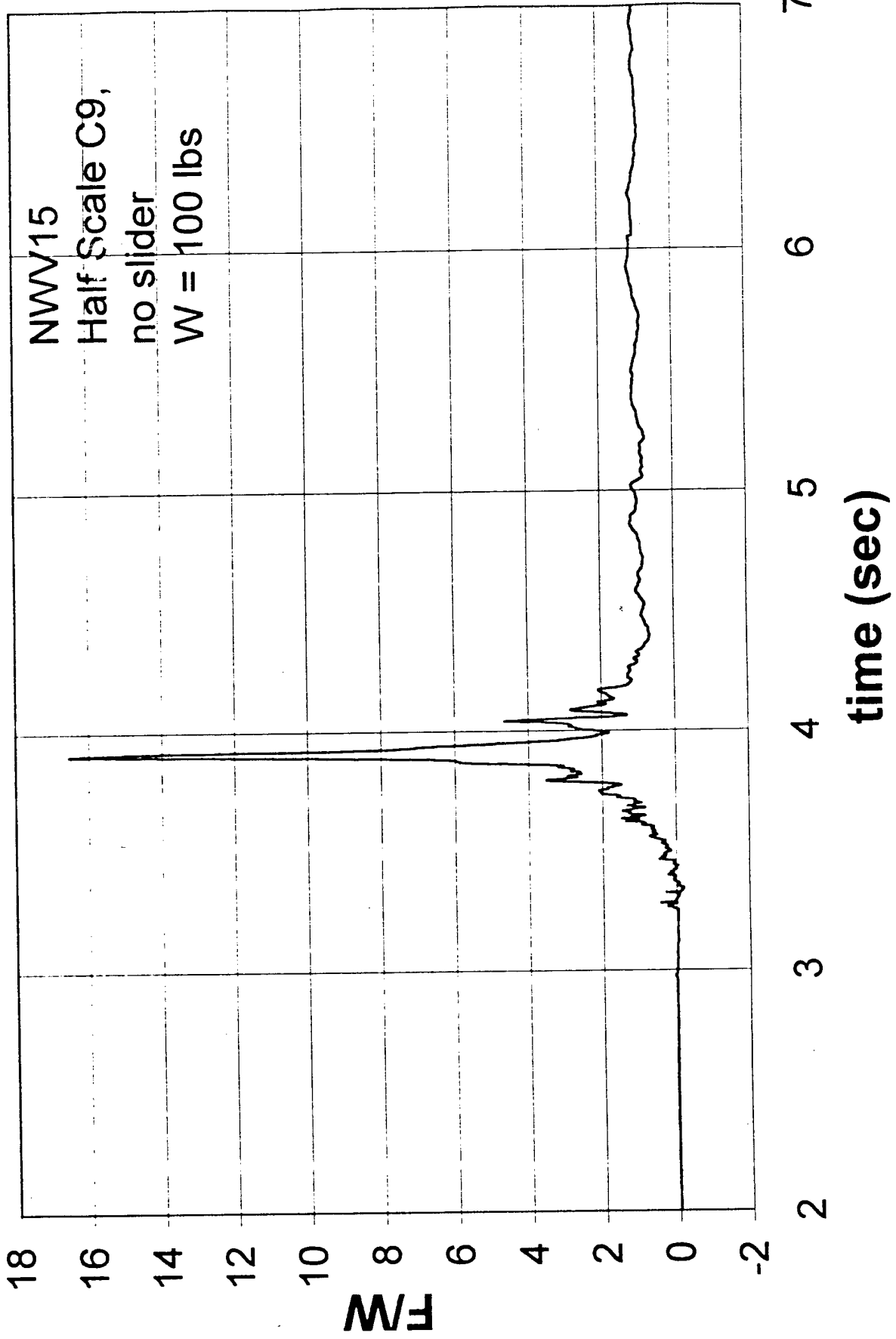


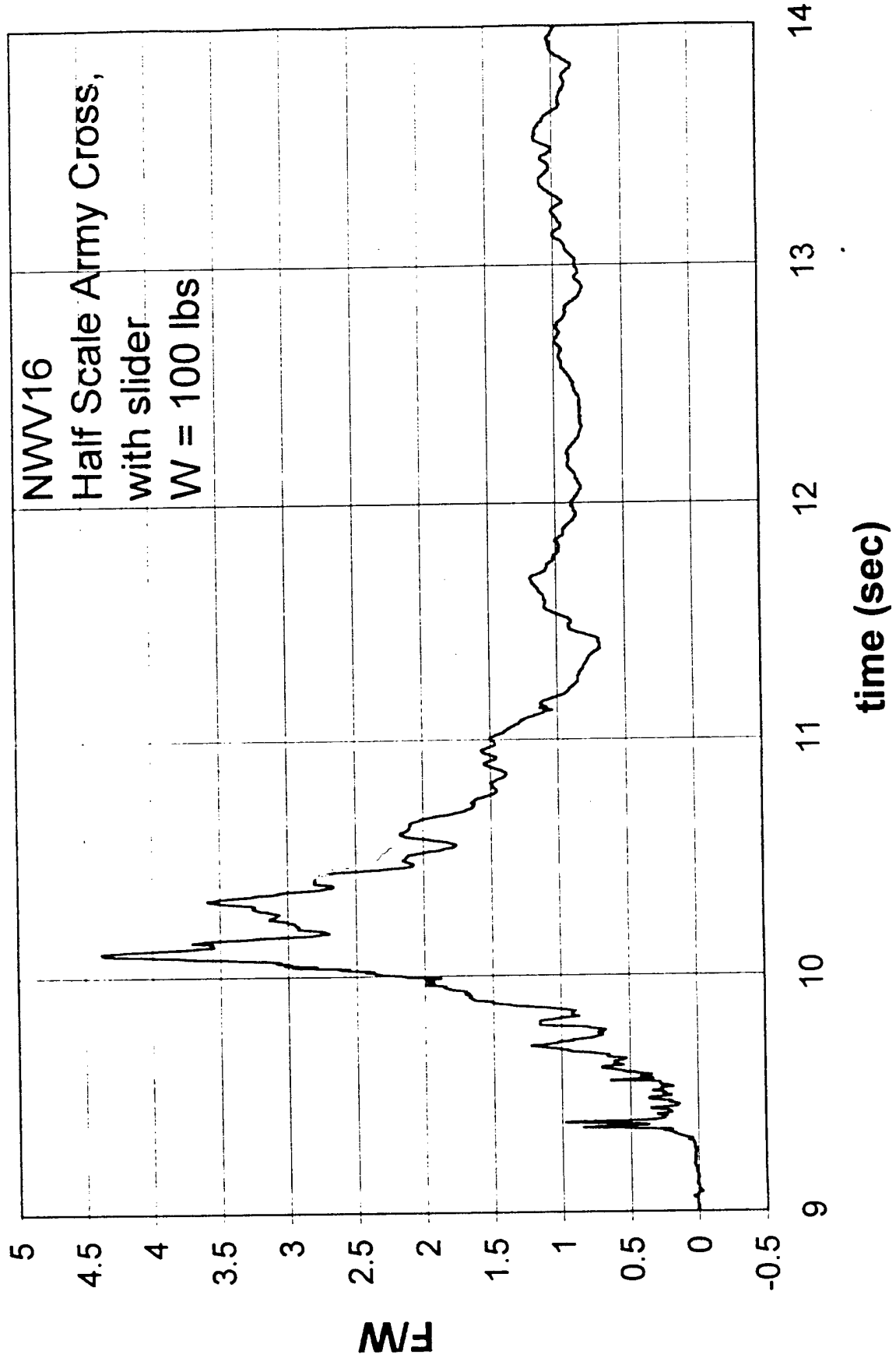


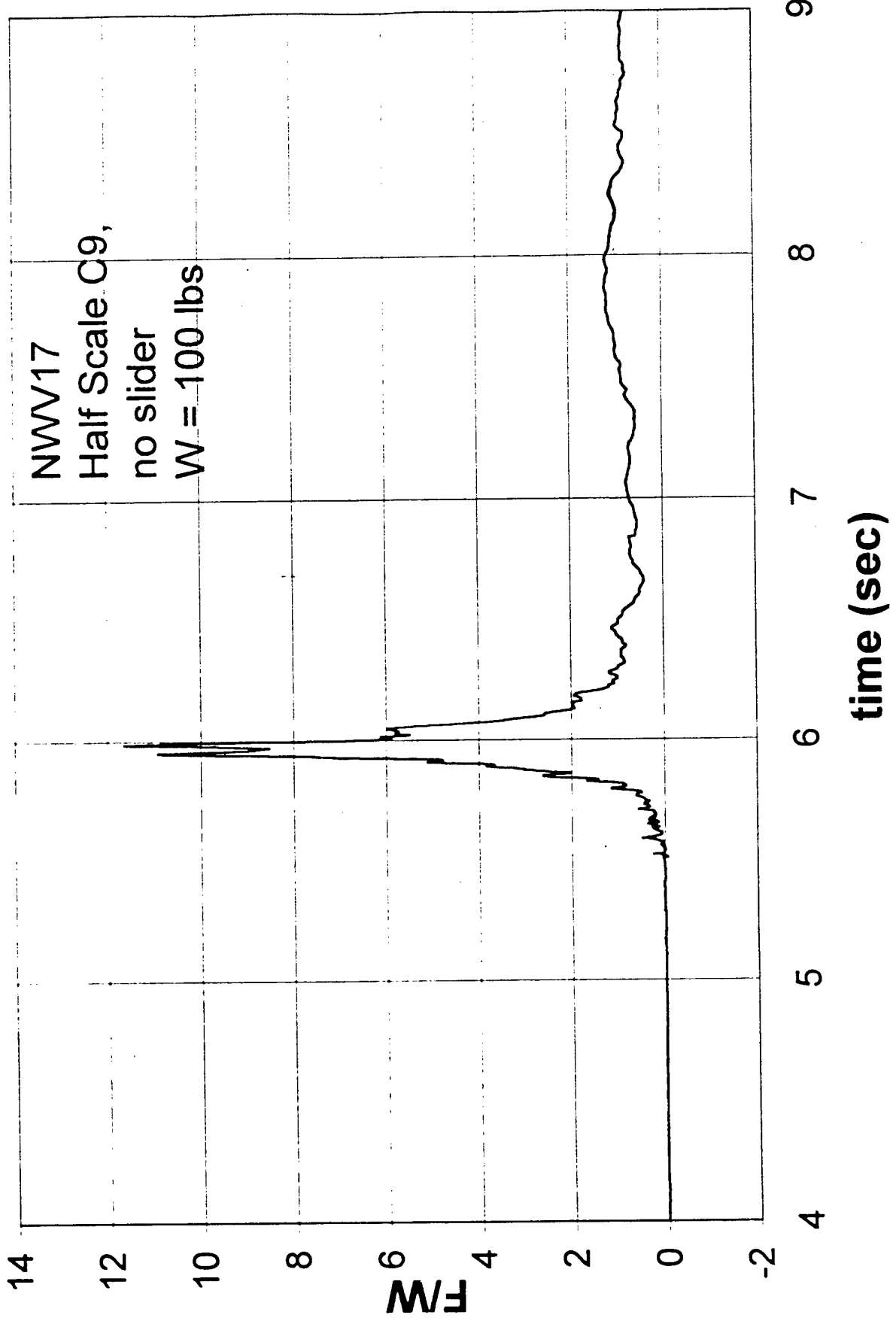


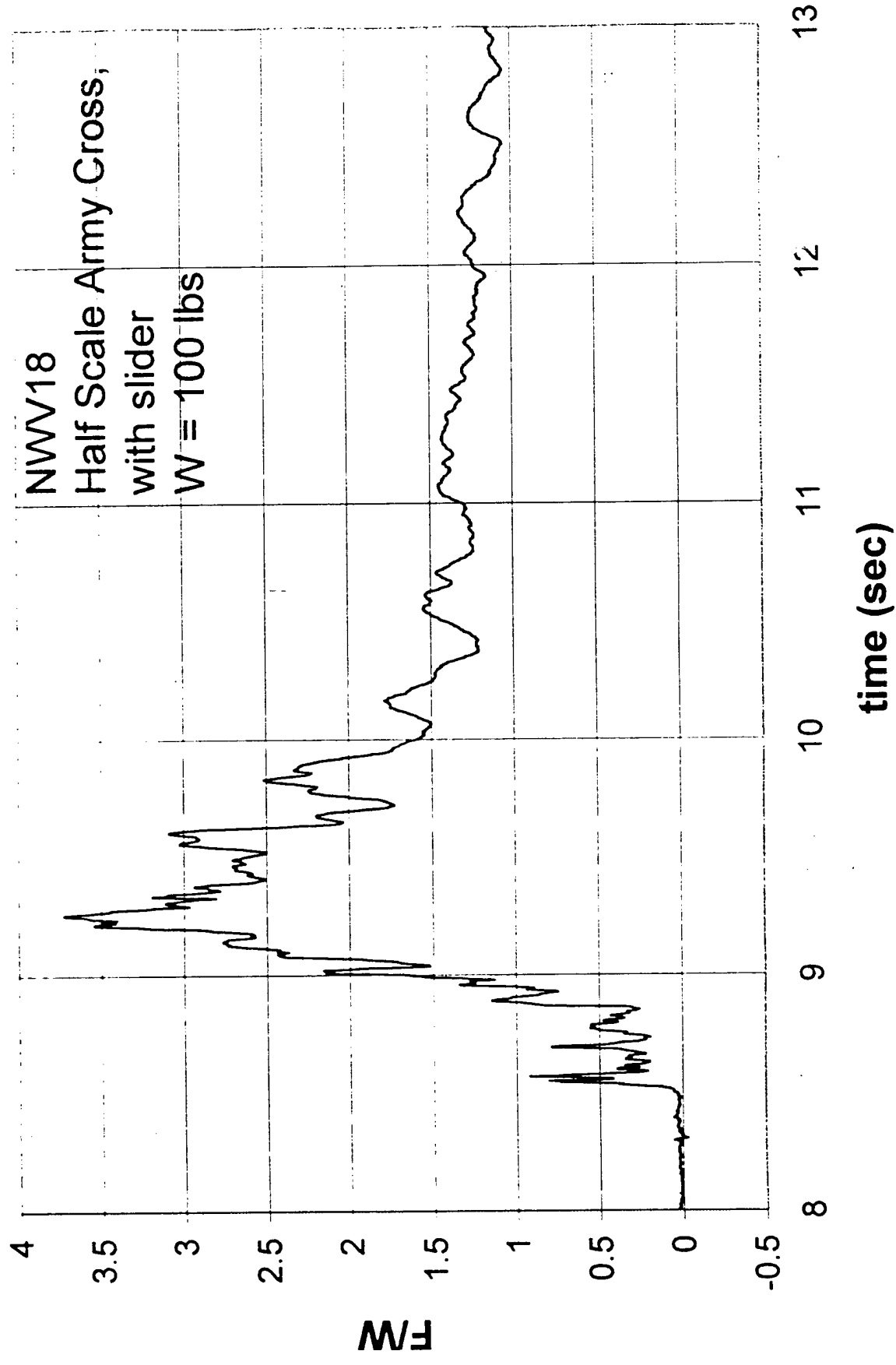


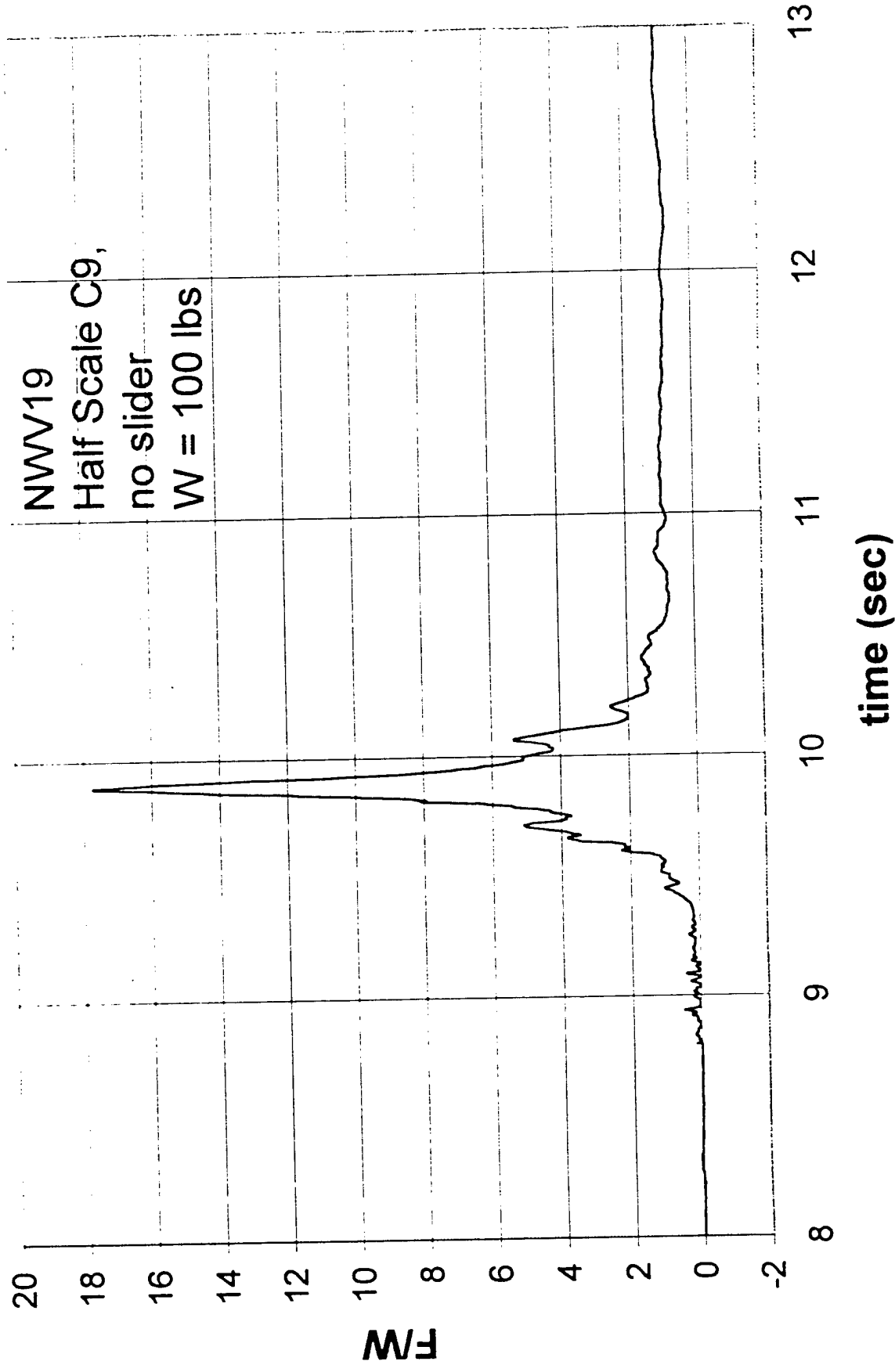


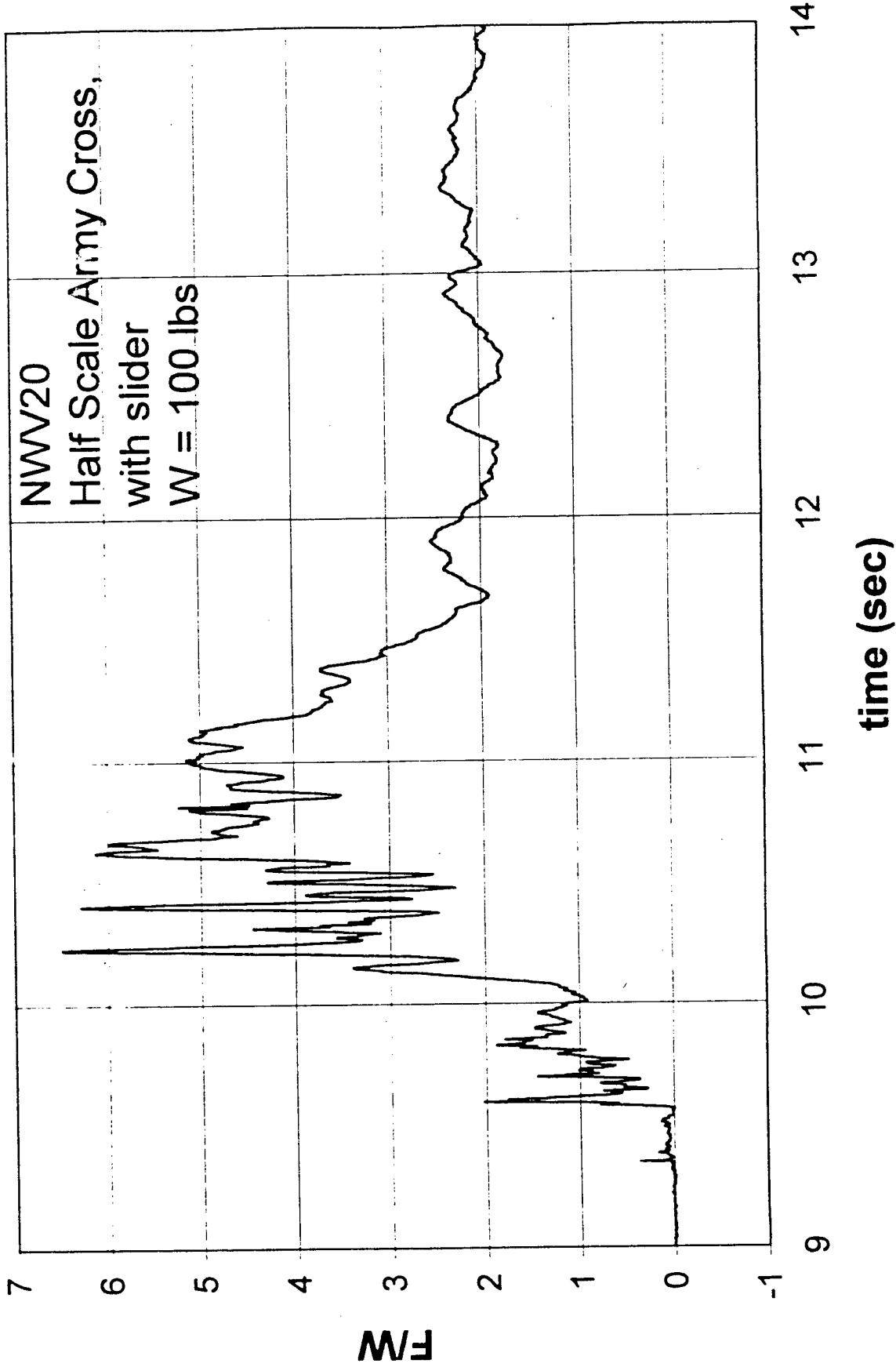


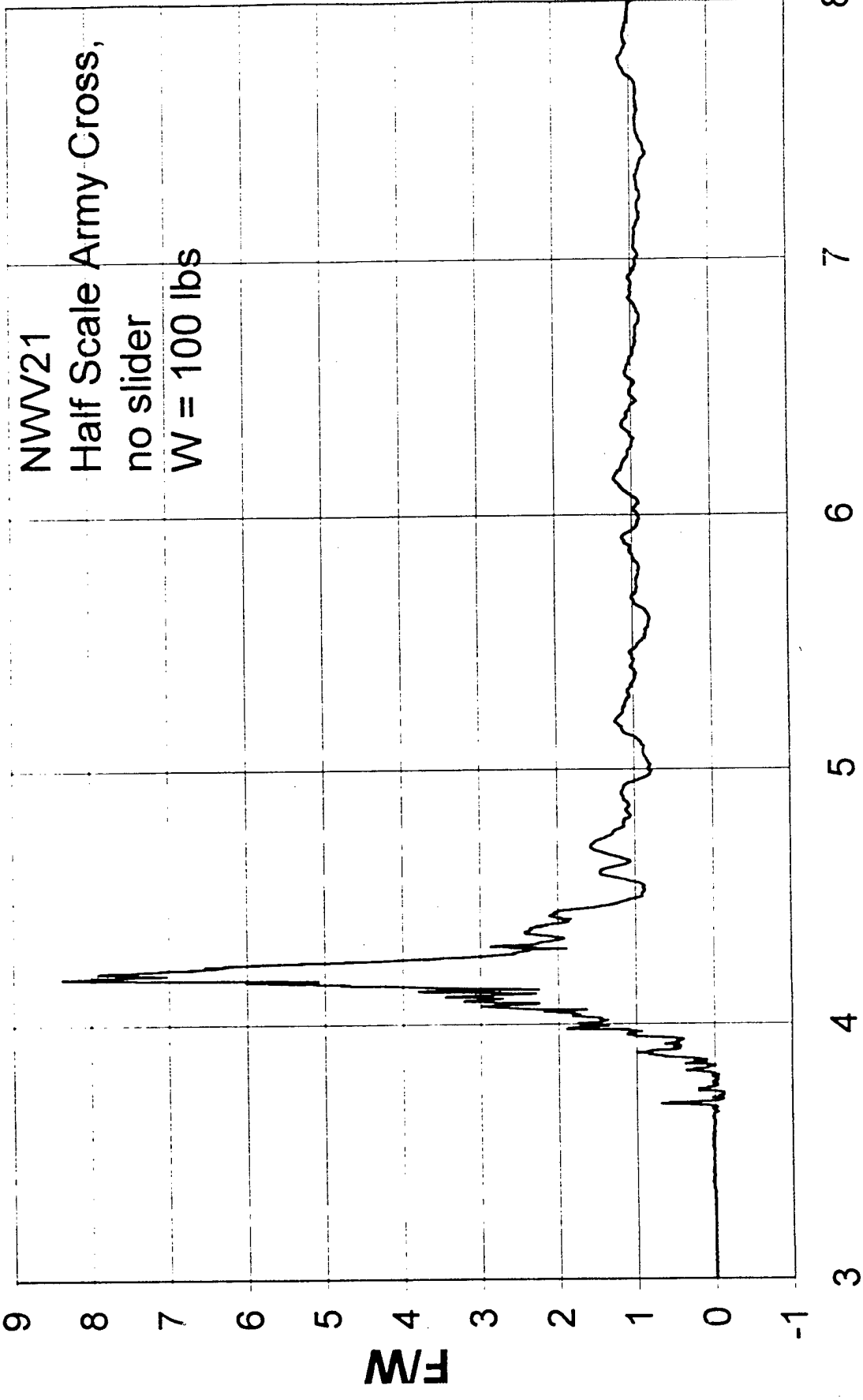






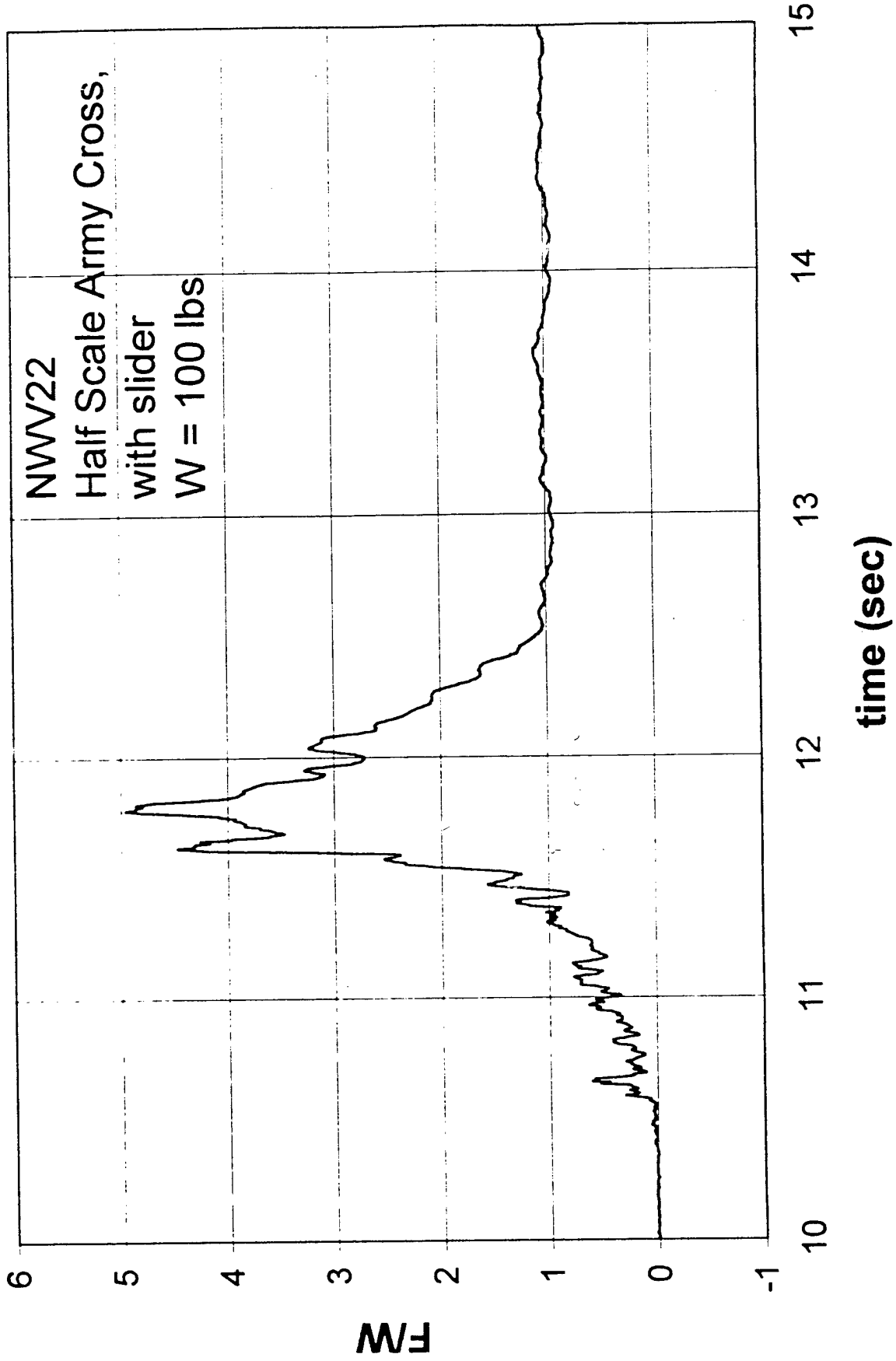


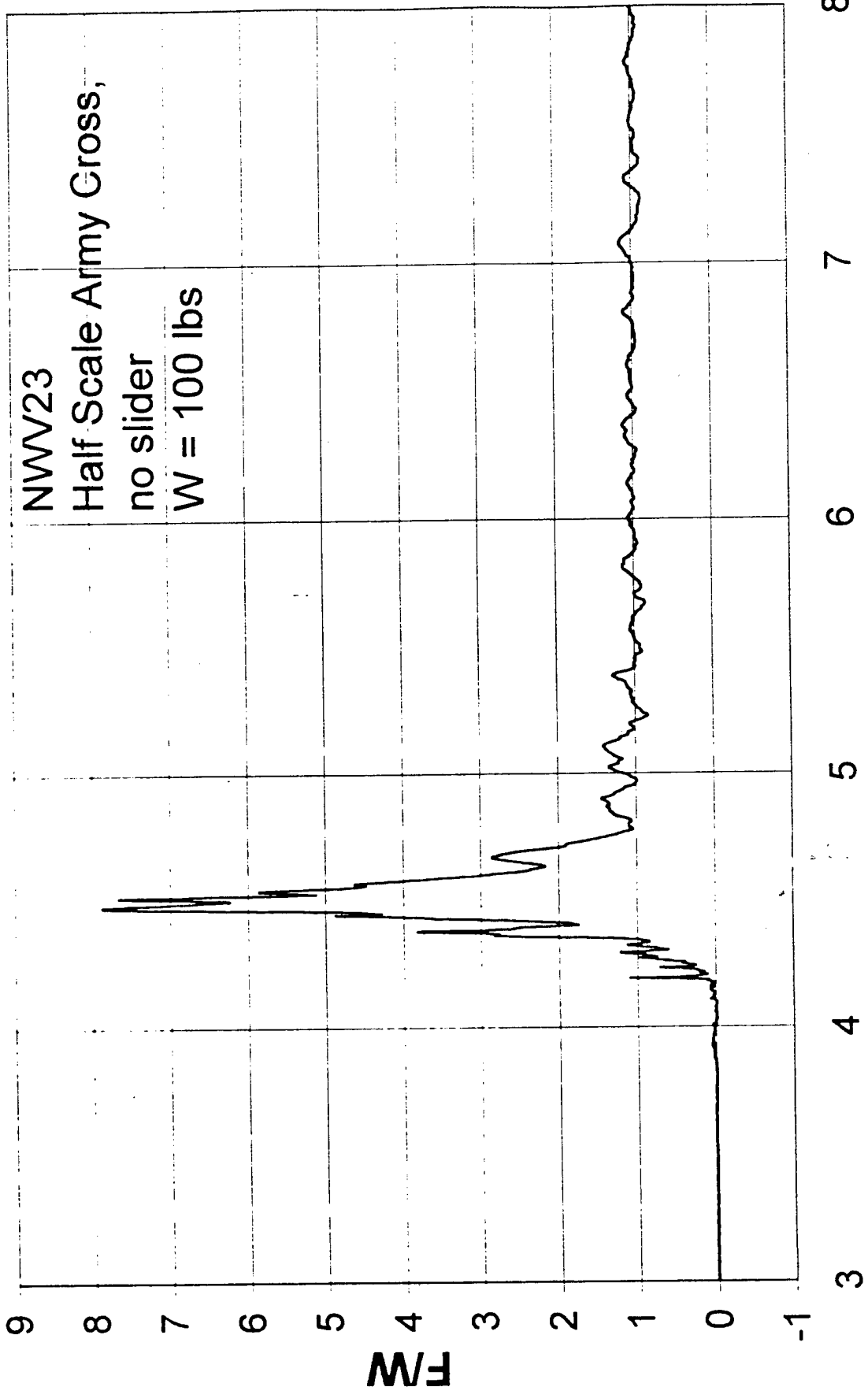




NWV21  
Half Scale Army Cross,  
no slider  
W = 100 lbs

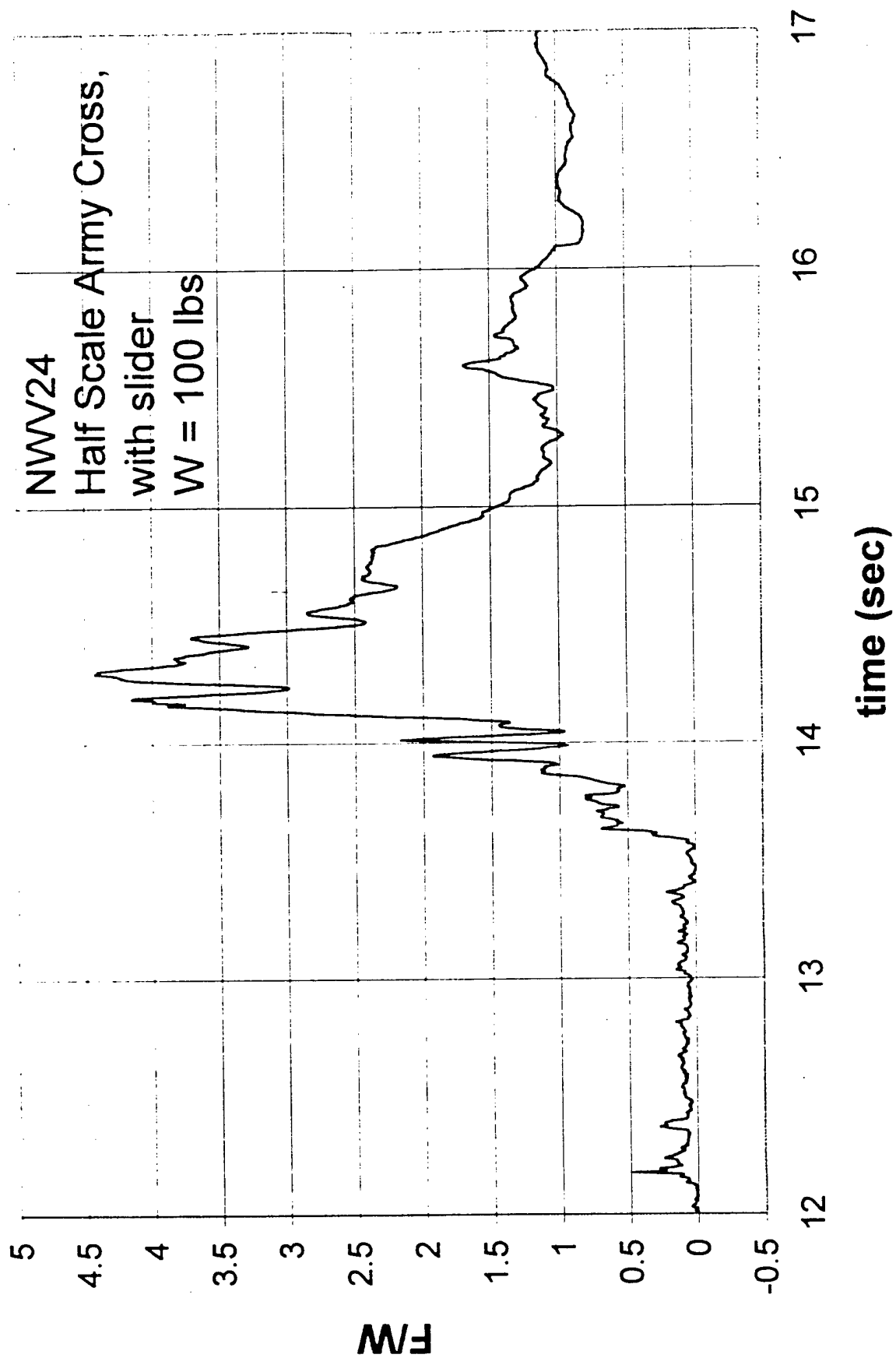
time (sec)

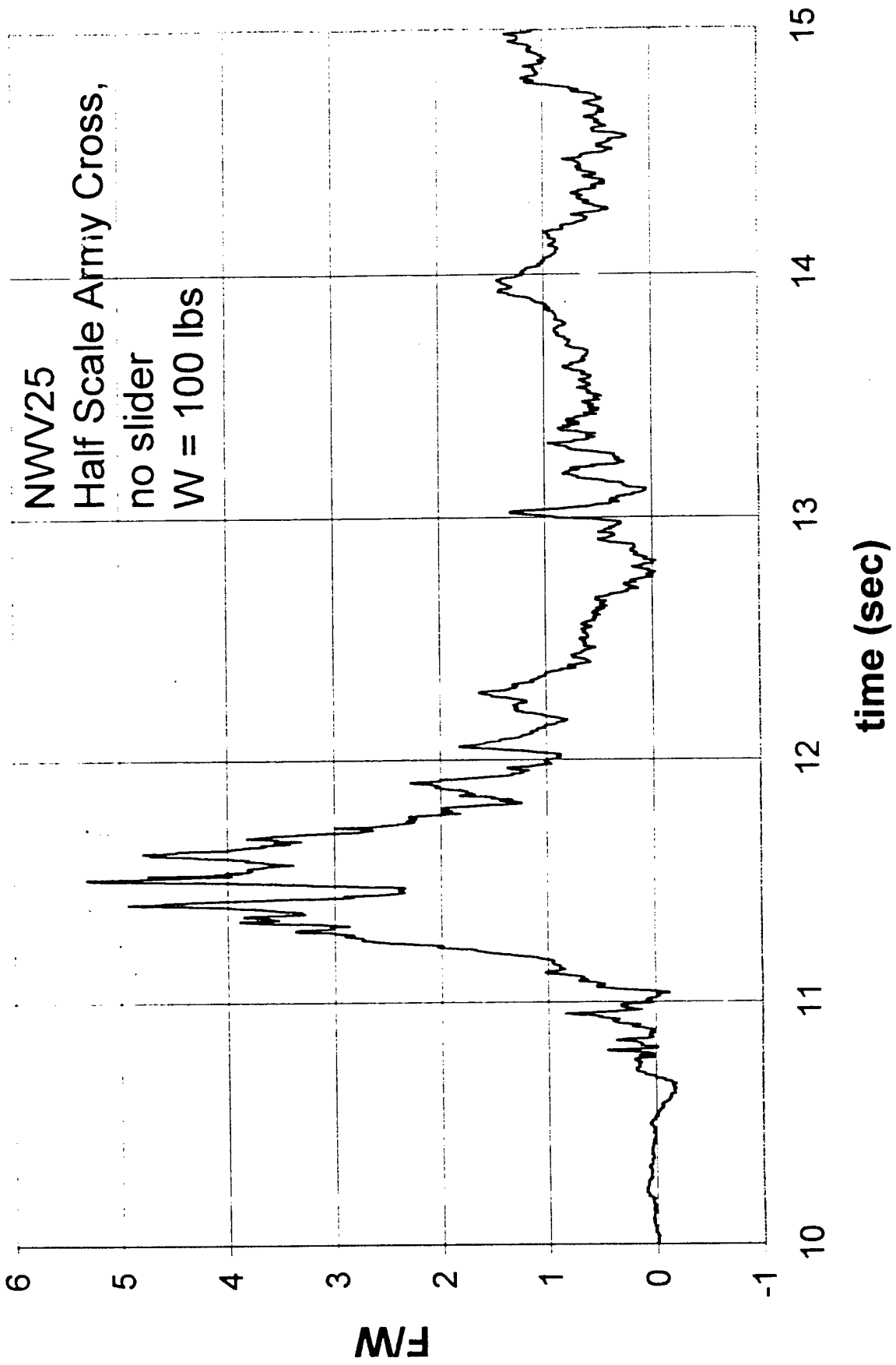


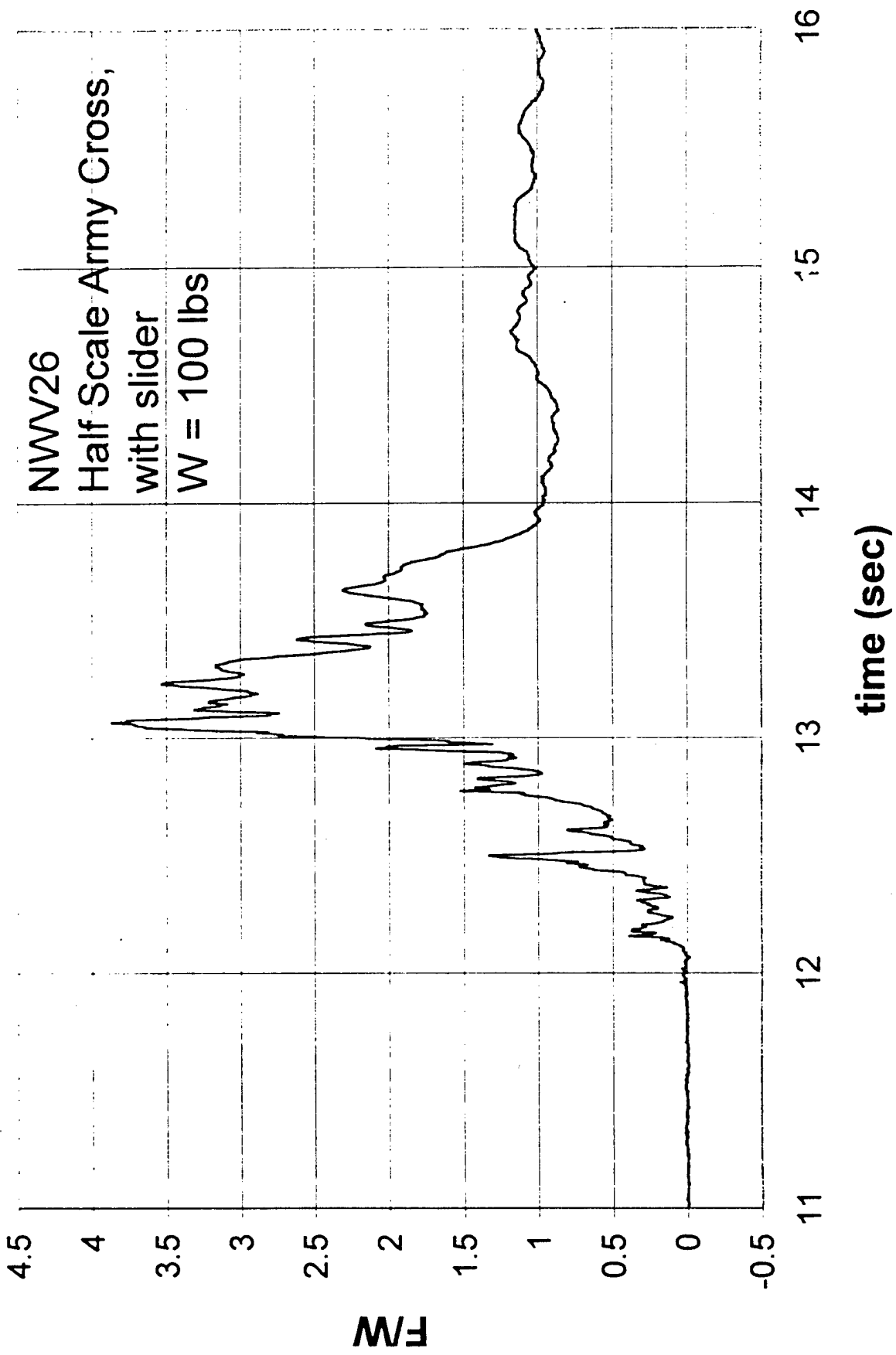


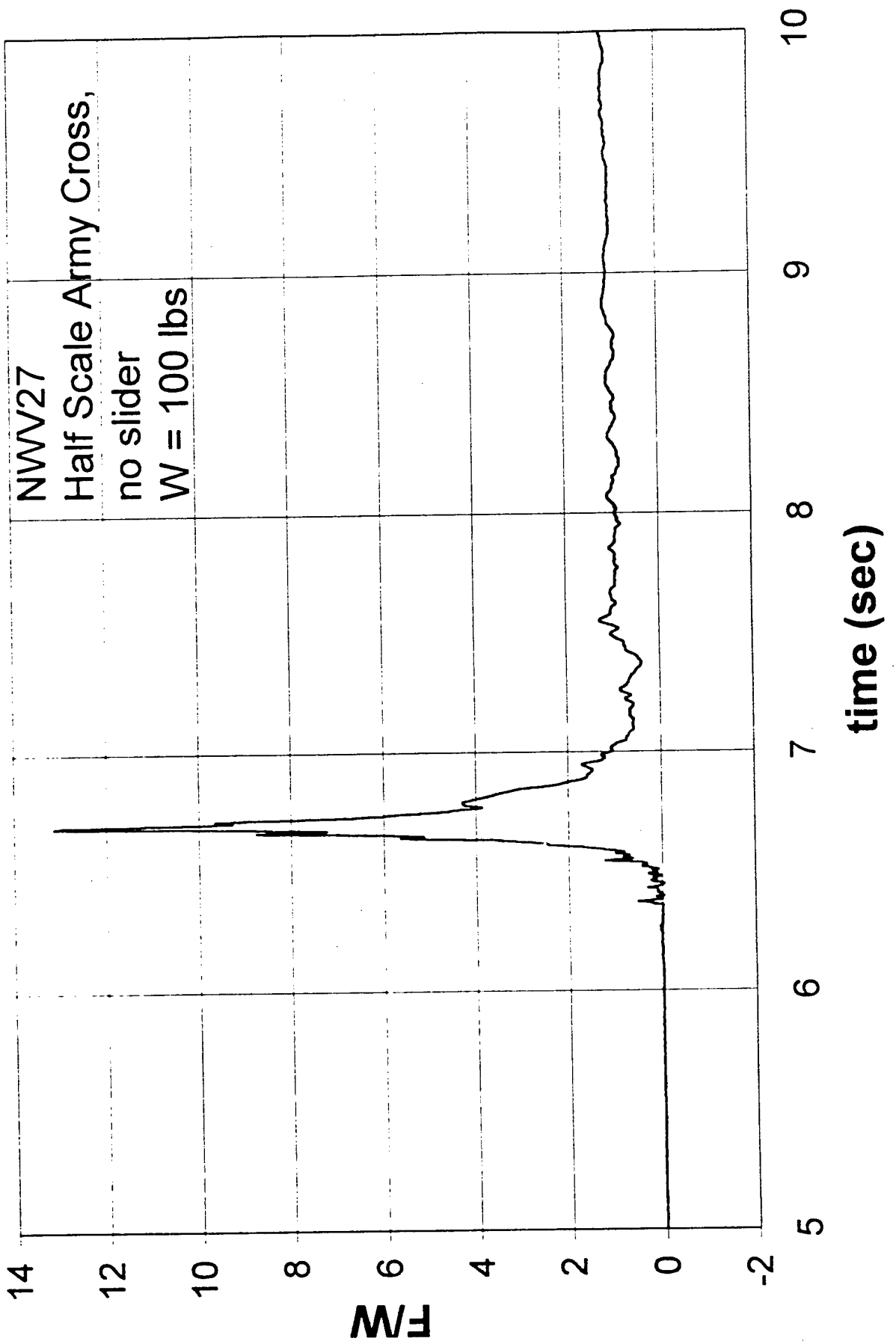
NWV23  
Half Scale Army Cross,  
no slider  
W = 100 lbs

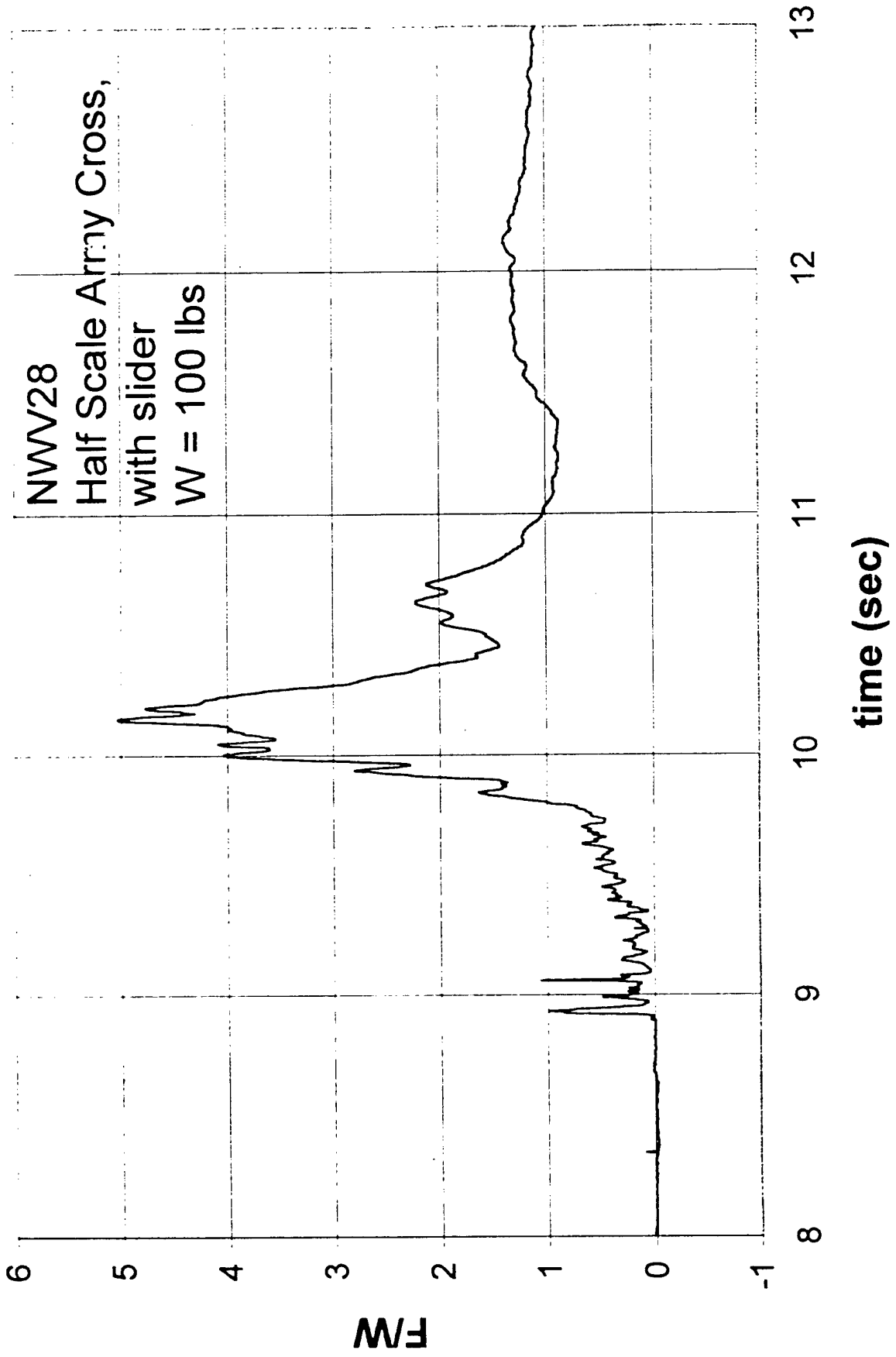
time (sec)

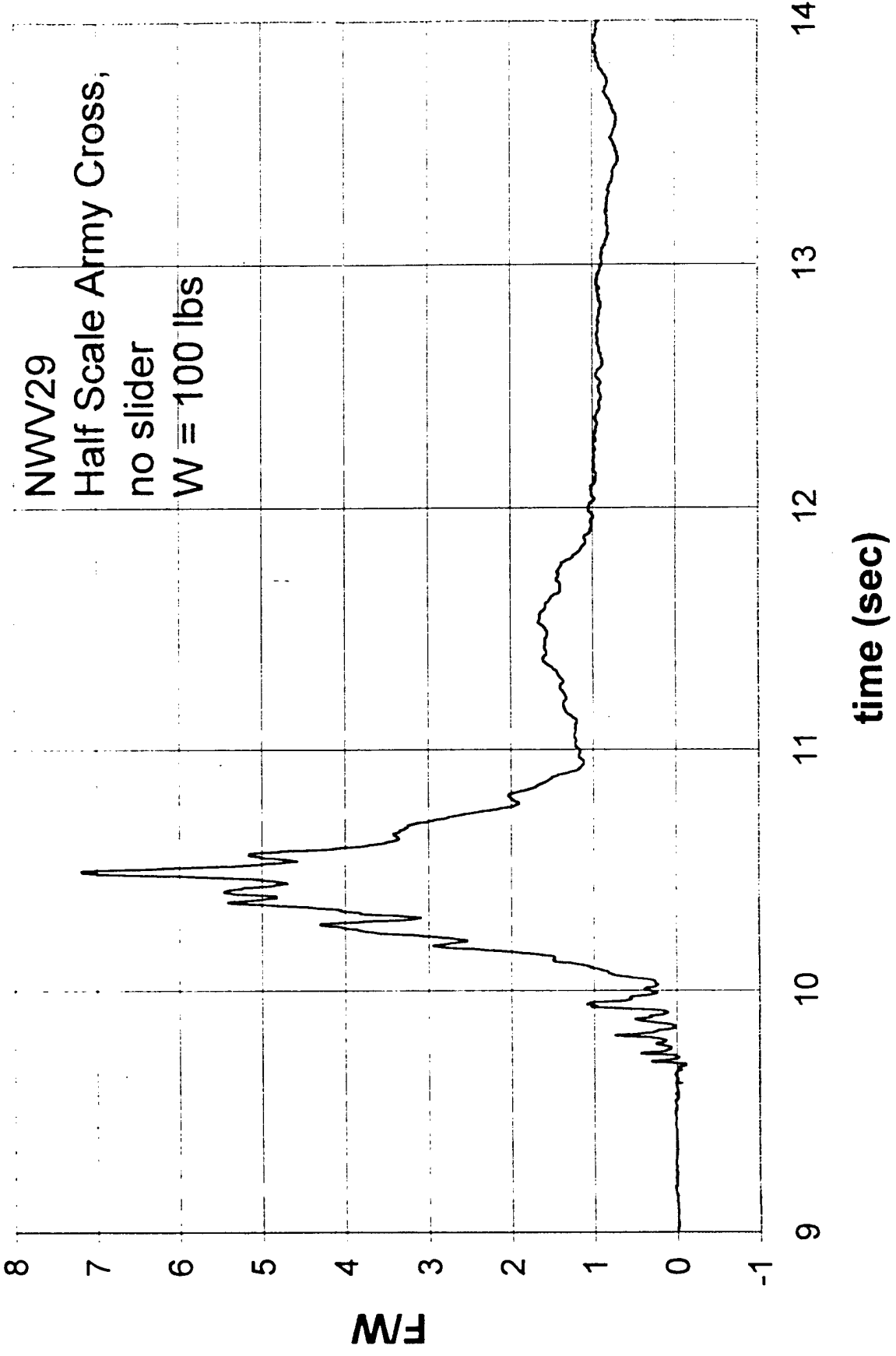


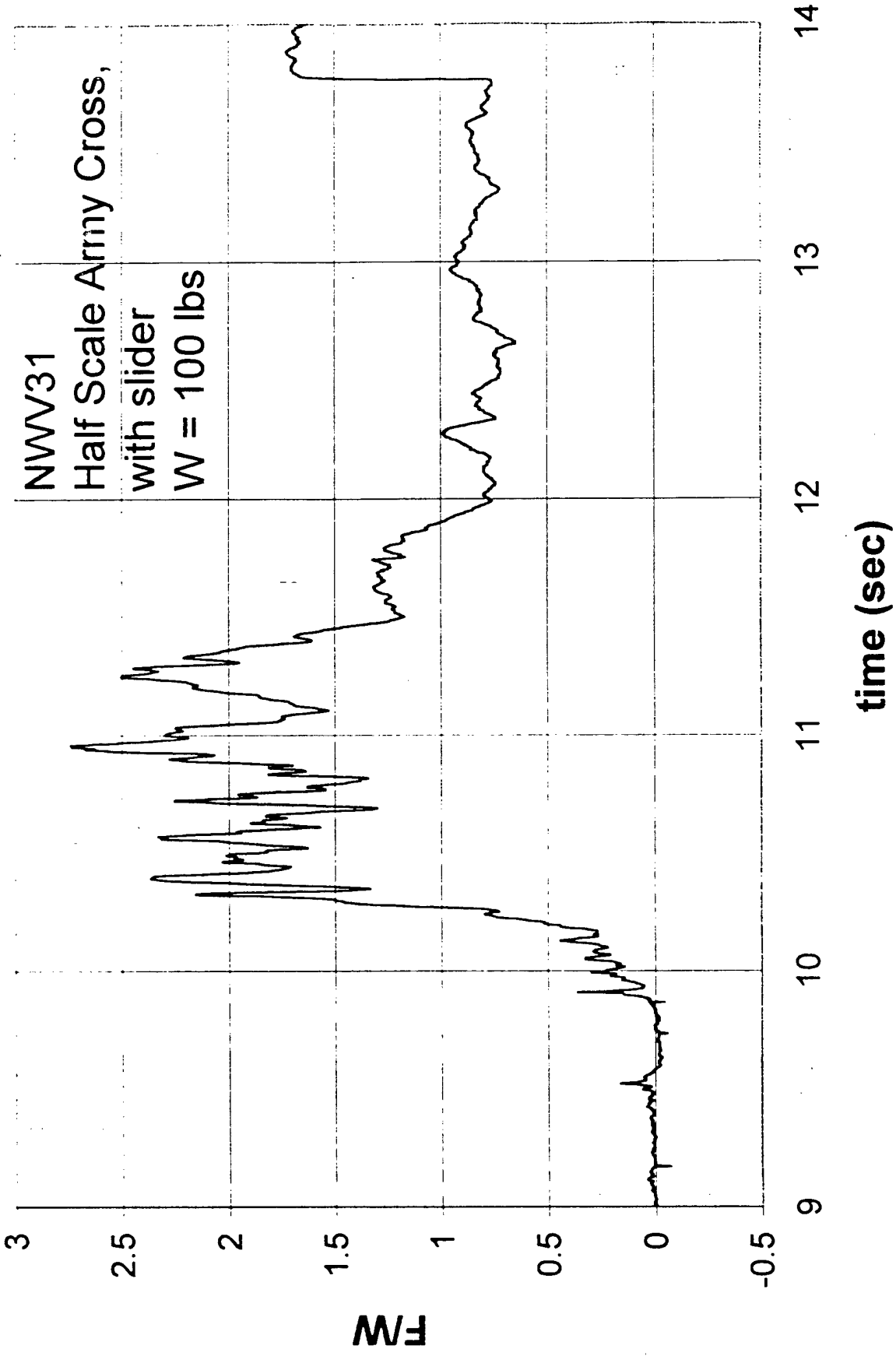


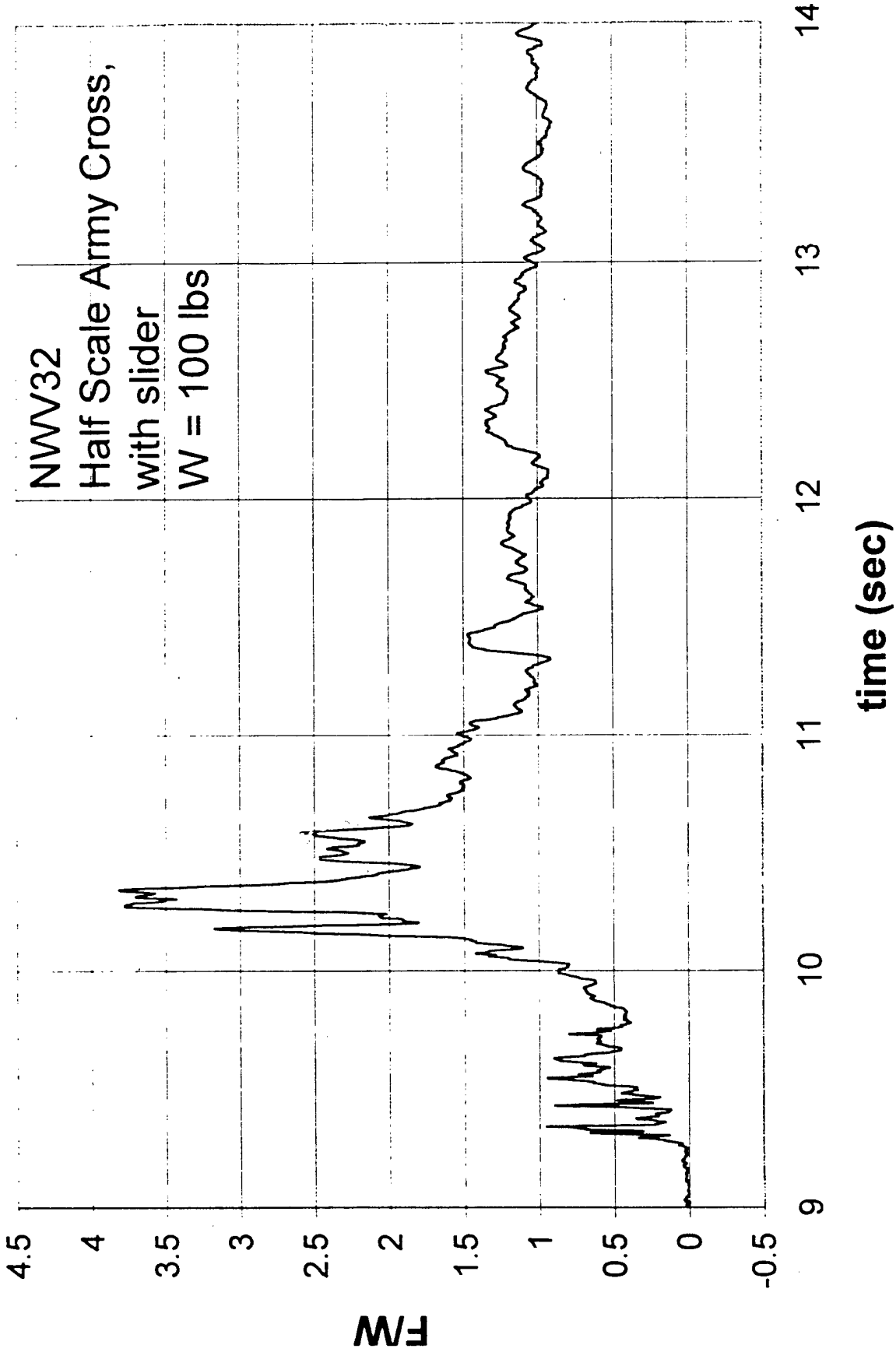


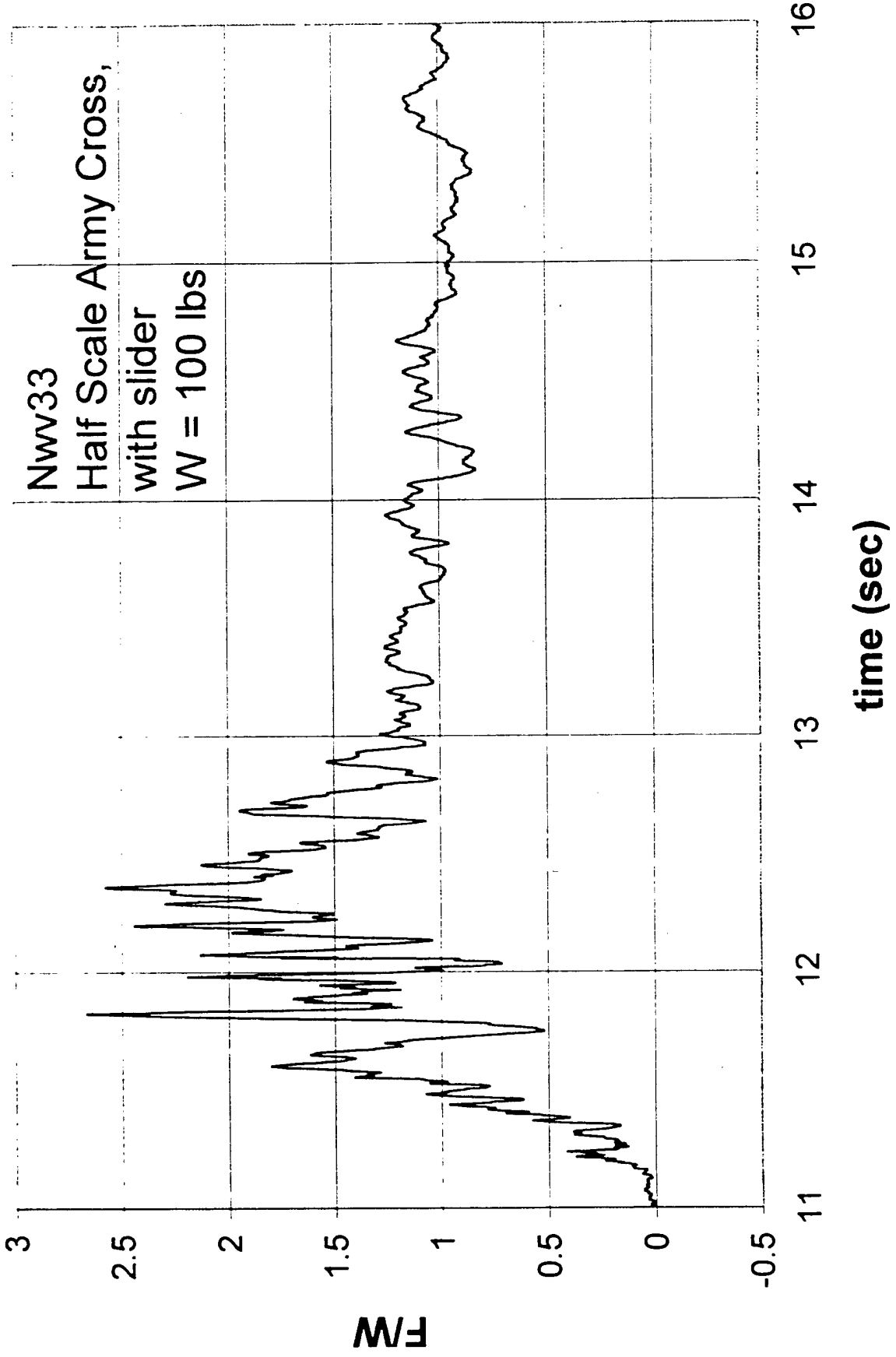


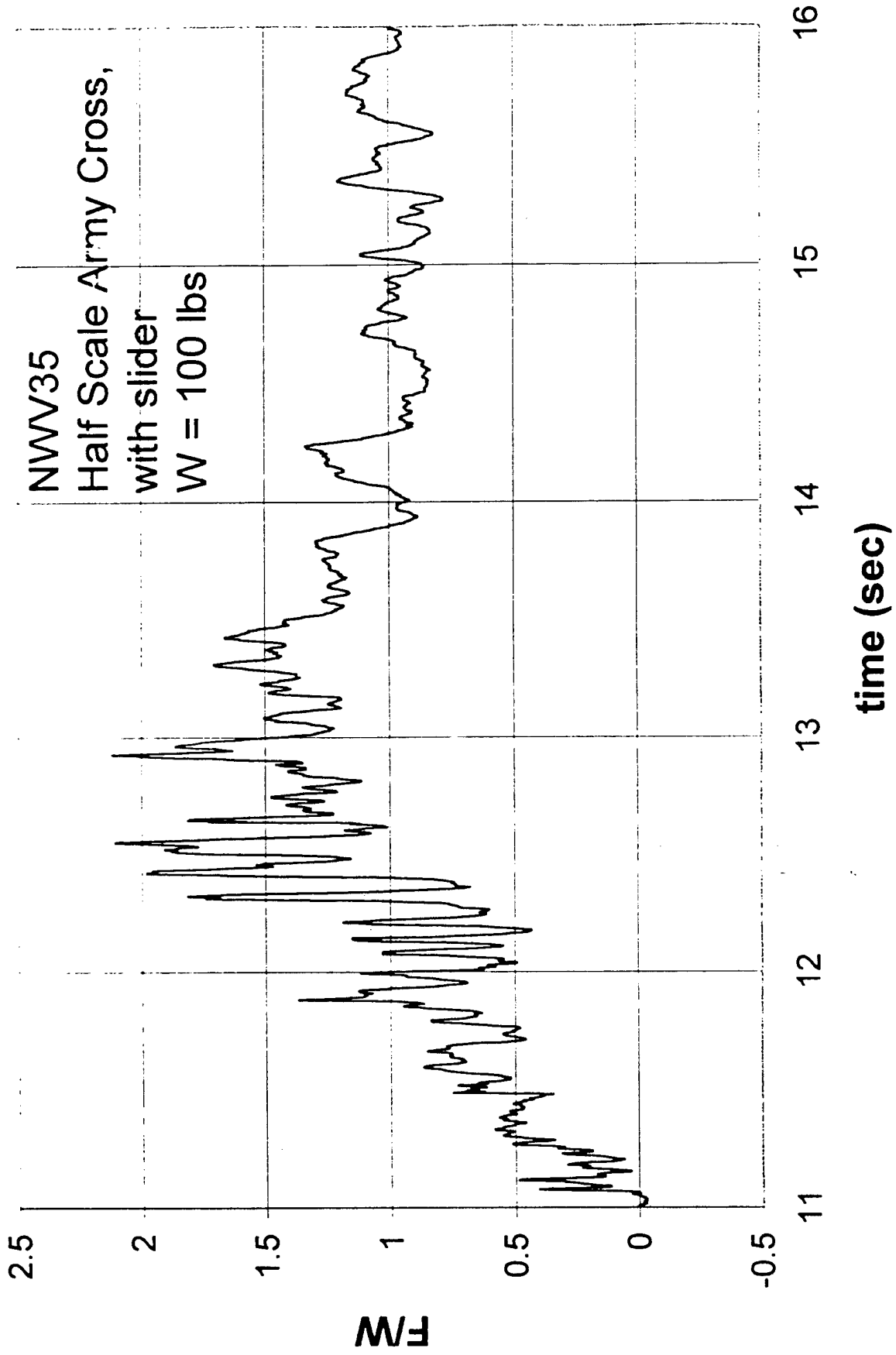


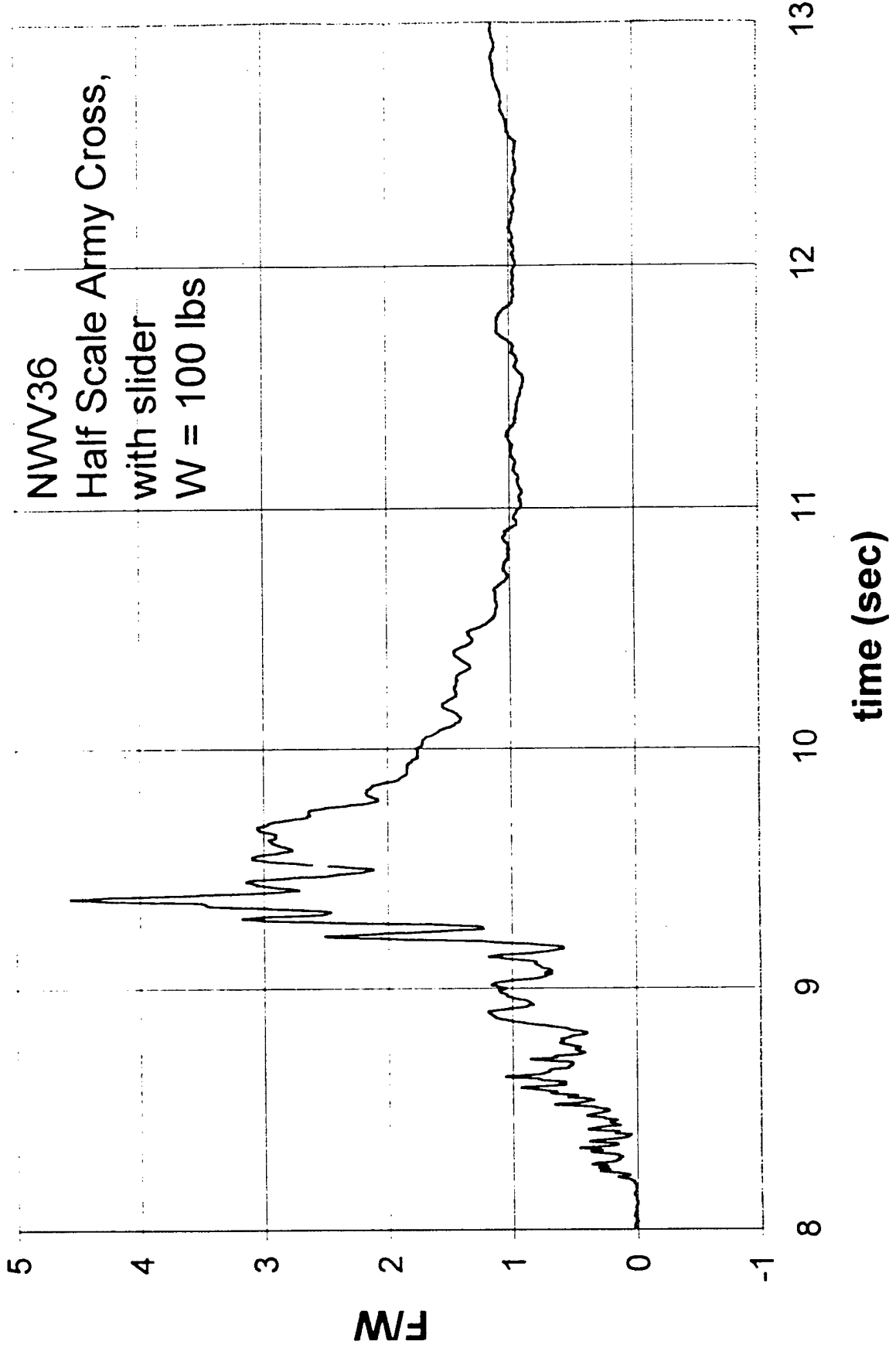


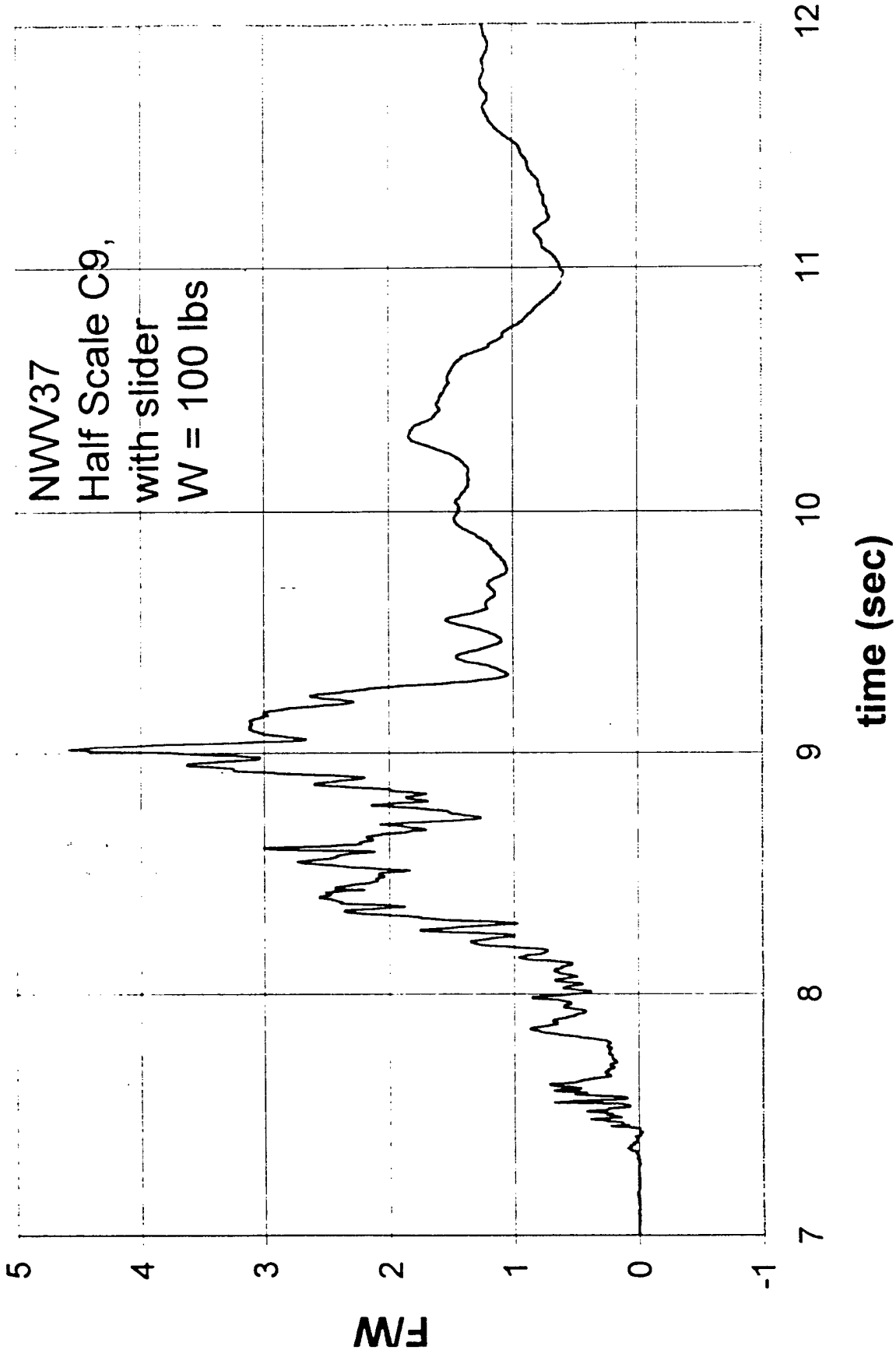


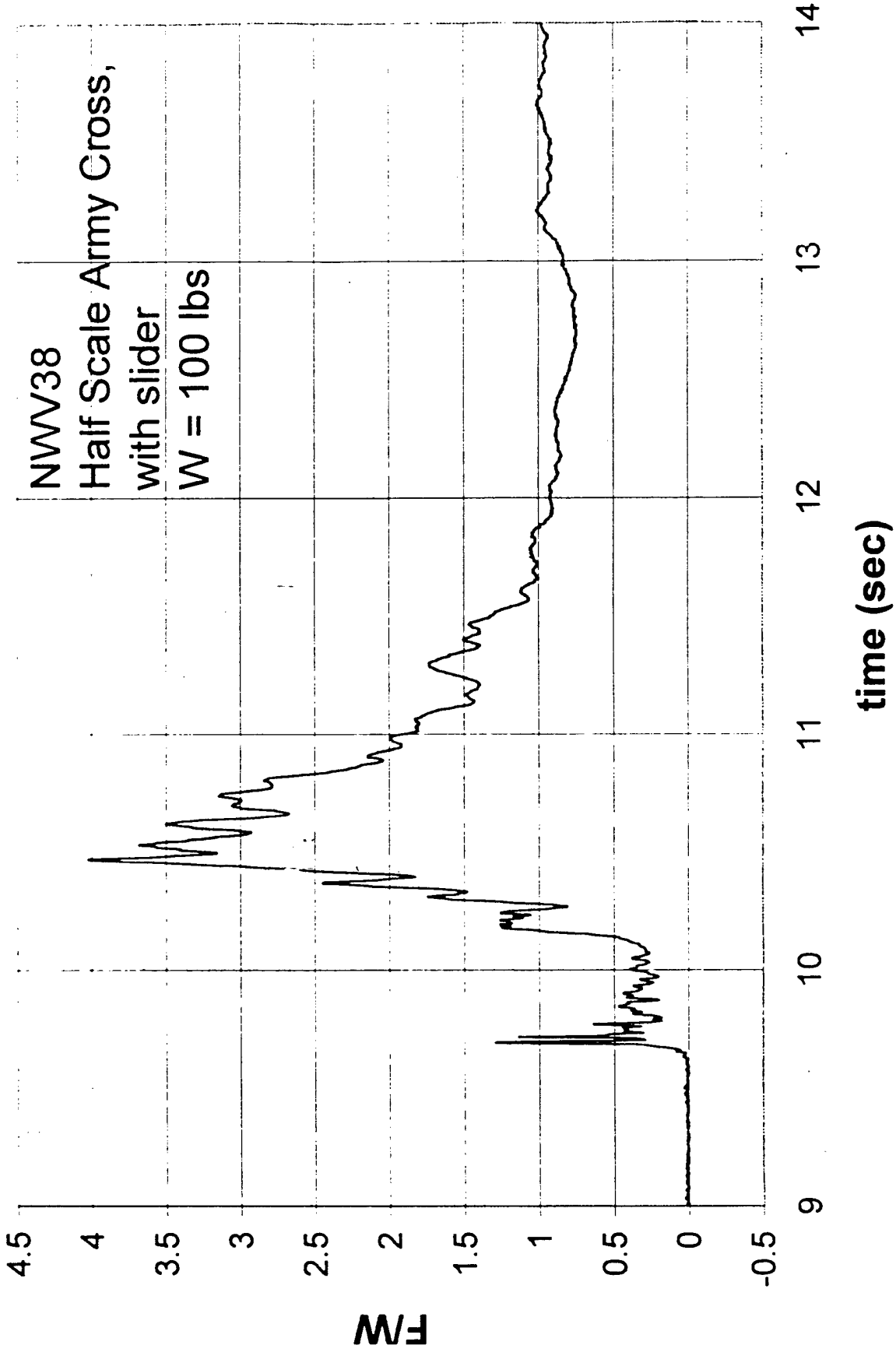


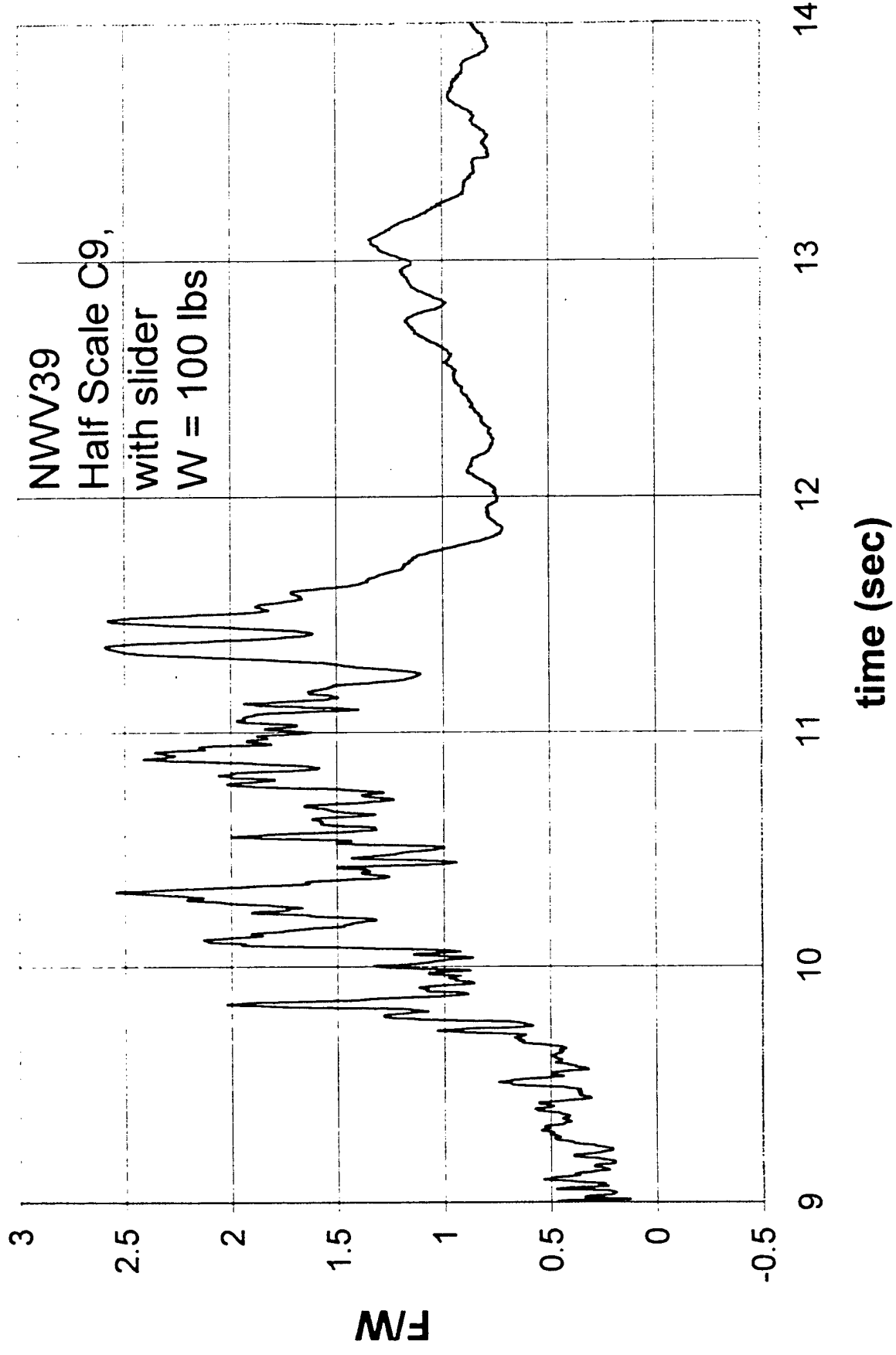


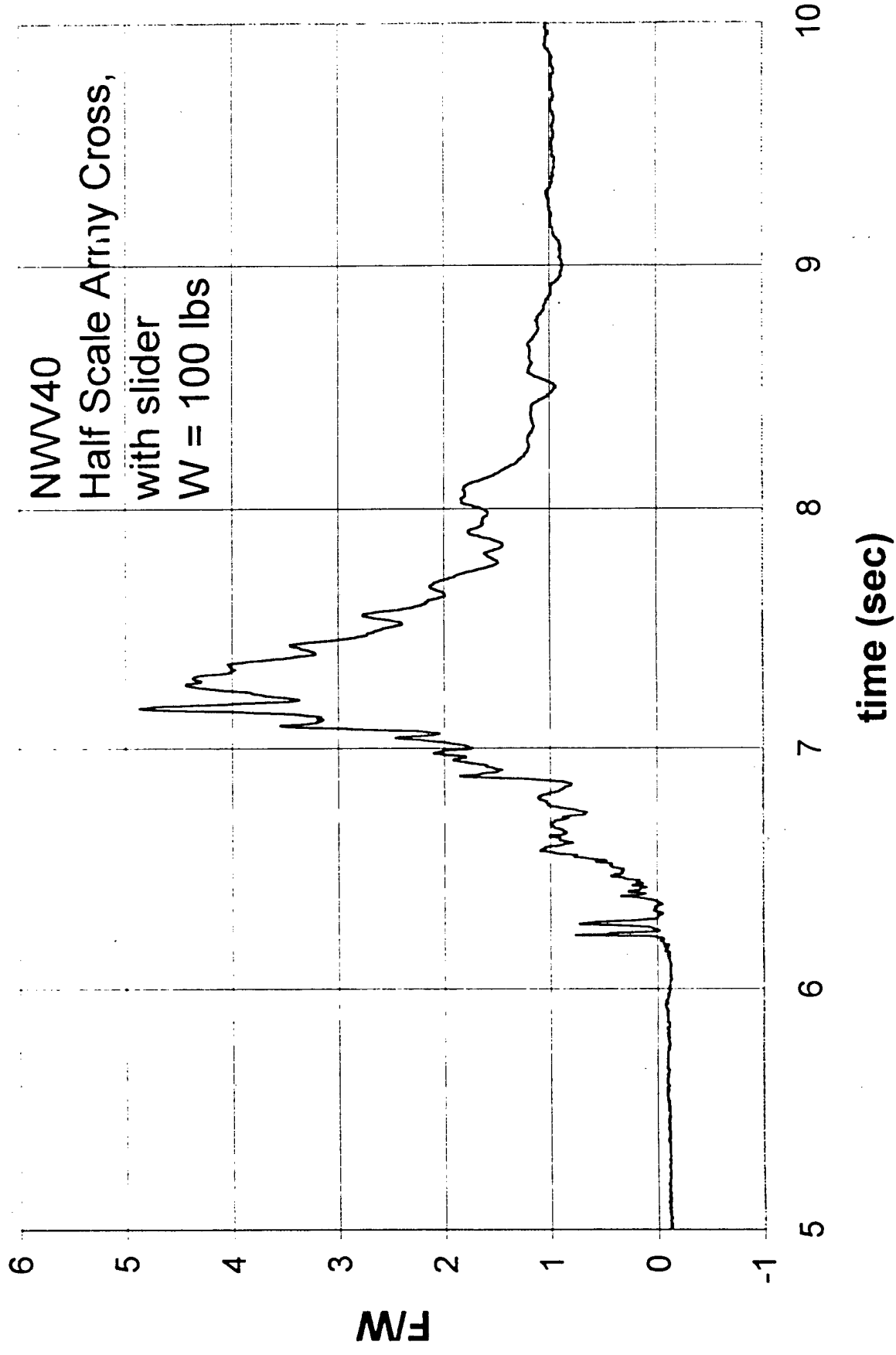


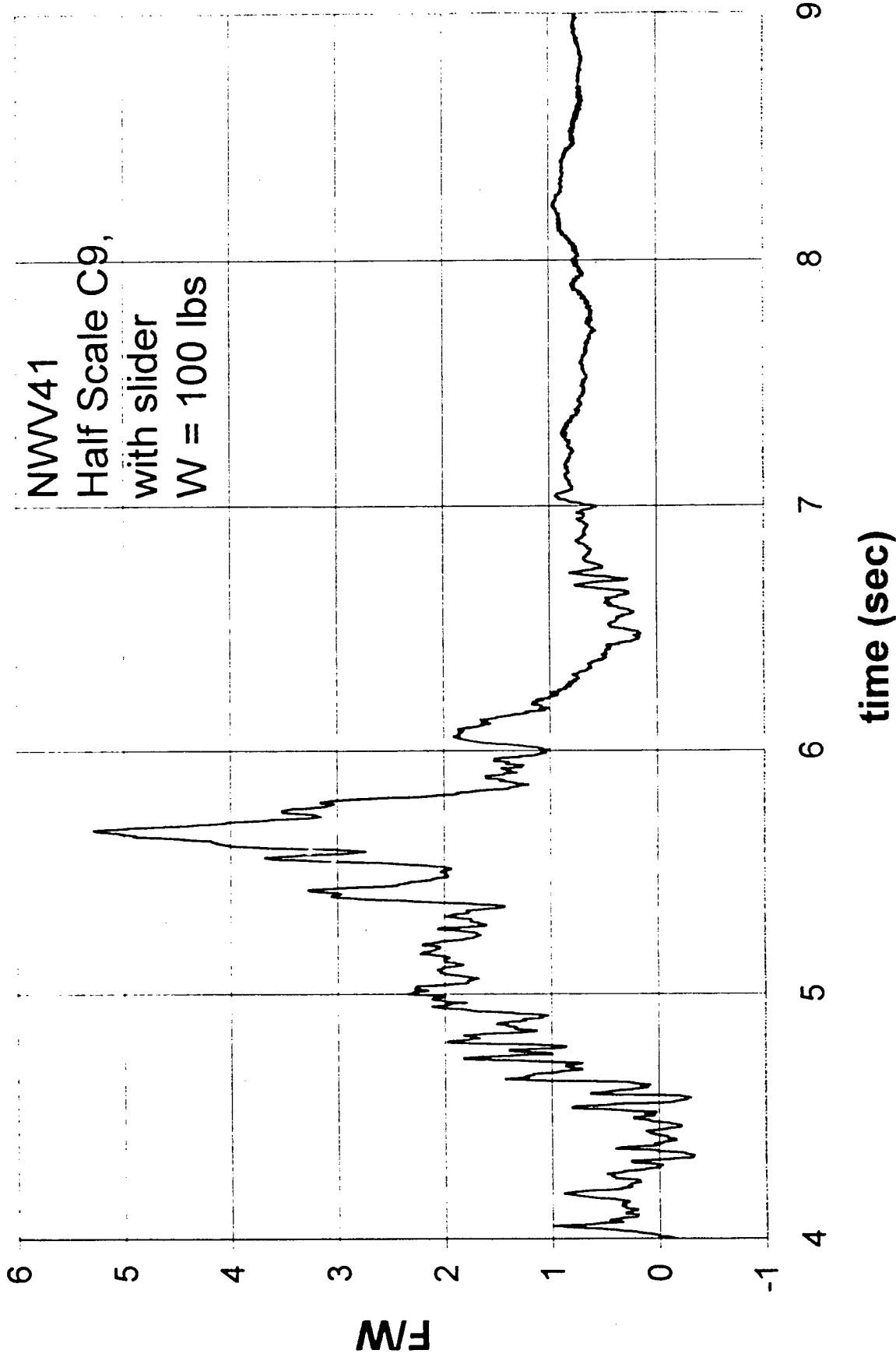


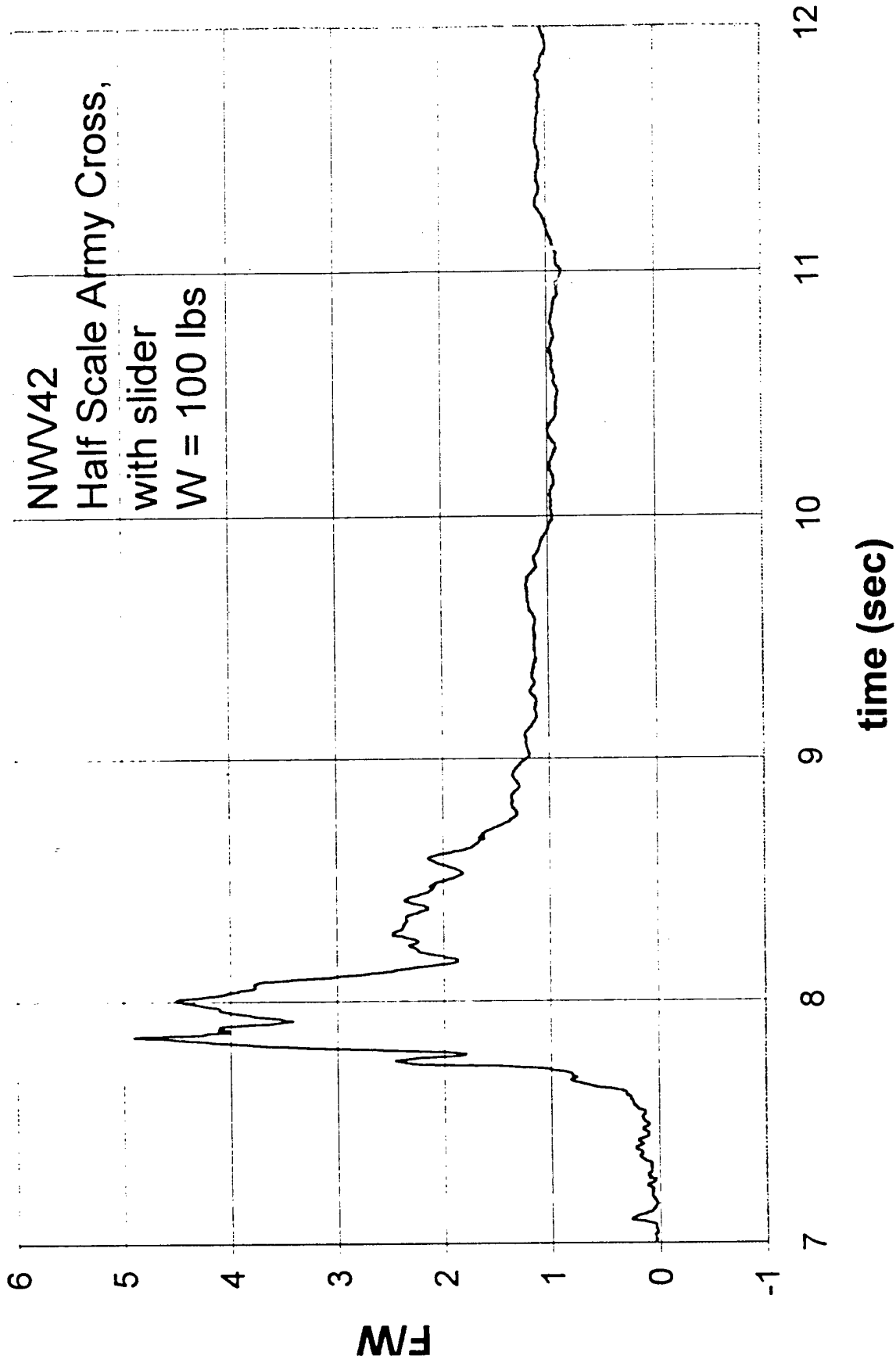


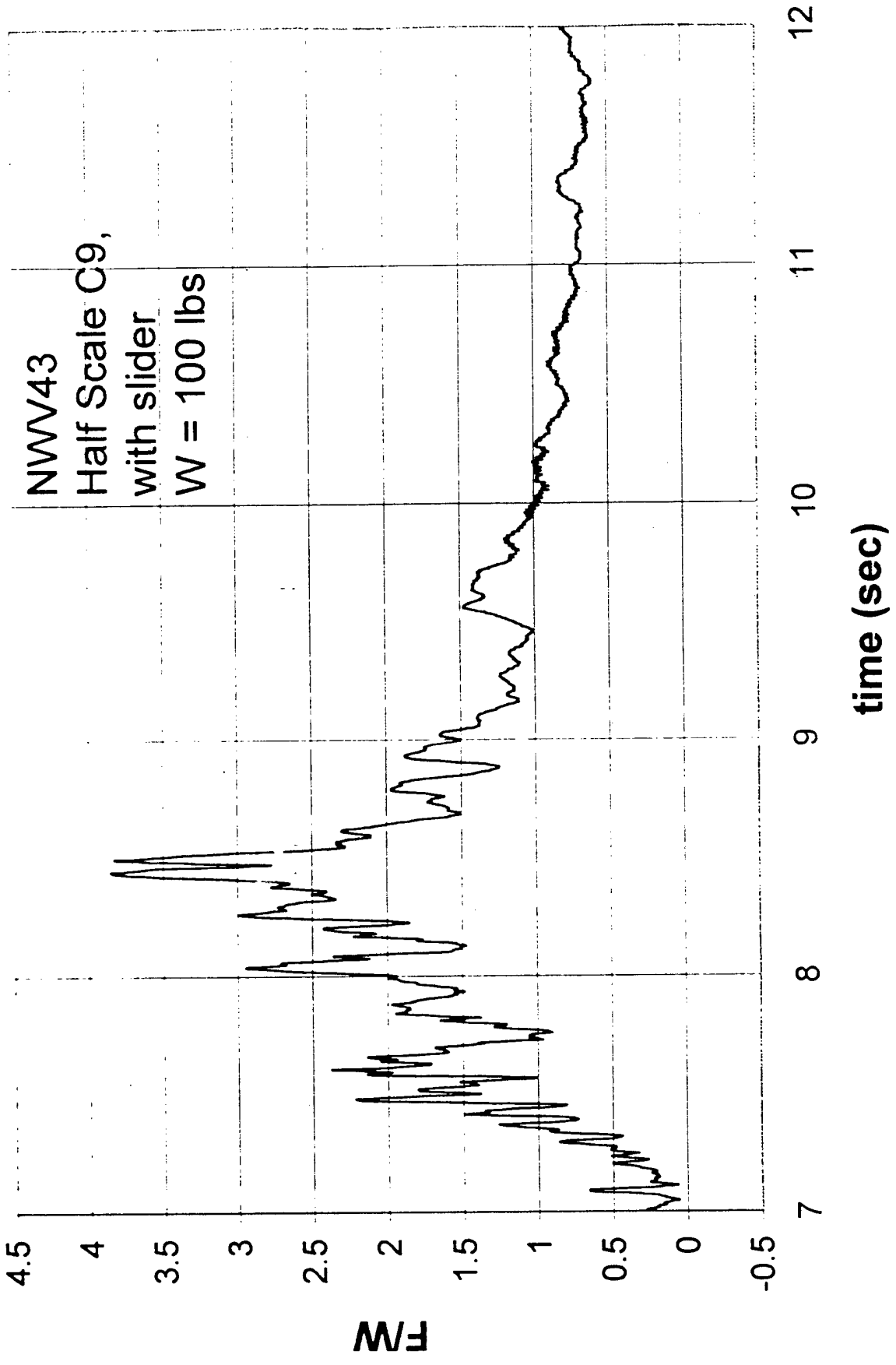


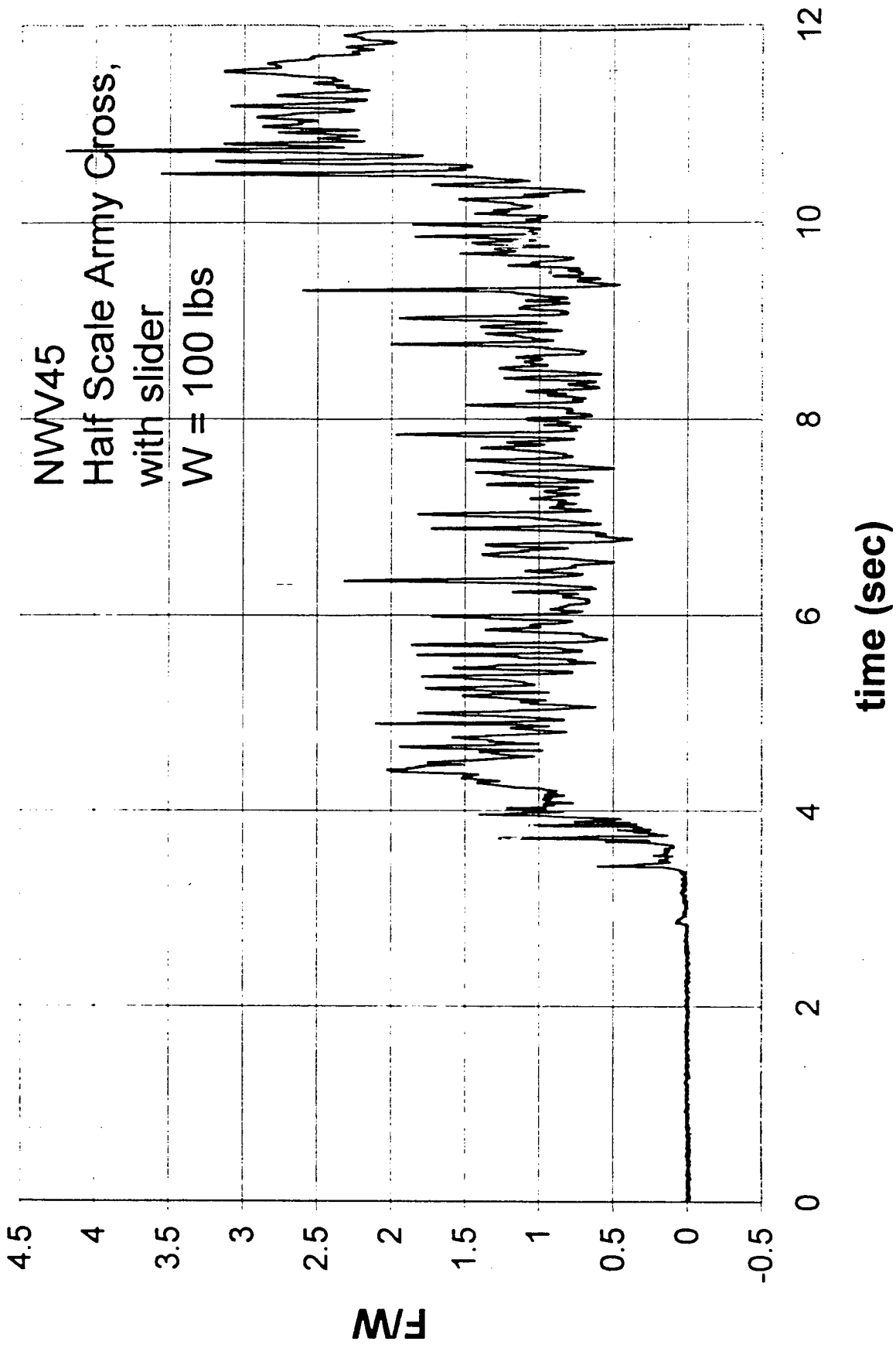


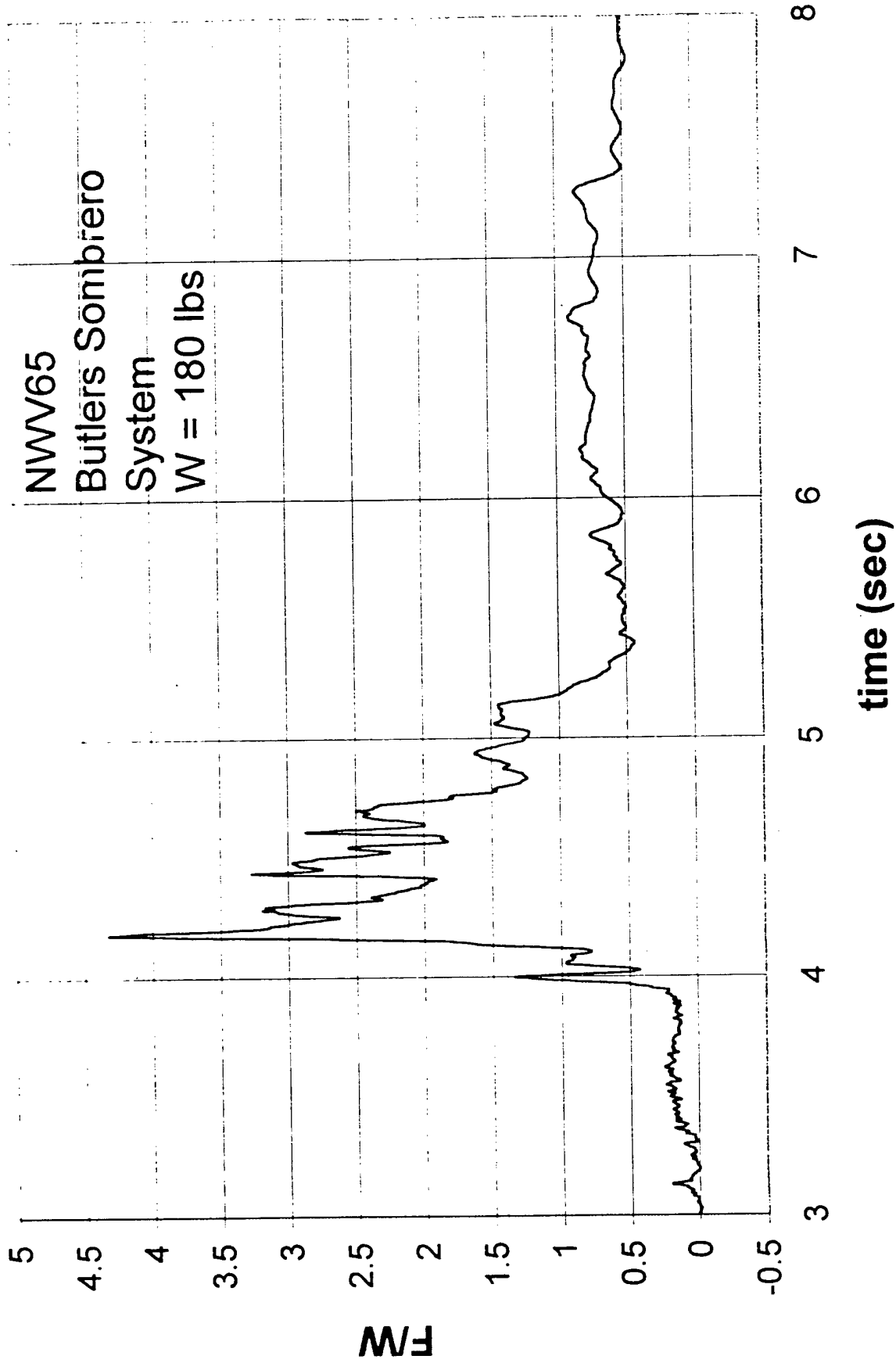


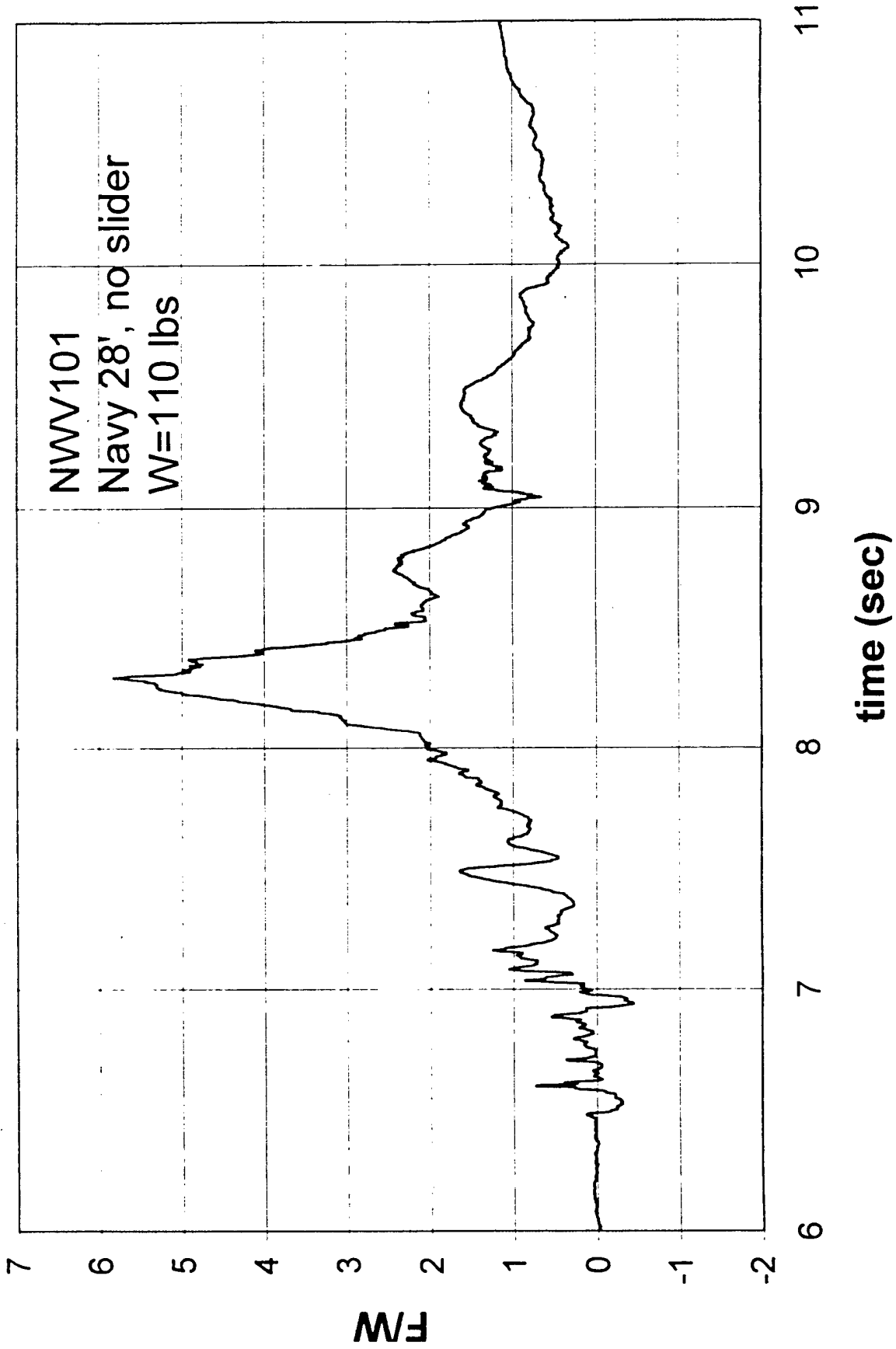


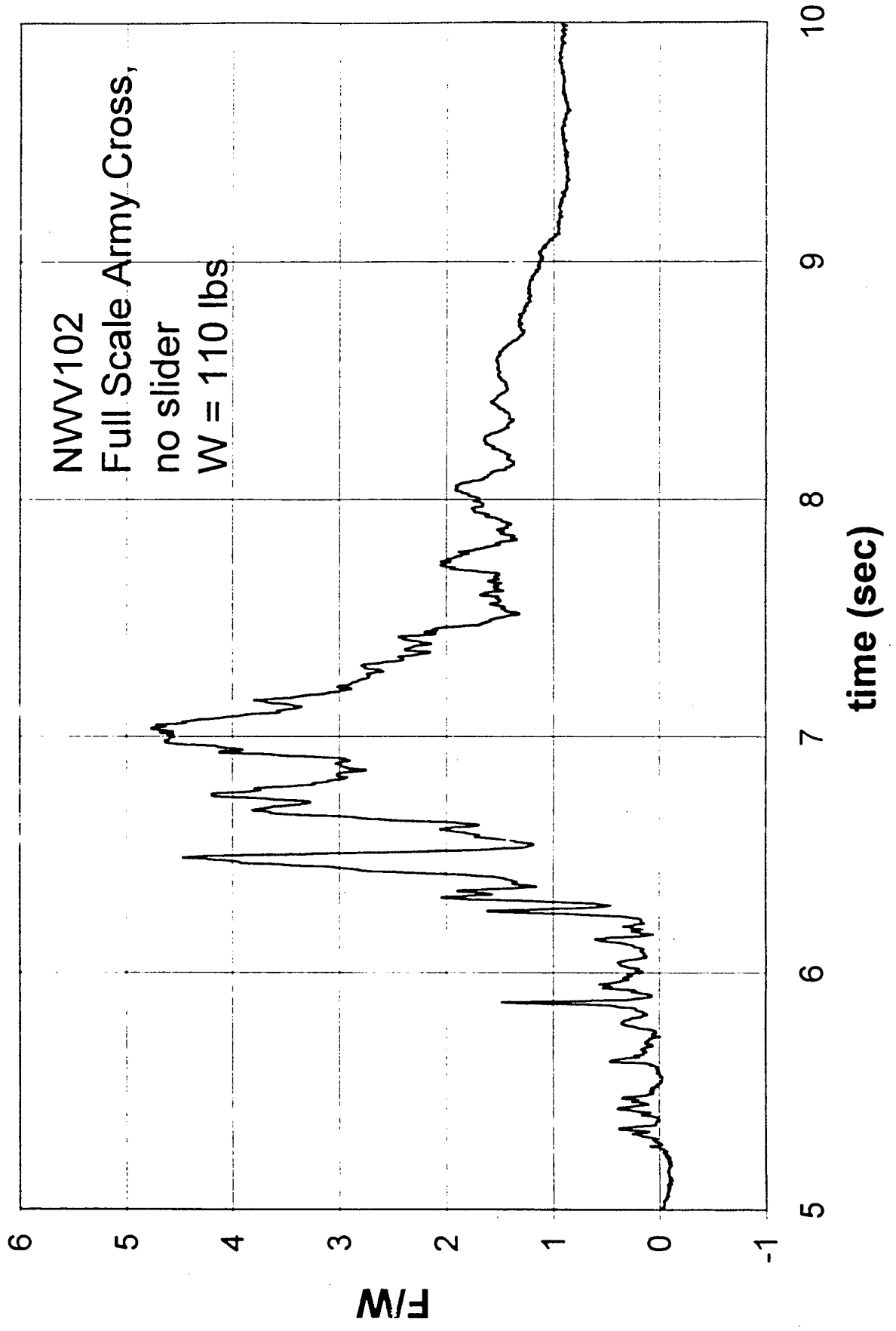


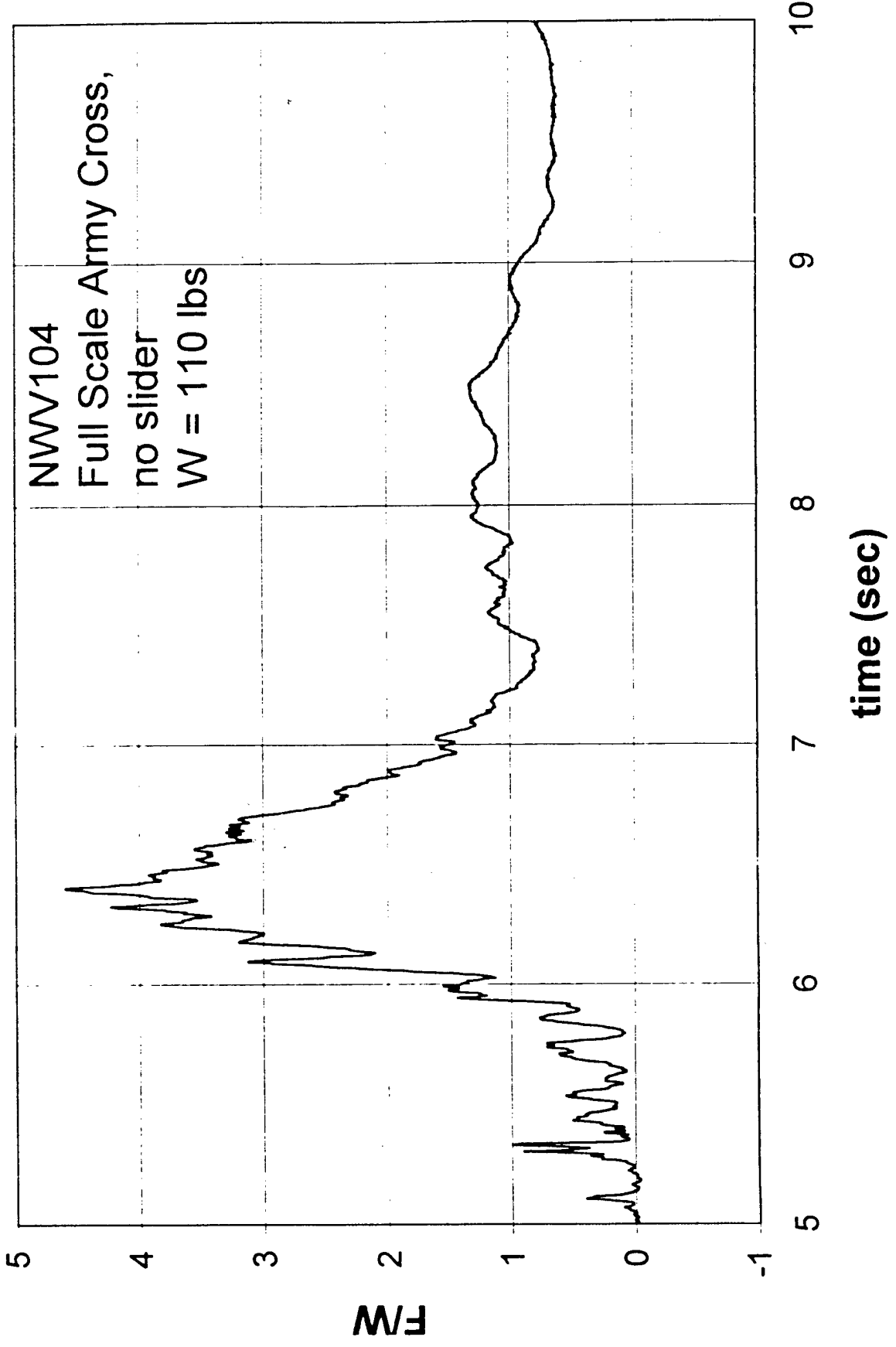


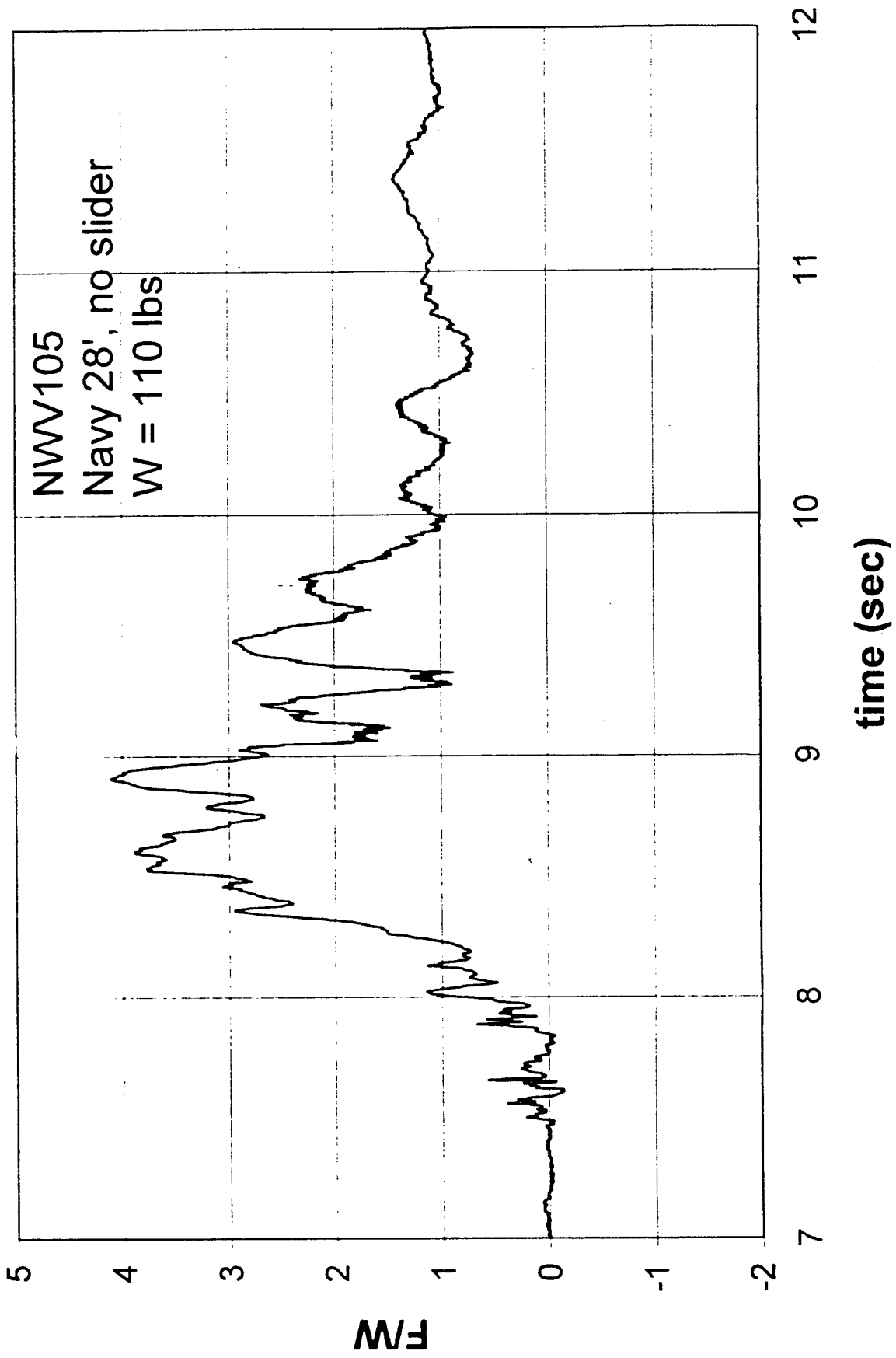


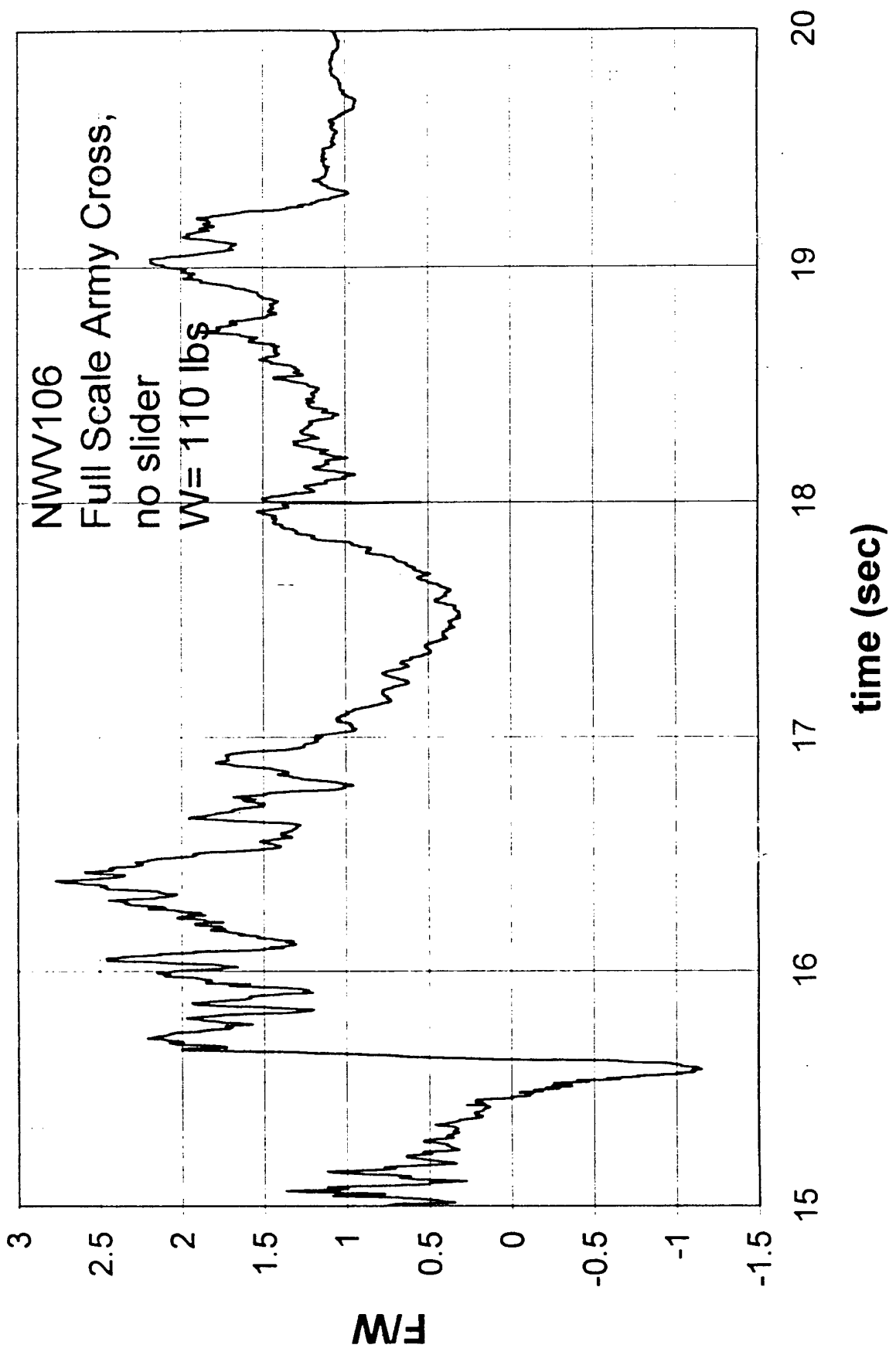


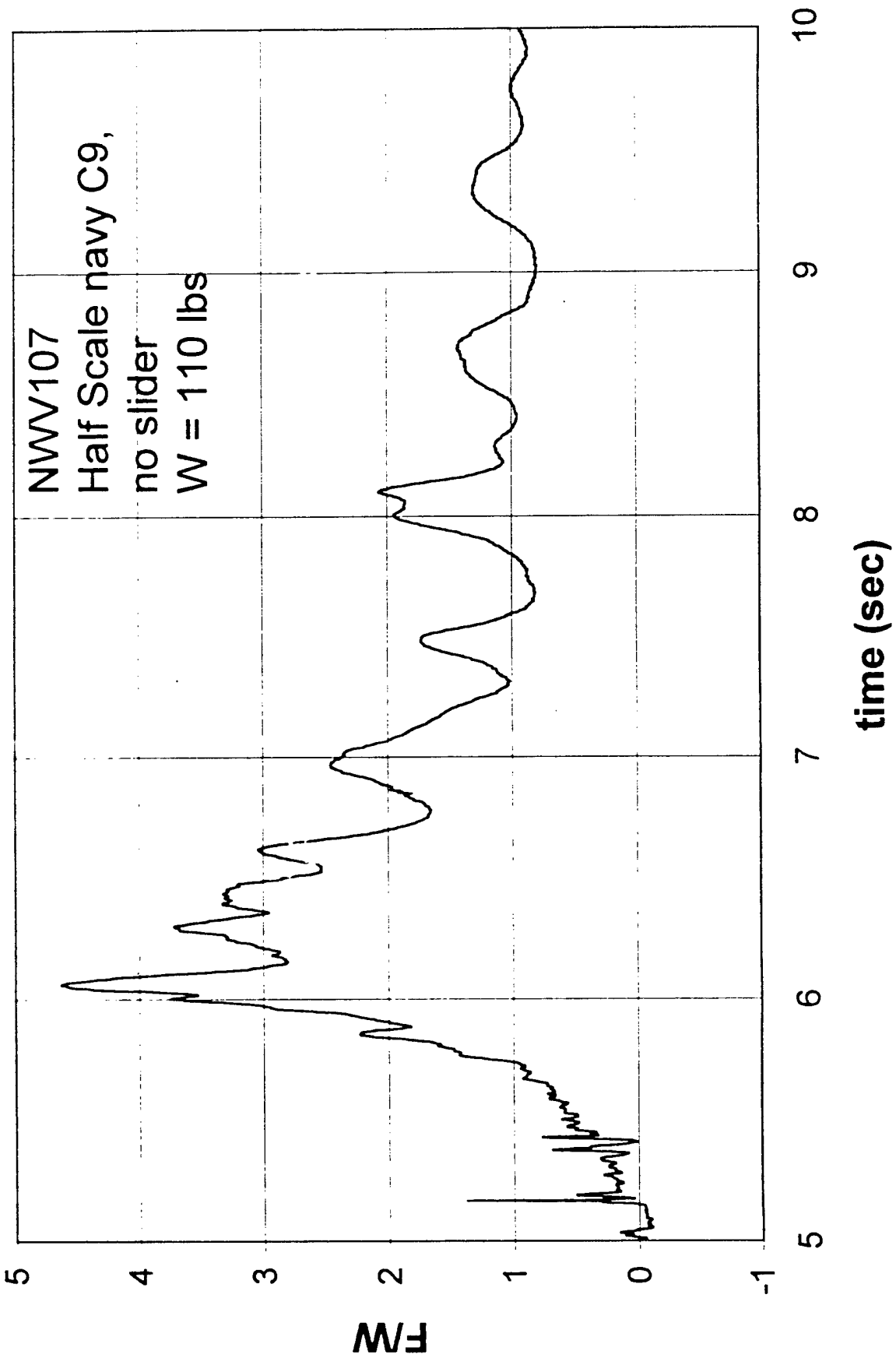


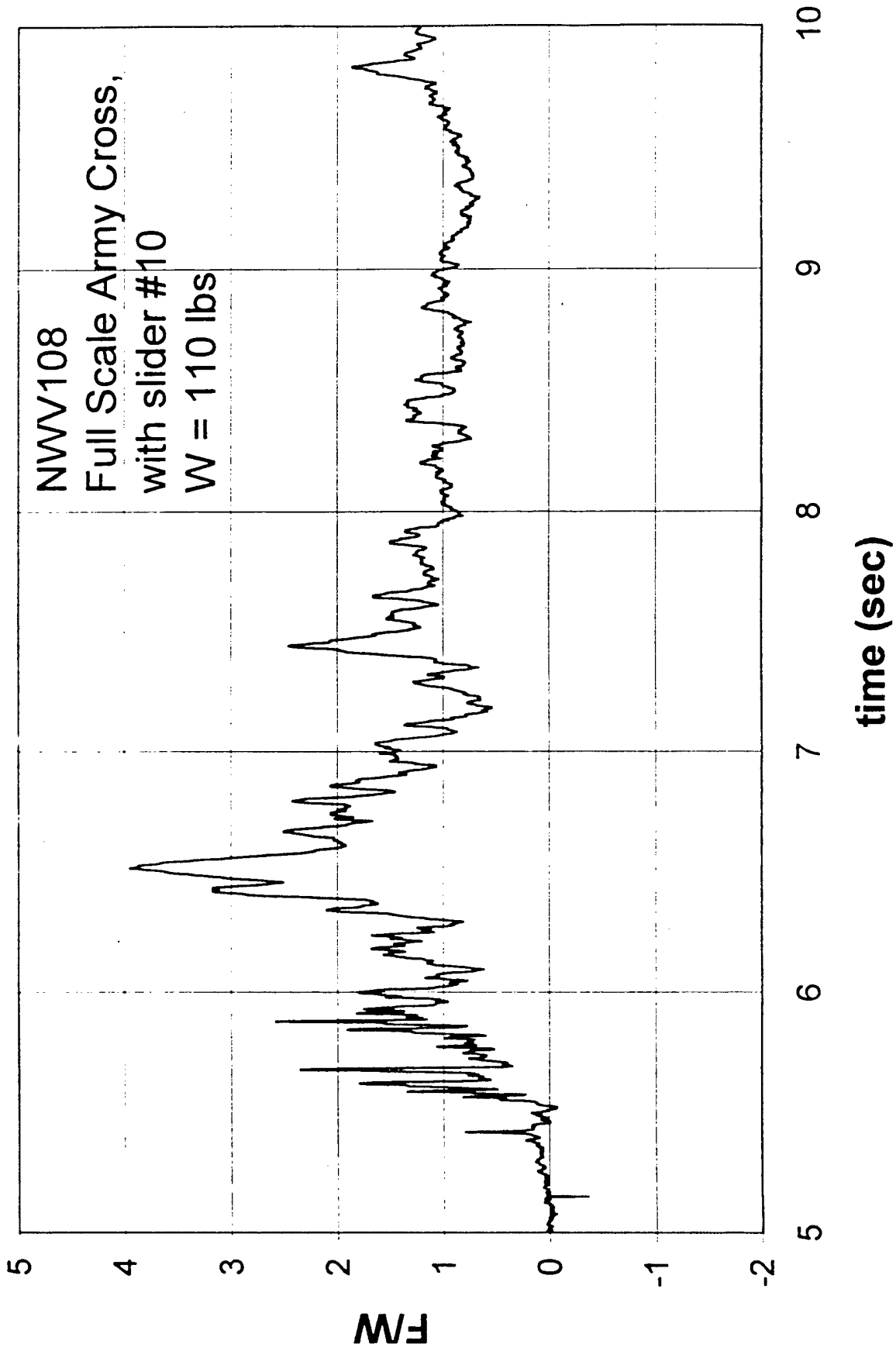


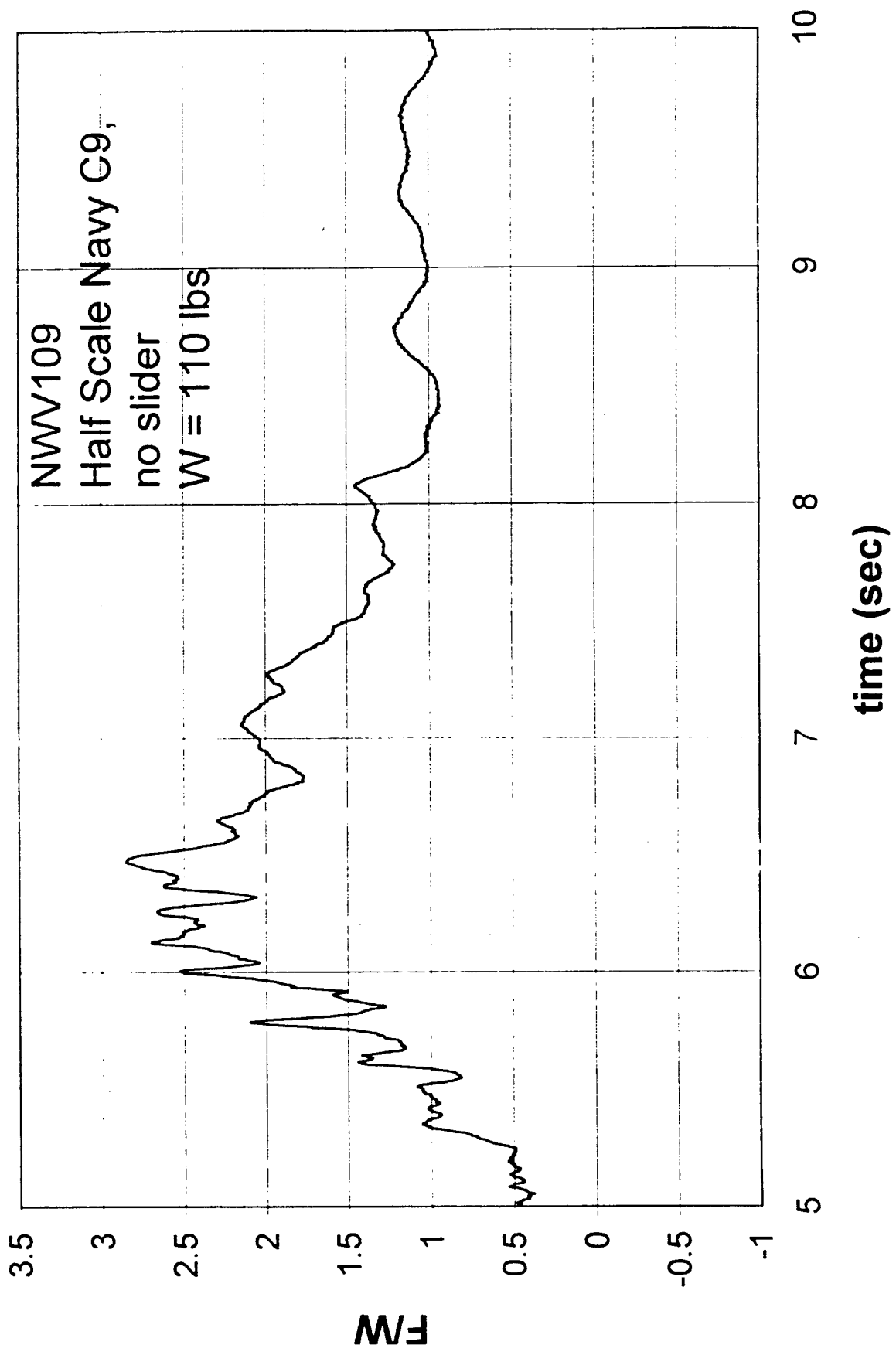


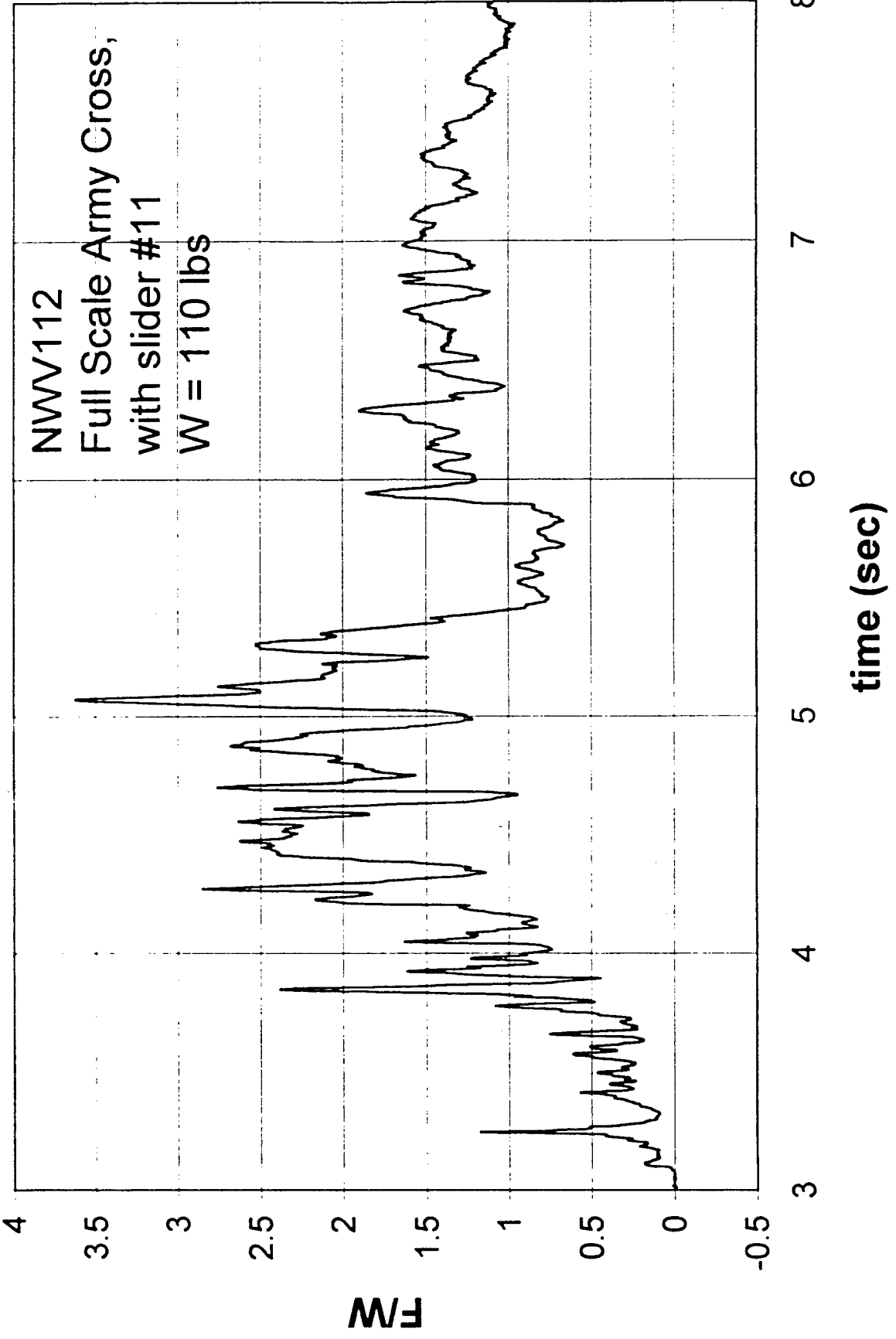


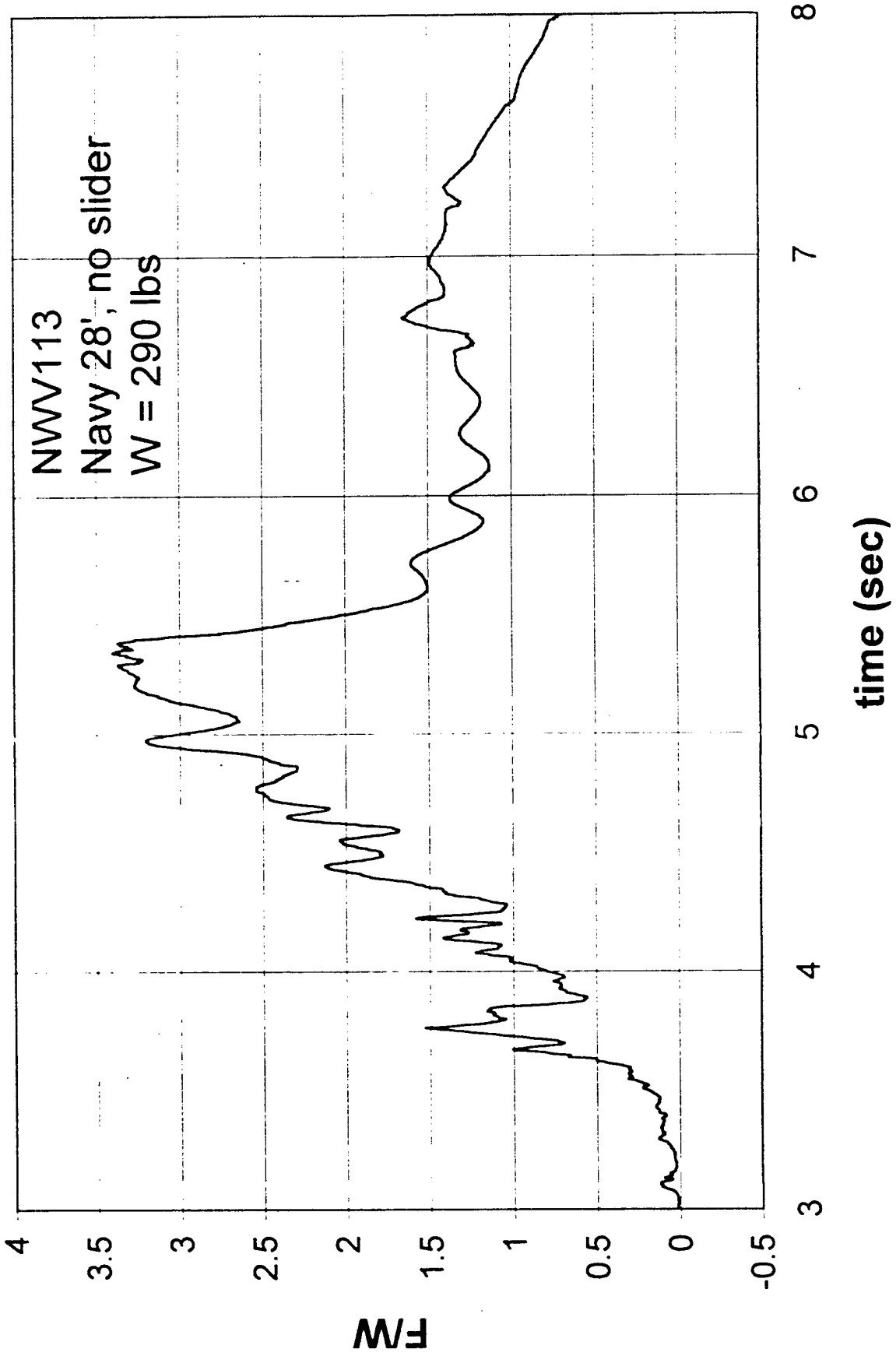


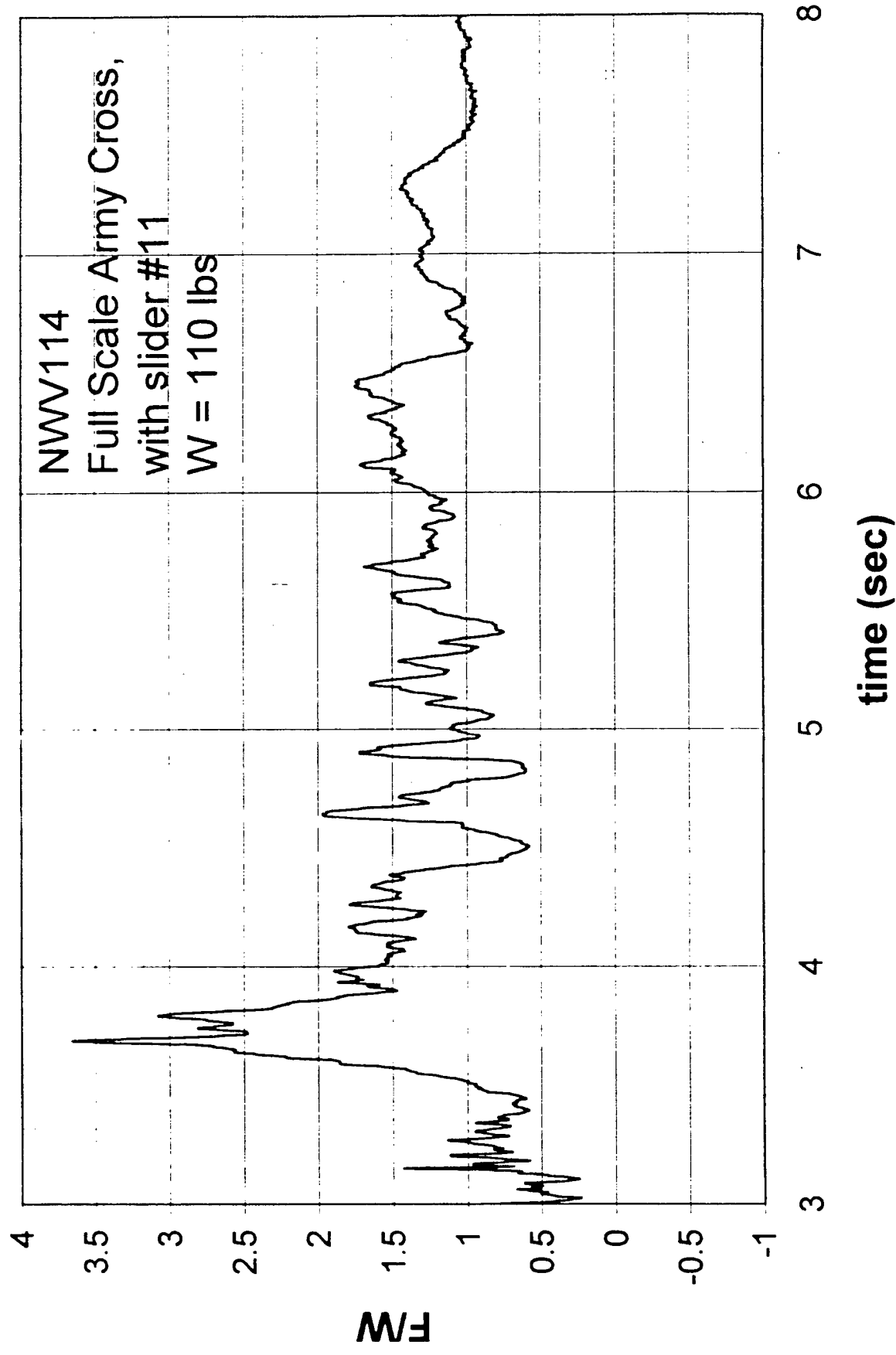


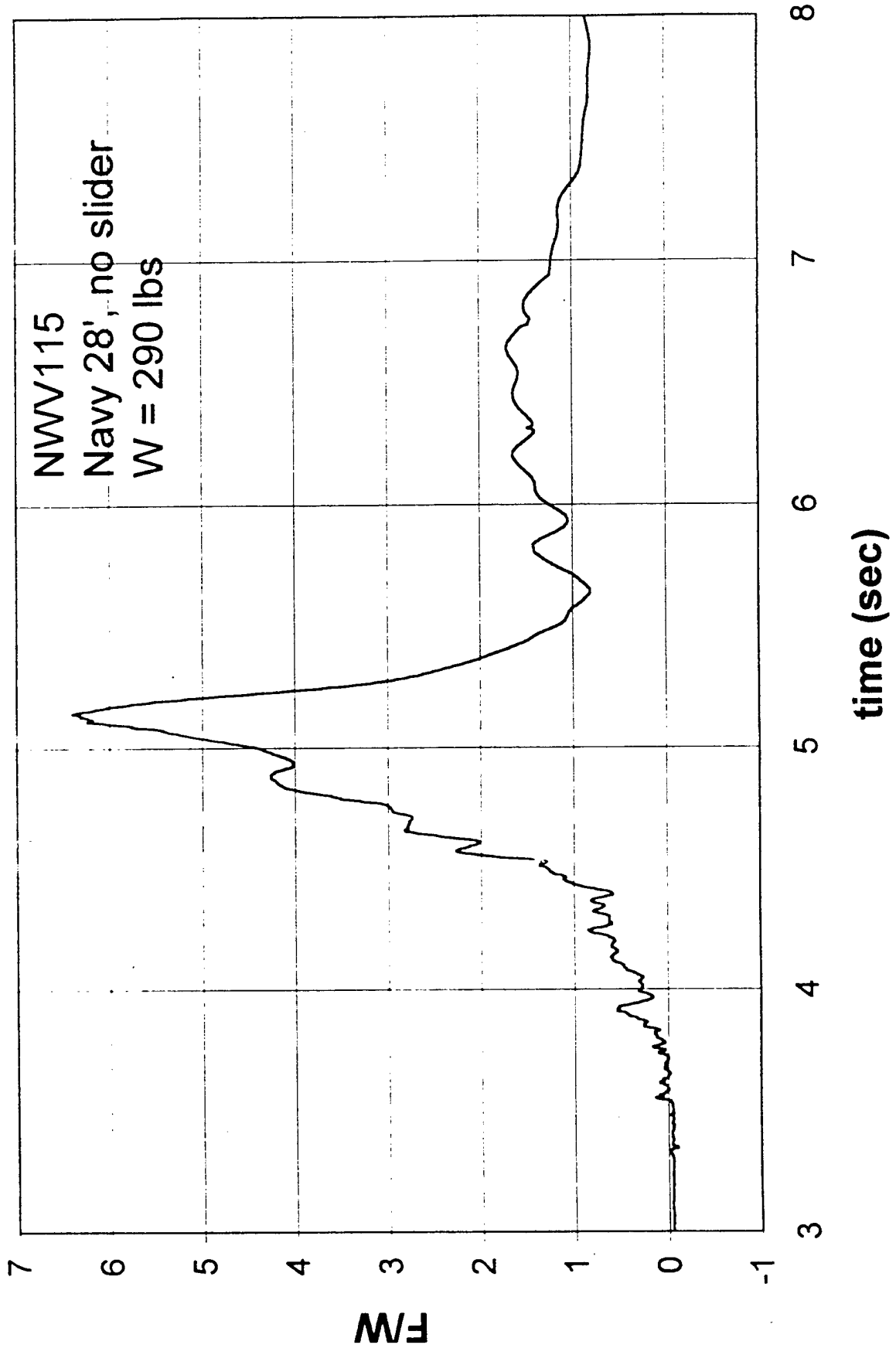


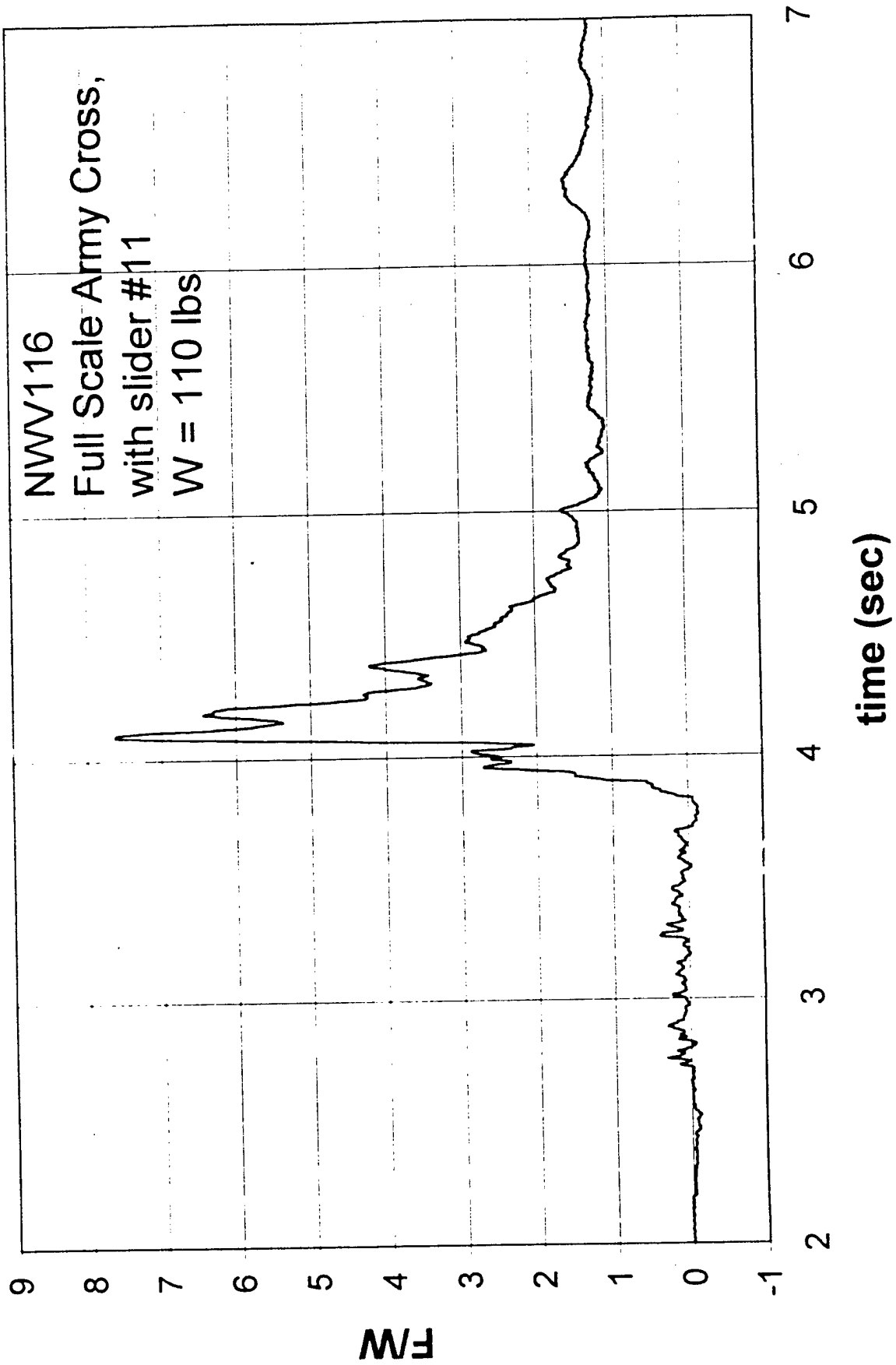


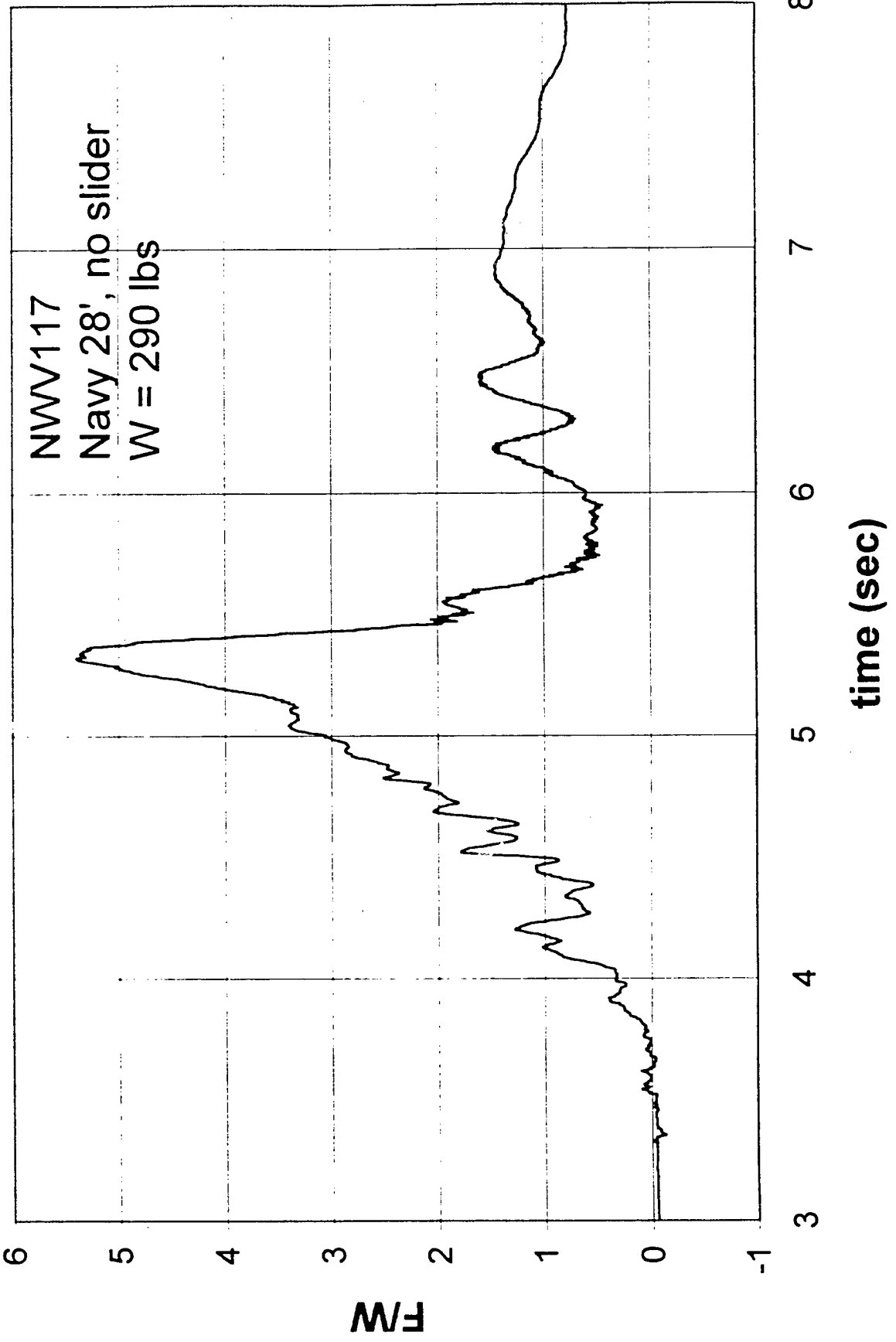


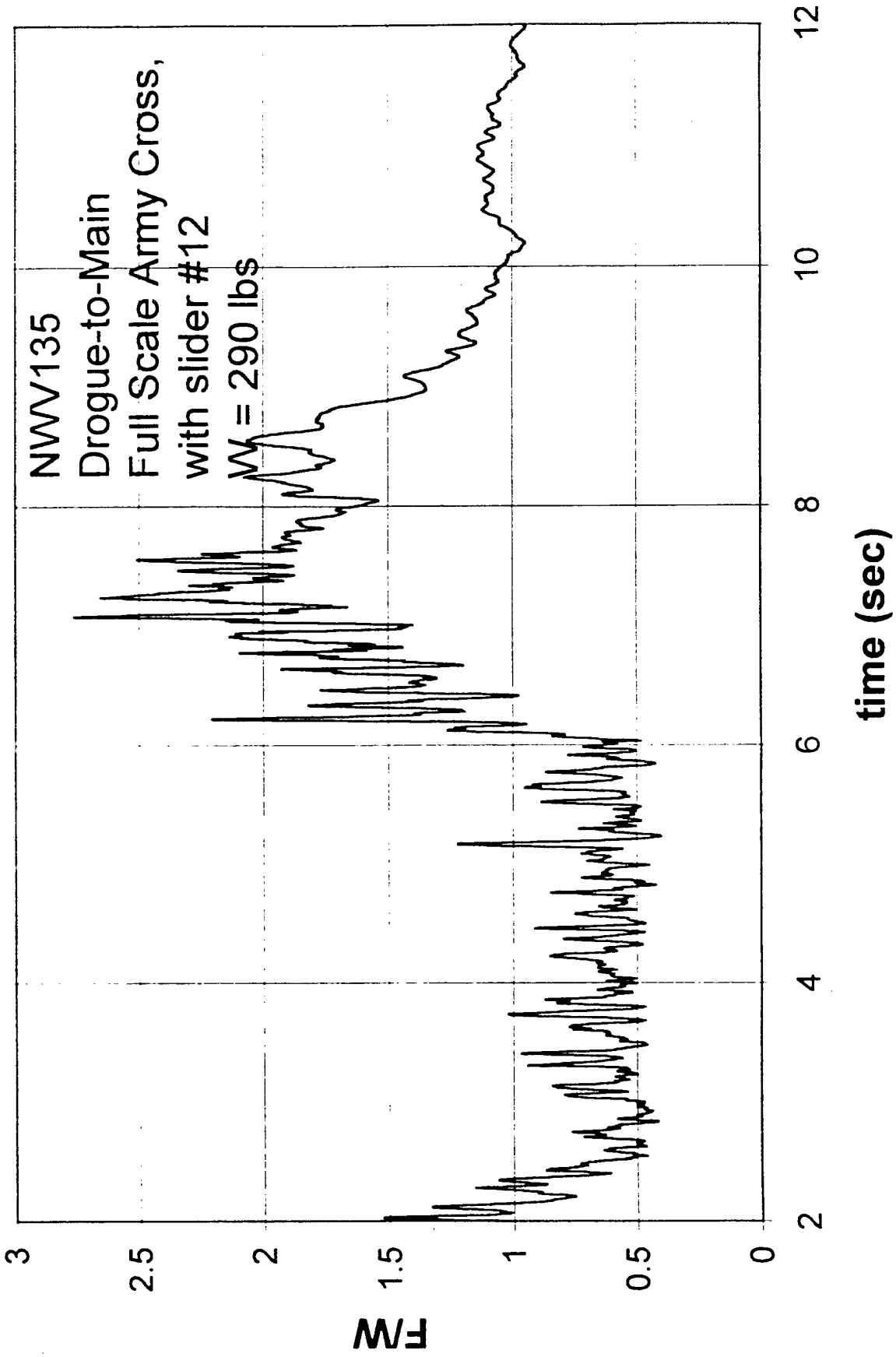












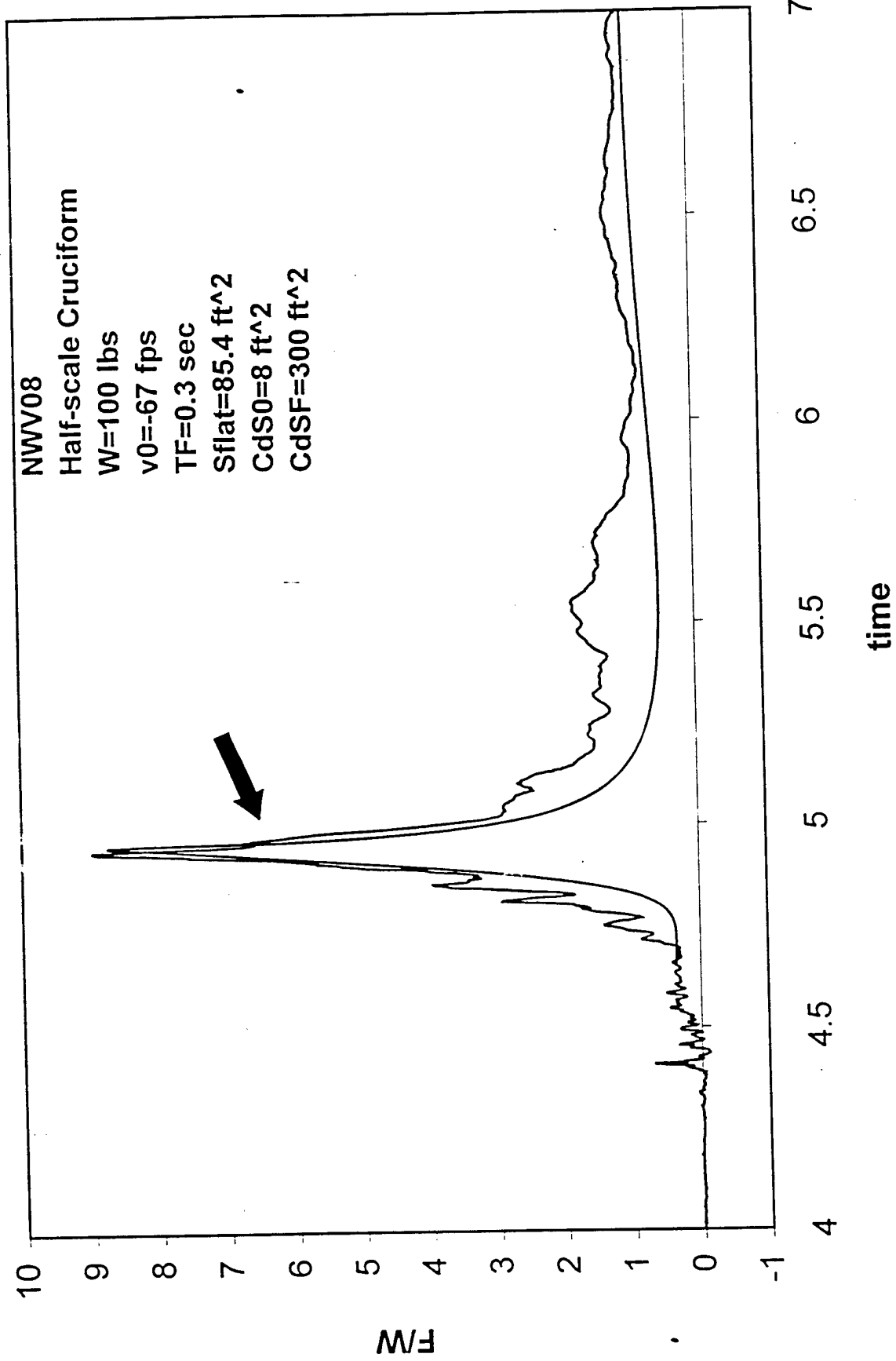


Figure 1. Total parachute riser force, per unit payload weight, versus time (sec). Half-scale U.S. Army cruciform parachute. The smooth, continuous line corresponds to the calculated force using equation (3.5) through (3.10). The arrow marks the end of inflation and the beginning of the post-inflation deceleration phase. Extracted from Appendix 2, figure 4.

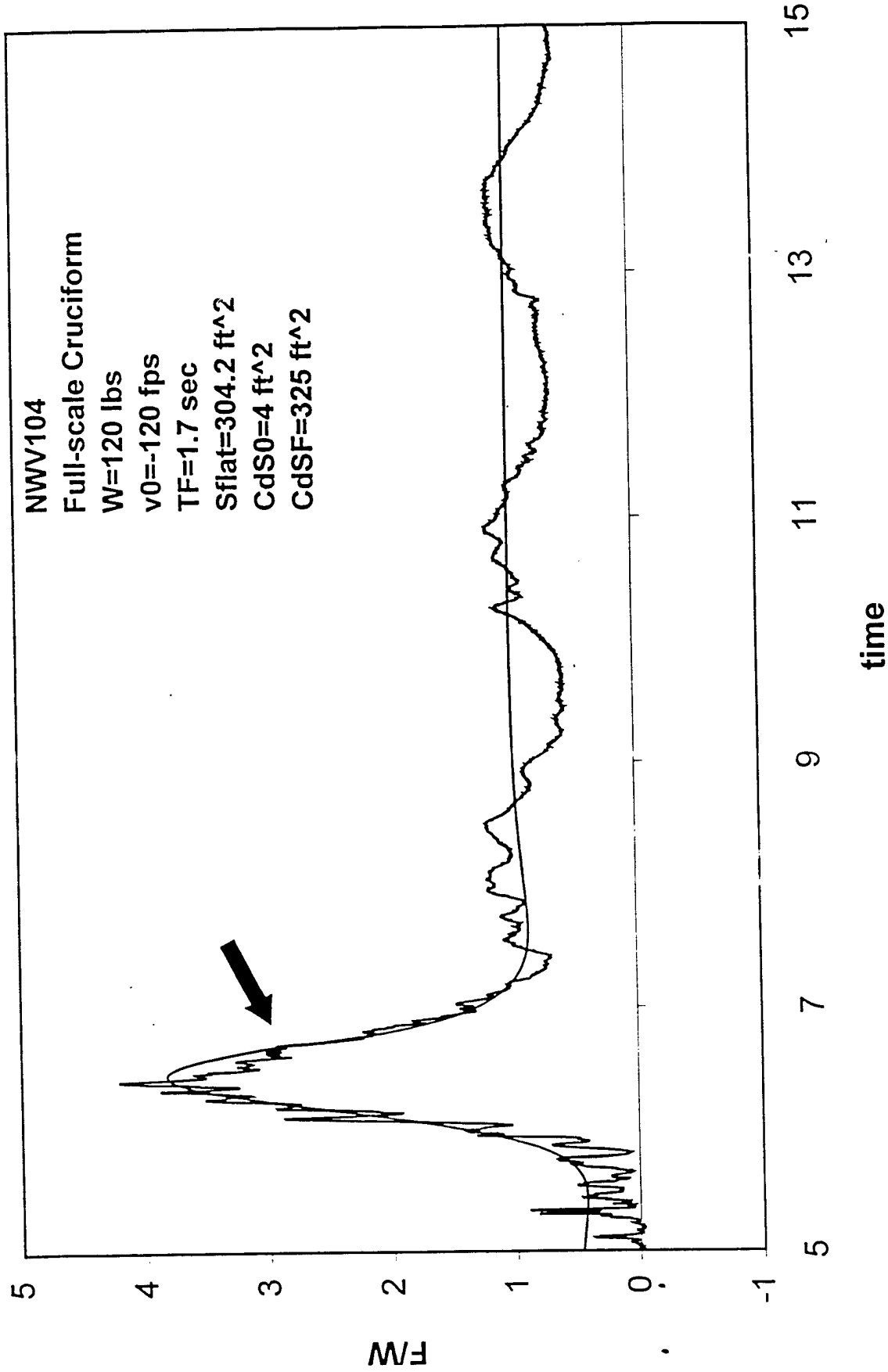


Figure 2. Total parachute riser force, per unit payload weight, versus time (sec). Full-scale U.S. Army cruciform parachute. The smooth, continuous line corresponds to the calculated force using equation (3.5) through (3.10). The arrow marks the end of inflation and the beginning of the post-inflation deceleration phase. Extracted from Appendix 2, figure 7.

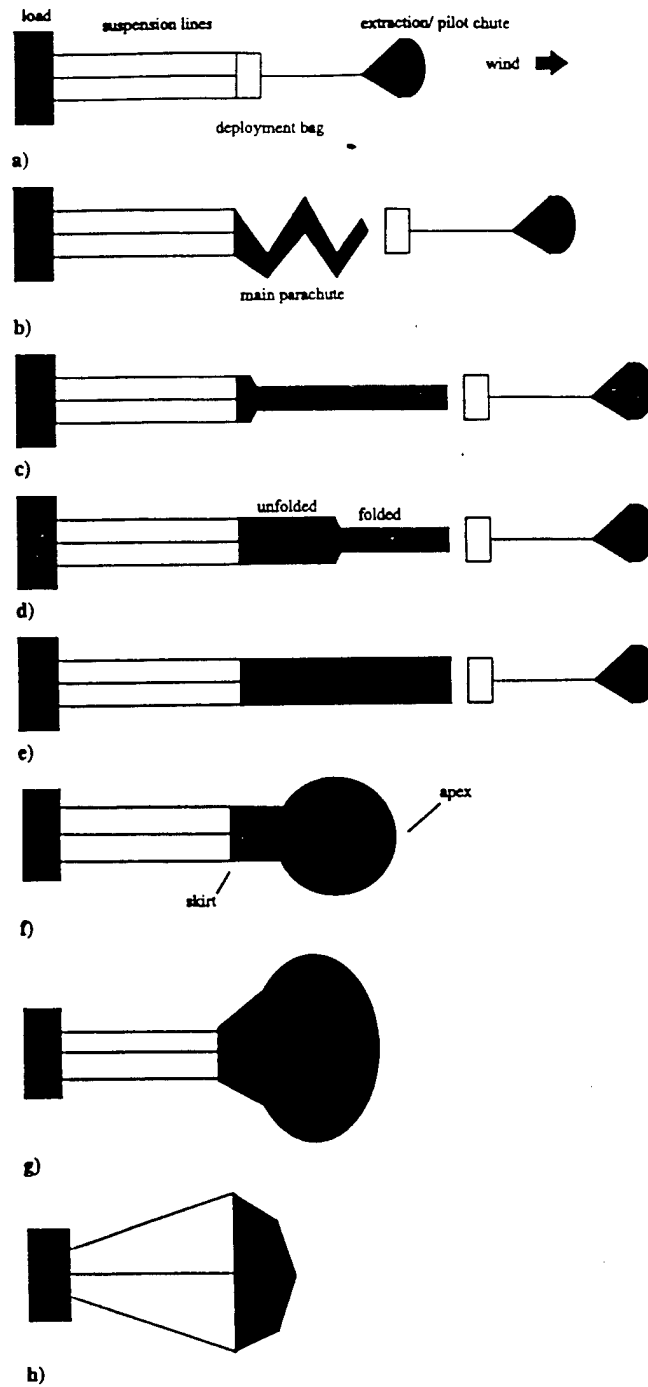


Figure 3. The many stages of parachute deployment and inflation. Steps *a* and *b*: bag and main chute deployment. Steps *c* through *e*: parachute unfolding and early pressurization. Steps *f* through *h*: late inflation and canopy spreading. Figure extracted from reference 10.

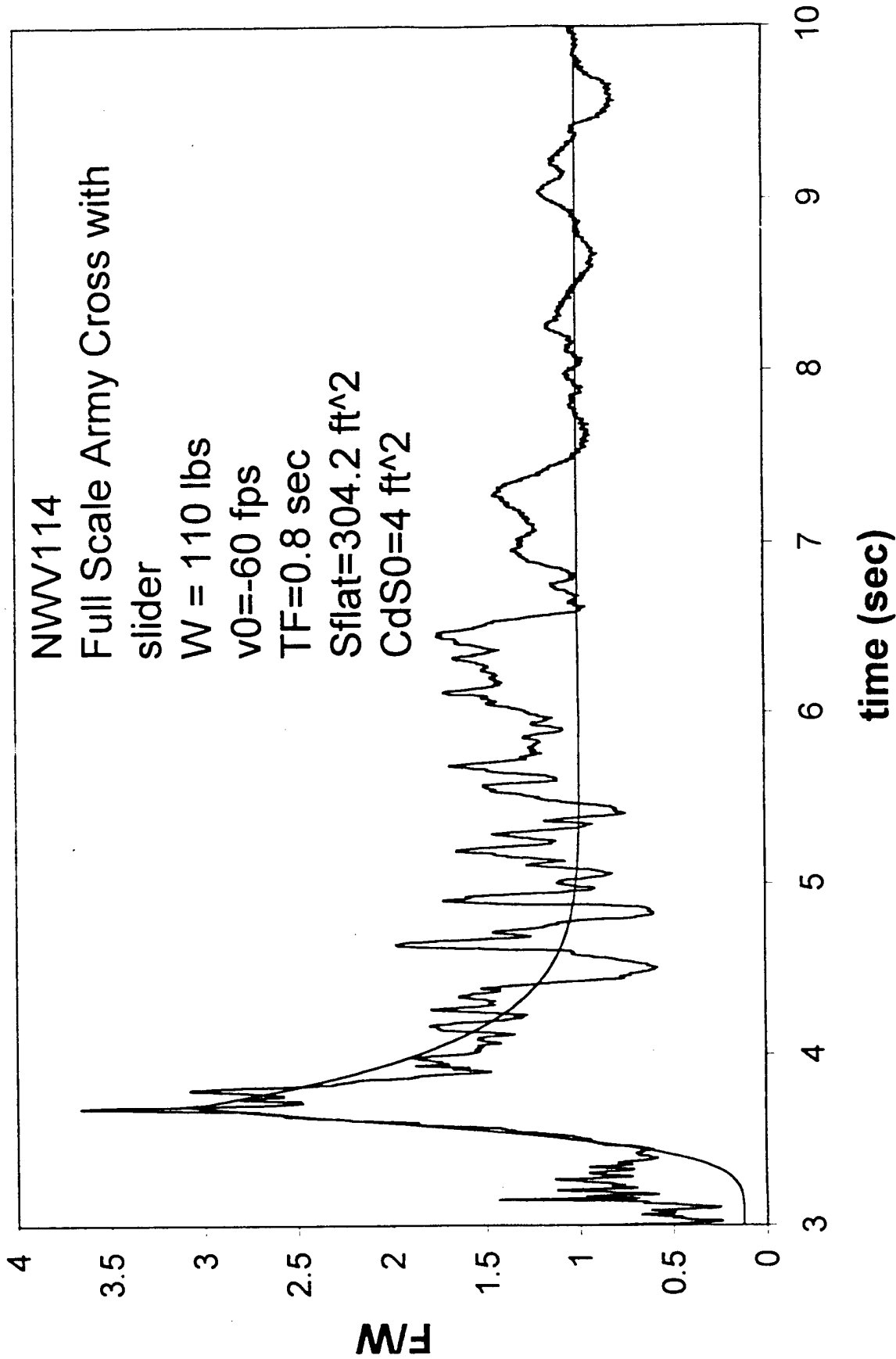


Figure 4. Total parachute riser force, per unit payload weight, versus time (sec). Full-scale U.S. Army cruciform parachute reefed with a large slider. The smooth, continuous line corresponds to the calculated force using equation (3.1), (3.20) and (3.10). The experimental data corresponds to drop NWV114.

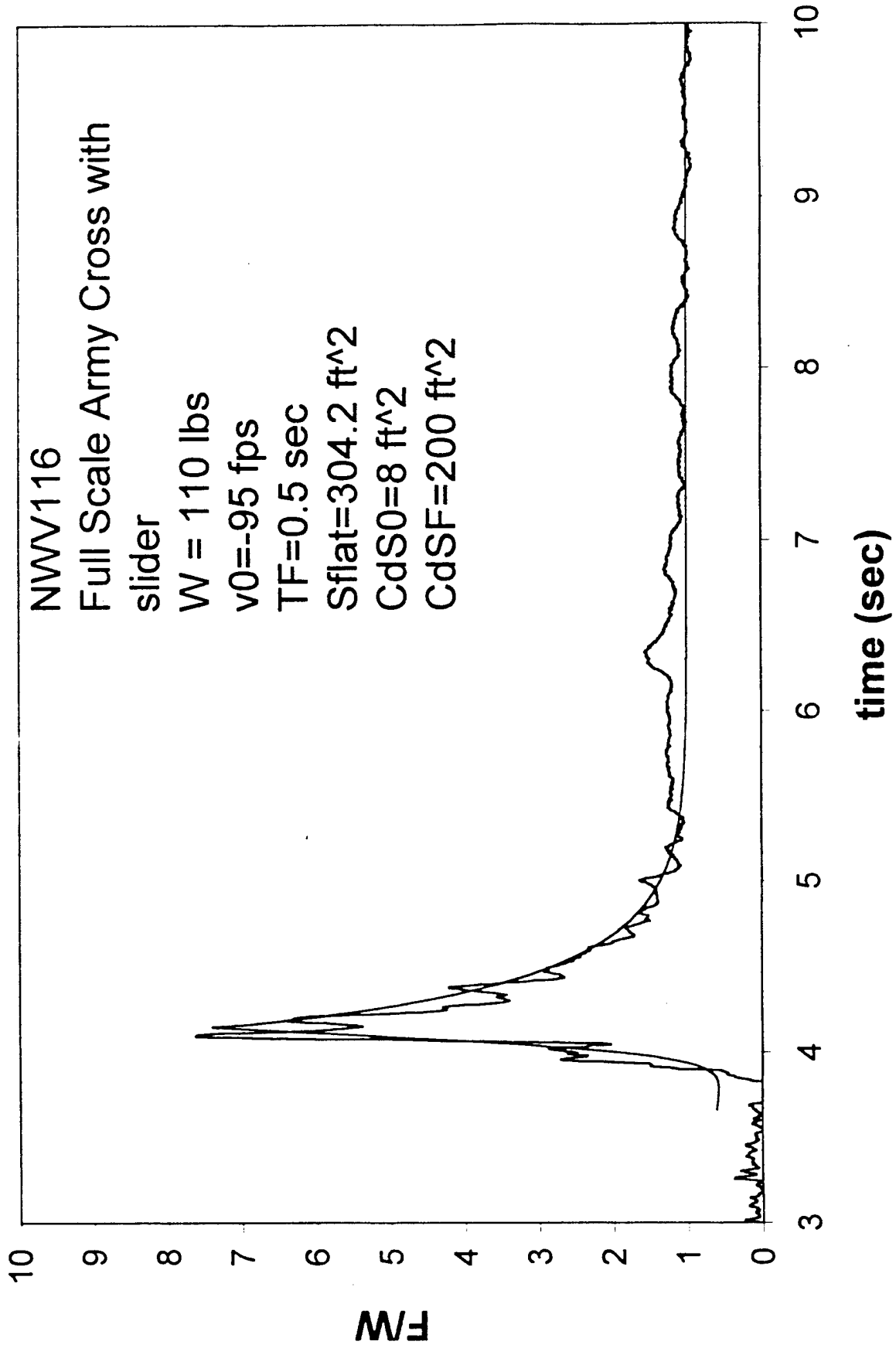


Figure 5. Total parachute riser force, per unit payload weight, versus time (sec). Full-scale U.S. Army cruciform parachute reefed with a large slider. The smooth, continuous line corresponds to the calculated force using equation (3.1), (3.20) and (3.10). The experimental data corresponds to drop NWV116.

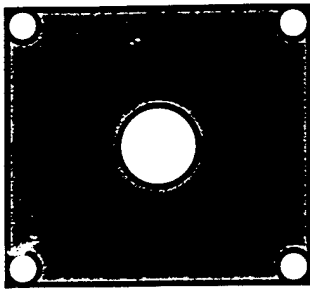


Figure 6. Slider design, which includes four corner grommets and vent hole at center. The fabric filling is shown in red.

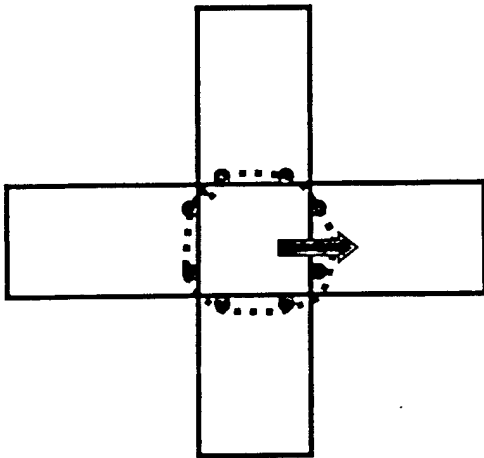


Figure 7. Crown reefing for a cruciform parachute. The design shows eight reefing rings (in red), one reefing line (dotted line) and one cutter (green arrow).

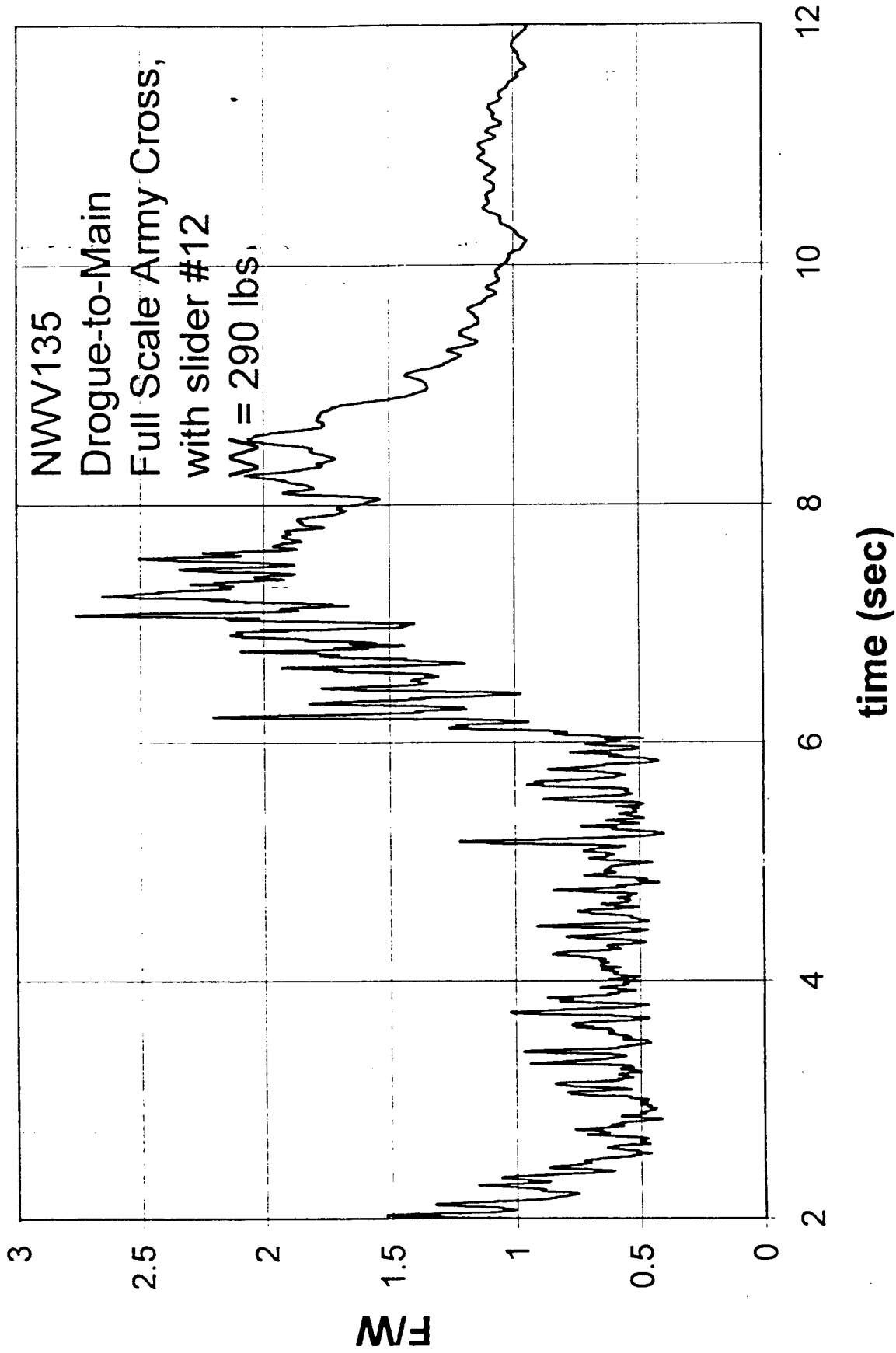


Figure 8. Riser load data during one demonstration drop of the doubly-reefed cruciform parachute system (concept F) – drop NWV135. The data shows the load sustained during the 4-second drogue phase which, is then followed by the very slow and gentle canopy opening slider descent. Unreefed parachutes of the same kind routinely develop up to 6g maximum opening forces when launched at similar aircraft speeds.